Connections between solar flare characteristics and their underlying magnetic drivers

Konstantina Loumou

Astronomy and Astrophysics Group
School of Physics and Astronomy
Kelvin Building
University of Glasgow
Glasgow, G12 8QQ
Scotland, U.K.

Presented for the degree of
Doctor of Philosophy
The University of Glasgow
JANUARY 2020

Abstract

The flare occurrences on the Sun have been a focal point of investigation for many years in the Solar community. Our increasing dependence on satellite technology as well as a way of living requiring frequent airplane trips, leave us susceptible to the interactions of the solar magnetic field with that of Earth's. Being able to identify parameters that could signal the occurrence of solar flares, would be advantageous towards our efforts to enhance our knowledge of flares and the principles of Space Weather. This thesis tackles two aspects of this problem.

In its first half, we investigate a pattern of the solar magnetic field as it expands in the heliosphere, the Hale Sector Boundaries (HSBs). The heliospheric magnetic field typically is organised into two or four different sectors of alternating polarity. The HSB is the segment for which the change in magnetic sector polarity agrees with that of the leading and following sunspots in each hemisphere. Based on heliospheric measurements, we made use of recorded times when the sector boundaries were detected from Earth and mapped it back to the Photosphere assuming ballistic propagation of the solar wind. At these times, the HSB was at the Central Meridian back at the Sun. Using the flare positions as provided by the RHESSI instrument, we found them concentrated in the hemisphere of the Hale boundary. We then further developed a method of detecting HSBs using magnetic field extrapolations, which allows us to detect all HSBs present at all times flares were recorded. It additionally gives the chance to track the HSBs at all solar latitudes. Both approaches confirmed an association, adding to existing literature showing likewise. We find that 41% of RHESSI flares during Cycle 23 and 47% during Cycle 24 had a location within 30^o from their closest HSB. We later show how this pattern has evolved during the declining phase of Cycle 23 and the rising phase of Cycle 24, following the expected change between northern

and southern hemispheres. Our findings show the rising phase of the solar cycle to be connected with a four-sector structure, while after solar maximum the sectors turn to a two-sector structure. That was an observational result that proved to be consistent during the times studied in this thesis. Finally, we contrast their migration paths to those of another feature of the large-scale field, Active Longitudes. Moving into a Carrington system, the HSBs were found to propagate faster than the Carrington rate at the beginning of a Cycle and slower at the declining phase, a property shared with Active Longitudes. Superimposing the paths followed by HSBs at Central Meridian to those of Active Longitudes showed no clear correlation. There were both points of overlap as well as large deviations, leaving space for further investigation.

In the second half of this work, we moved into the smaller scales of the solar magnetic field, looking for potential persistent changes of its properties before microflares. We presented two different methods of fragmenting a line of sight magnetogram as well as an approach for tracking those fragments with time. We then applied our pipeline on data provided by the SDO/HMI instrument on four individual regions; one small flux emergence region used mainly for testing our code and three active regions with long series of microflares. The timelines of their bulk properties did not return any recurring trends in their patterns. We found the fragment area and unsigned flux to both increase and decrease before or after the start of the flare, with the average area and flux per fragment to be mostly unaffected by the emission of flares. We noted more changes in the positive field than the negative and mainly before a flare occurs. However, the results lacked consistency in their pattern to declare that a specific association has been spotted. Similarly, there was no specific direction the fragments were drifting towards, with the fragments of one of the regions consistently moving towards the left, while for the other two spreading apart. The Python pipeline we developed for time tracking the line of sight magnetic field did determine a number of additional properties about the fragments, which could be further studied and applied to new regions in future work.

Our work shows that indeed there seems to be a stronger correlation of the HSBs with flaring activity and that there would be merit to explore further how the magnetic field is organised and results to this association. It also showed that

the correlation is not as strong as to suggest that the HSBs can be used as a forecasting property by itself. The second project sets the ground for understanding the processes leading to microflares, a thoroughly unexplored field to-date. The pipeline has been created and tested, with the initial results not revealing a magnetic signature of microflares. However, the pipeline with a refinement can be used for a statistical study similar to those already existing for flares of large energetic output.

This thesis is my own composition except where indicated in the text. No part of this thesis has been submitted elsewhere for any other degree or qualification.

JANUARY 2020

Acknowledgements

This research has made use of SunPy v1.0.6 an open-source and free community-developed solar data analysis Python package (Community et al. 2015).

Contents

List of figures

List of tables

Chapter 1

Introduction

Part of the contents of this Chapter has been published in Loumou, K. et al. (2018)

1.1 Solar Flares

Solar flares are sudden releases of magnetic energy followed by a burst of electromagnetic radiation. They take place in active regions, locations on the Sun's atmosphere where the rate of change of the direction and value of the magnetic field is high. Falconer et al. (2012) defined a proxy in order to measure the likelihood of a region to flare, $\int |\nabla B_{LOS}| dl$. They found that when the proxy exceeds 10^4 Gauss, the region is likely to produce a flare.

The process leading to a flare is illustrated in Figure 1.1, portraying what is called the "CSHKP Model" (Carmichael 1964; Sturrock 1966; Hirayama 1974; Kopp & Pneuman 1976) . The solar magnetic field originates from the solar interior, being pushed outwards by buoyancy, showing up as a prominence. As it extends into the outer solar atmosphere and new flux emerges, the rotation of the star causes the footpoints of that prominence to move, leading to magnetic concentrations with opposite polarities coming in proximity. Plasma inflow then

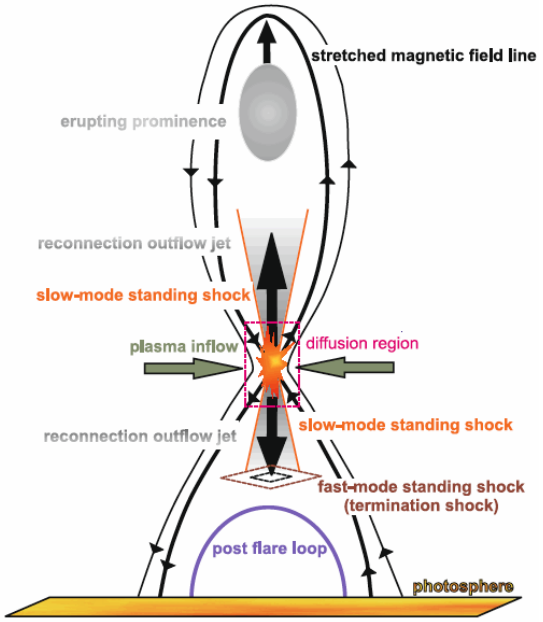

Figure 1.1: The CSHKP model. As the magnetic field arises from the interior, an instability, here a flow of plasma, can get the field lines to move closer, causing it to reconnect. In this way, magnetic energy is being released and what is called a solar flare takes place. Cartoon from (Mann et al. 2009).

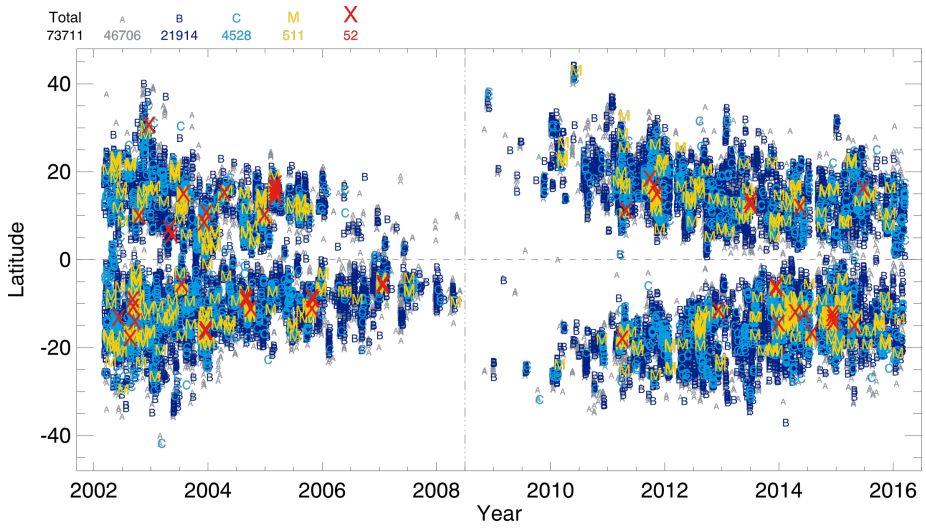

Figure 1.2: "Butterfly diagram" from the latitudes for the RHESSI flarelist used in this work. Figure from Loumou, K. et al. (2018).

has the potential to push the magnetic lines closer, allowing Lorentz forces to act. Reconnection takes place at that point and energy of the order of up to 10^{32}ergs is released (Shibata & Magara 2011), an event termed as a solar flare. At the initial stage of the flare, energy is mainly emitted in hard X-rays. Particles trapped in the top part of the loop of Figure 1.1 absorb part of the released energy, which is transformed to kinetic and the particles move to the Heliosphere, subject to the magnetic field configuration and emitting mainly in microwave and radio wavelengths. Additionally, electrons become trapped into post-flare loops and return to the Photosphere, emitting energy mainly at soft x-rays. Finally, the system is reconfigured into a lower energy state.

1.2 Active regions

Flares have a strong correlation with the solar cycle, an eleven year periodic change of solar activity, and the magnetic field. Starting from a period of minimum number of events, the solar cycle reaches its peak roughly 5.5 years later, to end at a minimum again. With each new Cycle sunspots, regions of strong magnetic field, appear within $\pm 40^o$ latitude, reaching their peak number at the solar maximum.

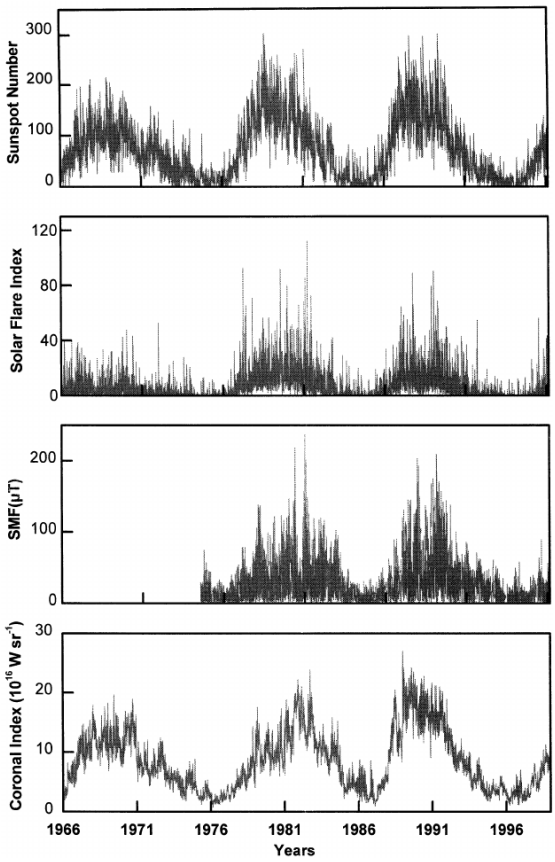

Figure 1.3: Number of sunspots, flare index, solar magnetic field and coronal index per day. Figure from Mavromichalaki et al. (2003).

As the cycle progresses the sunspots are concentrated at lower latitudes. This can be seen in Figure 1.2 where RHESSI flare positions we later use in Chapter 3 map out active regions.

Active regions appear as concentrations of magnetic field of opposite polarities. There is a configuration of "leading-following" sunspots in an active region where the leading and following sunspots have opposite polarities. During the same cycle, the polarities of leading-following regions will be opposite between the two solar hemispheres as well (eg. in an odd cycle, the positive sunspots are leading in the northern hemisphere while the negative are leading in the southern hemisphere). When a new cycle begins, the new sunspots of a hemisphere will have a reverse "leading-following" polarity (Carroll & Ostlie (2006), page 381). Figure 1.3 illustrates that as the cycle progresses from minimum to maximum, the sunspot number, number of flares and value of the magnetic field increase in phase, proving their close connection. The total cycle cycle length is of 22 years, where the sunspots will re-appear in the same region with the same polarity as the Hale's Polarity Law (Hale et al. 1919).

1.3 Hale Sector Boundary

As the magnetic field propagates from the surface of the Sun to the Heliosphere, the solar rotation shapes that radial field into the form of the Parker's spiral (Parker 1958). At the same time, the field emanating from the solar interior is subject to Hale's law. This means that as the solar cycle evolves and the sunspots are being dragged from the differential rotation to lower latitudes, the global magnetic field is being led to a change of its polarity. Mapping the solar magnetic field from a distance during the 11 years of a cycle, the polarity of the heliospheric field will be separated in two halves or four quarters, named a "sectors". At solar minimum, the Sun is a bipolar star and that is reflected in a two-sector structure of the polarity of the heliospheric magnetic field. During solar maximum, the sun is a quadrupolar, which results in the polarity of the heliospheric field to be configured in four sectors.

The first report of this phenomenon came with the advent of the satellite era with the first observation of the Interplanetary Magnetic field (IMF) through the

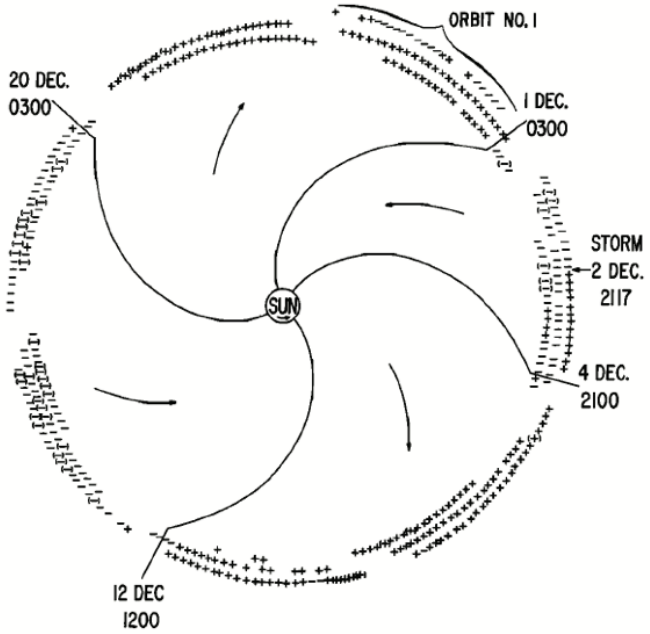

Figure 1.4: The Interplanetary Magnetic Field as it is separated in four different parts with alternating polarities. The positive sign indicates field pointing outwards and the negative inwards from the Sun. Cartoon from Wilcox & Ness (1965).

satellite IMP1 of the Explorer series. It was shown that the IMF is separated in four sectors with opposite polarities, Figure 1.4 (Ness et al. 1964). The positive polarity indicates field with direction towards the observer while the negative indicates the opposite. Wilcox & Ness (1965) found that the sectors in the time period they studied them covered an area of $\pm 35^o$ either side of the equator and $\pm 90^o$ either side of their boundary while Svalgaard et al. (1975) reported that there is a North-South asymmetry in the surface of the sectors; as the Earth-Sun distance changes, so does the inclination of the boundary to the solar equator, subject to the Rosenberg and Coleman effect (Rosenberg & Coleman 1969). During the course of a year, the position of the Earth will be either above or below the ecliptic. Therefore, half of a year the polarity at the Earth is dominated by the Sun's southern hemisphere, while the other half by the Northern. As stated before, the sectors will alternate from a two-sector stucture during the declining and minimum phases of the Solar Cycle to a four-sector structure close to solar maximum (see also Getachew et al. 2017). In modern literature the boundary is termed as the "Neutral Line of the IMF". However, since this work is a direct

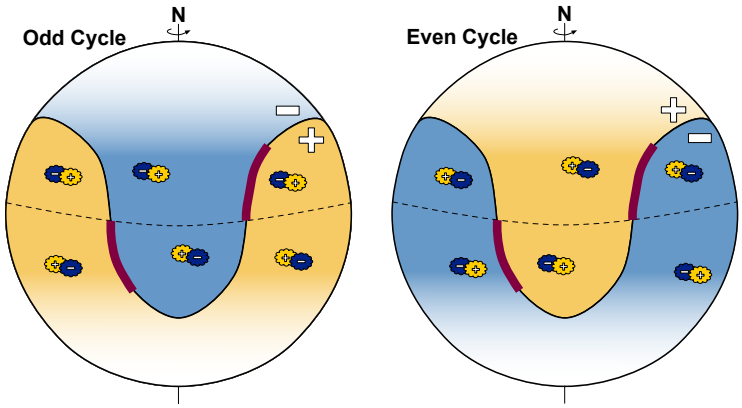

Figure 1.5: Example cartoon of the Sun, with the Hale Sector Boundary (thick purple lines) for odd (left) and even (right) Cycles. Yellow for positive IMF Polarity while blue for negative.This example is during a period of four-sector crossings. Cartoon from Loumou, K. et al. (2018).

continuation of the studies started in the 1970's, we keep the old term throughout.

Svalgaard (1968) and Mansurov (1969) independently developed a method - later further tested by Svalgaard (1972) - of detecting the crossing of the sector boundary from Earth. They realised that at the polar latitudes, the solar wind causes enough disturbance on the geomagnetic field to be detectable. More specifically, when the boundary is crossing the Earth, measurements of the geomagnetic field taken at stations in the polar regions (Vostok at latitude -84.9° and Thule at latitude 86.8°) show a perturbation to the Z component of the geomagnetic field seen as a flip in polarity. In fact, this is the flip in polarity of the Interplanetary Magnetic Field. When the two stations measure the polarity change, the boundary was at Central Meridian on the Sun about 5.5 days before, the average time the solar wind needs to propagate towards Earth. There are enough historical data for this method to be applied even back to the beginning of the 20^{th} century. Therefore, we have a long account of sector boundary crossings from Earth, which can be found in a list maintained at `http://www.leif.org/research/sblist.txt`, the origin of the HSB data for Chapter 3. If we adopt a ballistic approximation as the solar wind propagation, this implies that the time a change in polarity is detected at Earth, is the time the sector boundary was a Central Meridian back at the Sun plus the travel time of the solar wind from Sun to Earth: $t_{Earth} = t_{Sun} + t_{travel}$.

The section of the boundary that indicates the polarity change of the IMF in the same orientation as the sunspots for that hemisphere, is called a Hale Sector Boundary (hereafter HSB). Since the sunspots are subject to the Hale cycle, a cyclic 22 year polarity reversal of the global magnetic field (Hale et al. 1919), the location of the HSB indicating a particular polarity change per solar hemisphere will also change between odd and even Cycles. Figure 1.5 shows an example of how the boundaries would look like during a time of four-sector boundary crossings and highlights with a thick brown line which part of the boundary is the HSB. The yellow surface indicates the positive polarity of the IMF and the blue the negative. The black curve indicates the boundary between the yellow and blue sectors. For an observer at Earth, they would register the IMF's field in this cartoon from right to left. Therefore, moving towards the left side of Figure 1.5:

- Left panel: During an odd cycle, in the northern hemisphere the positive sunspots lead and the negative follow. Therefore the HSB is the boundary showing the IMF change $(+, -)$. In the southern hemisphere the negative sunspots lead and the positive follow. Therefore the HSB is the boundary showing the IMF change $(-, +)$.

- Right panel: During an even cycle, in the northern hemisphere, the negative sunspots lead and the positive follow. Therefore the HSB is the boundary showing the IMF change $(-, +)$. In the southern hemisphere the positive sunspots lead and the negative follow. Therefore the HSB is the boundary showing the IMF change $(+, -)$.

The HSBs significance was first indicated by Bumba & Obridko (1969) who found flares to be occurring around sector boundaries. Dittmer (1975) proved the distinction that it is the HSBs that exhibit flares, and in fact, the non-Hale part of the boundary have much fewer flares in comparison. They used the times of the Hale Sector Boundary at Central Meridian for times ranging from 1964 to 1970 (Cycle 20) and flare locations as reported in Solar-Geophysical Data. They identified a much higher flare occurrence at the HSB crossing. This preference was more noticeable for northern hemisphere flares, where the magnetic polarity matched Hale's law. At the same time, Svalgaard & Wilcox (1976) showed that the Fe XIV line, a line emitted when a flare takes place - with material heated to

10-20 MK (Fletcher et al. 2011) - reaches its maximum when above the HSB and its minimum when above the non-Hale part. However, due to the absence of an extensive and reliable database of flares, and crucially their location, no further tests could be made. The launch of the RHESSI instrument (see section 2.1) was an important factor with overcoming that problem. With sensitivity to flares of GOES flux from 10^{-8} to 10^{-3} Wm^{-2}, complete with their location, Svalgaard et al. (2011) re-produced the work of Dittmer (1975) for the last half of Cycle 23 (2002-2009) and confirmed the findings. They also used the NOAA flarelist as an alternative dataset, which gave similar results. The study of Svalgaard et al. (2011) was limited to only RHESSI flares that occurred about the time of HSB at central meridian.

In Chapter 3, we reproduce the process of Svalgaard et al. (2011) for Cycle 23, extend it to Cycle 24 and create a more enhanced method of detecting Hale Sector Boundaries, allowing the HSB-flare distance for all RHESSI flares to be determined. This work was also published in Loumou, K. et al. (2018).

A complete review on Hale Sector Boundaries can be found in the review article Hudson et al. (2014).

1.4 Active Longitudes

The concentration of magnetic activity in terms of longitude has been suggested since the time of Carrington (1863). Initial studies of "Active Longitudes" (e.g. Losh 1939) found substantial ambiguities in their existence and precise location. A copious literature has developed to characterise these regions, testing their usefulness for solar activity prediction and probe their source and implications for dynamo theory (e.g. Usoskin et al. 2007). Several terms have been used for these regions, including "nests of activity" (Gaizauskas et al. 1983; Zwaan 1987), but all these describe locations where there is a strong tendency for flux emergence to persist over long timescales.

The general approach for finding Active Longitudes is to filter the activity tracer, i.e. sunspots or flares, so that only the most dominant regions per time remain, often requiring a correction for rotation at rates differing from those of the Carrington synodic period (e.g. Usoskin et al. 2007). A variety of techniques have

been applied to active longitude studies but these can sometimes produce artefacts (e.g. Pelt et al. 2010) that can lead to ambiguities in the quantitative properties of Active Longitudes. The work of Berdyugina & Usoskin (2003) and Usoskin et al. (2005) used the Greenwich sunspot data, finding two Active Longitudes in each hemisphere about 180° apart. This pattern lasted for several Solar Cycles. At any given time one of the Active Longitudes was more dominant than the other, with the activity switching from one Active Longitude to the other ("flip-flopping"). These Active Longitudes were affected by differential rotation, but at a different rate to the sunspots and were asynchronous between hemispheres. Berdyugina et al. (2006) provided a qualitative explanation for their results in terms of the internal solar dynamo, with it either being a differentially rotating magnetic structure or a solid rotator with a stroboscopic effect producing the observed behaviour. Similarly behaving Active Longitudes have been identified via EUV observations of coronal streamers (Li 2011), as well as flare locations during Solar Cycles 19-23 (Bai 2003) and Cycles 21-23 (Zhang et al. 2011).

The Debrecen photoheliographic sunspot data have contributed to active longitude studies (Gyenge et al. 2012, 2014, 2016), leading to the conclusion that about 60% of X-ray flares occurred with ±36° of an active longitude. This work again shows two bands of activity, with one being more productive than the other and this varying over time (the "flip-flop" behaviour). These regions were narrow during the starting and decay phases of each Cycle (about $20° - 30°$) but wider (60°) during maximum. They also showed how the Active Longitudes' rotation rates vary over each Cycle. Initially they are faster than the Carrington rate but near solar maximum start to slow down, resulting in a "parabolic migration path" relative to the Carrington rate (Gyenge et al. 2016). This time evolution of their location was previously noted by Usoskin et al. (2005). The properties of the sunspot groups near Active Longitudes, such as complexity and helicity, were also found to be more preferential for CMEs to occur (Gyenge et al. 2017).

Studies up to-date have tried to compare the Active Longitudes with flaring activity Gyenge et al. (eg. 2016, 2017) or modelling of the open structures of the IMF connecting Active Longitudes with flux concentrations (Ivanov & Kharshiladze 2013; Ivanov 2010). In Chapter 4, we use our observations to test the temporal evolution of Hale Sector Boundaries and contrast it with that of Active

Longitudes.

In the first half of this thesis, we will show how the Hale Sector Boundary is associated with flares. We will delve even further on its pattern with time and we will show that its path bares both similarities and differences with the migration path of Active Longitudes.

1.5 Magnetic field changes during flares

Observed changes in the solar magnetic field before and after flares have long been the subject of numerous studies. Identifying whether or not there is a particular signature of the magnetic field in the signal, or if it is a consequence of them is the focal point of many of these studies. A landmark breakthrough was the association of the value of the unsigned flux around the Polarity Inversion Line (PIL) with large (M and X-class) flares in Schrijver (2007). However, the exact reason these two events are connected or the exact change that happens before flares is still not understood. A detailed analysis on the topic has been presented in the review papers of Wang & Liu (2015) and Toriumi & Wang (2019).

Leka & Barnes (2007), in the end of a 4-paper series devoted to the subject, conclude a statistical study finding that the state of the photospheric magnetic field in vector magnetograms at any given time has limited bearing on whether a region will be productive. In their research, they also used Line of Sight (LoS) magnetograms and did not see any changes in the field. Welsch et al. (2011) confirms their findings, adding that the evolution of the LoS does not seem to show any indication of flaring.

Petrie & Sudol (2010), in a study searching stepwise changes for M and X-class flares, identified permanent stepwise changes in the backgound of the magnetic flux before the flares occurred. Burtseva & Petrie (2013) followed up by making use of the Yet Another Feature Tracking Algorithm (YAFTA) to identify the exact location of those changes, finding large flux changes mainly associated with X-class flares, as well as close to the limb. They report that the changes of the horizontal component of the line-of-sight magnetic field close to disk centre are about half in number compared to the ones closer to the limb.

Burtseva et al. (2015) further compared the field changes with quicklook images provided by the RHESSI instrument. A superposition of the RHESSI data onto the feature with stepwise changes showed a good correlation to features where there was a strong change in the field. In most cases, this is the region close to the PIL. Moving further away from the PIL, that correlation dropped, meaning that later emission from RHESSI is not well associated with stepwise field changes. They also find those changes to take place either before or at the start time of flares and are completed by the time RHESSI completes recording of the hard X-ray output. Tracking the changes with time, they find that they follow the same migration path that the loop footpoints follow. They conclude that flares and field changes are correlated both in time and space, but do not share the same time nor do they happen at the precise same location.

Wang (1992) and Wang et al. (1994) showed that field changes are much more prominent in the horizontal than in the LoS component of the field. Therefore, Sun et al. (2017) go one step further by using the Stokes Parameters of the SDO/HMI instrument to construct vector magnetograms with a 135 seconds cadence. This gives them the ability to test and confirm the findings of Petrie & Sudol (2010), without losing the information usually non-present in a 720 second HMI dataset. They find a sharp increase of the transverse component of the field during the start time of the flare, in agreement with Burtseva et al. (2015) as well. They also confirm Sudol & Harvey (2005) who showed that the field change lasts about 10 minutes, but flag that even with their refined approach there is still a percentage of the field that is still unresolved with current instrumentation.

As similar studies for small flares are not in existence, with the largest statistical sample to-date being that of 75 flares from Castellanos Durán et al. (2018), with the flare of smallest X-ray output being one B-class flare. They note that from their sample, the smallest flare exhibiting a change that is a C3.0 flare, the smallest flare in literature associated with a stepwise change of the field.

In the second half of this thesis we will make a first attempt to fill in this gap. We will present two methods of fragmenting magnetograms as well as tracking them with time. In the final part of this work, we will explore the changes that the LoS magnetic field of microflaring active regions exhibited before and after microflares.

Chapter 2

Instrumentation

The data sources of this PhD thesis are the flare catalogue provided by the Reuven Ramaty High Energy Solar Spectroscopic Imager (RHESSI) and the magnetograms given from the Heliospheric Magnetic Imager (HMI) on board the Solar Dynamics Observatory. The flare lightcurves and the backtracked flare images from RHESSI were also used in order to verify individual events from the flarelist as indeed solar and at the positions reported in the RHESSI catalogue. However, the flare information that form part of the final analysis are mainly the location of the flare, start peak and end time as well as the GOES background flux. In Chapter 6 we also make use of some RHESSI images.

2.1 The RHESSI instrument

The Reuven Ramaty High Energy Solar Spectroscopic Imager (RHESSI) (Lin et al. 2002) was an imaging and spectrometric instrument designed and operated by NASA for a period of 16 years. Launched on 5th of February 2002 it created a vast catalogue of flares with X-ray flux abundance ranging from 10^{-8}-10^{-3} Wm^{-2}. It became unresponsive on 11th of April 2018 at 01:50 UTC and was finally shut down on 16th of August 2018. The official RHESSI catalogue terminates on 3^{rd} of March 2018 with a B5 GOES class flare.The scientific objective of the mission was to investigate how energy is being released during solar flares and how particles get accelerated.

The imager consists of nine bi-grid rotating modulation collimators (RMCs)

that are situated in front of the spectrometer with nine cryogenically-cooled germanium detectors (GeDs), one behind each RMC.

This is to allow imaging of emission from 3keV to several MeV as the RMCs time-encode the spatial information (Hurford 2010).

Flares are light on X-rays over many orders of magnitude and so to maintain sensitivity to smaller and larger events RHESSI uses shutters/attenuators. According to the energy level of the flare, either the thick or the thin shutter will be used to maintain spectral dynamic range.

RHESSI imaging allows the flare position to be accurately obtained to $< 1''$ arcways. Several different algorithms are used to cover the time encoded spatial information. One is the back projection method (Hurford et al. 2002) which is a 2D inverse Fourier transform where the time difference from the counts is translated to distance. Due to the indirect imaging technique some artefacts arise of particular issue. One is that the position of flares near the imaging/rotation axis cannot be determined, as there is no time modulation detected from them. This small region is indicated in my figures later.

RHESSI's pointing and spin rate have to be known very accurately to recover a flare position (and image). There are onboard systems to do this, but one, the Roll Aspect System (RAS), occasionally has data gaps resulting in flare positions at the correct distance from the imaging axis but at the wrong angle. These flares are usually easy to identify as their position is erroneously away from the active regions. It is imperative that the user checks for misaligned flares when handling RHESSI data and run existing routines in order to correct it. This was performed during my research and a detailed explanation is given in the next Chapter.

What makes RHESSI an innovative instrument is its unique competence of studying Hard X-Rays (HXR). This is the part of the radiation that is emitted at the very beginning of a flare, the so called "impulsive phase". It is a product of the well understood Bremsstrahlung radiation and originates from optically thin regions. On the other hand, other instruments, such as GOES, can observe the Soft X-Rays (SXR), the radiation emitted after the onset of the energy release that comes from heated material. For this reason, RHESSI excels in documenting even flares of small intensity. An important issue that arises from that is that at solar maximum the A and B class flares are being obscured by stronger ones (M

and X class). For GOES the same applies for the C class flares. Therefore, when using data from the two instruments one has to keep in mind that the population of event available during that period differs.

Finally, two more issues need to be mentioned. First is the South Atlantic Anomaly (SAA), a region in the Earth's atmosphere with a large amount of energetic particles. In order to protect the instrument RHESSI needs to shut down when crossing it. Second is the annealing, a necessary period of self-remedy that RHESSI needs to undertake every few years. The bombardment of highly energetic particles leads to a degrading of its detectors. In order to minimise this problem they need to be heated to about 100^oC in order to remove damage to the crystal structure of the germanium. In both cases, RHESSI needs to switch off in order to protect any sensitive electronic equipment. When switching back on after those two events, or after night time, RHESSI can confuse the sudden increase of counts as a flare. Although the RHESSI team has put some safety checks to prevent this, errors appear and the observer needs to be careful.

2.2 Helioseismic and Magnetic Imager

The Helioseismic and Magnetic Imager (HMI) onboard the Solar Dynamics Observatory (SDO) is situated at the L1 Lagrangian point, providing full-disk solar data uninterruptedly. HMI returns maps of intensity, velocity and maps of the magnetic field. Its four CCD cameras have a resolution of 4096×4096 pixels with a pixel size of 0.5 arcsec×0.5 arcsecs and have a time cadence of 45 seconds with a background noise level of 5-10 Gauss. Table 2.1 gives an overview of its properties, taken from the official website[1].

[1] http://hmi.stanford.edu/Description/HMI_Overview.pdf

Table 2.1: Characteristics of the HMI instrument

Sensitivity	10 G
Aperture	14 cm
CCD pix size	0.5 arcsec×0.5 arcsec
CCD	4096 pixels×4096 pixels
Resolution	0.5 arcsec/pixel
Lines	FeI 6173 Å

The core objective of the mission was to investigate the convection zone of the Sun and the processes taking place there and ultimately have a greater understanding of the ways flaring phenomena are connected with the solar dynamo.

The magnetograms in the HMI data center are offered as Line of Sight and vector magnetograms. The observables on the Level-1 (ready to be used for scientific purposes) data are given in two cadences. The 45 seconds cadence datasets are the output of subtracting the left and right circularly polarised Dopplergrams created from filtergrams captured from CAMERA 1 (HMI Doppler camera). The 720 seconds LoS magnetograms are the combination of ten 135 seconds filtergrams calculated from the I+V and I-V Stokes parameters as captured from Camera 2 (Vector Field camera) (Couvidat et al. 2016).

In this work we make use of the 45 and 720 seconds HMI magnetograms in Chapters 5 and 6. HMI magnetograms were imported in the pipeline described in Chapter 5, fragmented in smaller segments according to pixel intensity and twelve properties of the magnetic field were calculated and saved out.

Chapter 3

Hale Sector Boundary: association with solar flares

The work presented in this Chapter has been published in Loumou, K. et al. (2018).

In the first part of this thesis, we probe the link between Hale Sector Boundaries (HSB) and flares. We perform a large statistical analysis, containing more flares than the ones previously considered in the literature, to see if the Hale Sector Boundaries can be used as an indicator for flares that will take place back at the Sun. The concept of the HSBs was presented in Section 1.3 alongside previous research done on the topic.

In this Chapter, in Section 3.1 we present the RHESSI flare database and how it was reduced to be appropriate for our research. In Section 3.2.1 we consider the HSB found from the time of the sector crossing at the Earth, extending the work of Svalgaard et al. (2011) who studied the declining phase of Cycle 23 and extend it for the rising phase of Solar Cycle 24. In Section 3.2.2 we go one step further, by making use of magnetic field extrapolations as an enhanced method of detecting Hale Sector Boundaries. This was done due to the restrictive nature of detecting HSBs from Earth, as explained later. We calculate and present the

HSB-flare distances for all RHESSI flares with longitudes $|\lambda_F| \leqslant 60°$. We compare the two different methods in 3.3. Finally, in Section 3.4 we discuss or results and the advantages and limitations of our methods.

3.1 RHESSI flare data reduction

The Reuven Ramaty High Energy Solar Spectroscopic Imager (RHESSI) flarelist[1] is an extensive list of solar flares[2], from 22-February-2002 to 3-March-2018. It is created by comparing the count rate obtained in the 6 to 12 keV energy band to the background level. In order for an event to start being considered a flare, the recorded count rate must be greater than 3σ above the background or, in the case of South Atlantic Anomaly crossing or data gap, be at least 60% of the background level. If the energy is found in the 6 to 12 keV energy band, then it is characterised as a flare. To view the flarelist as well as complete documentation of its creation information can be found in the RHESSI branch of Solarsoft (Schwartz et al. 2002).

In addition to the flare start, peak and end times there are many additional pieces of information determined for each flare quantifying the conditions during the observation, helping to verify if it is a real flare. These are keywords that according to their value provide information on whether RHESSI was getting in or out of the South Atlantic Anomaly or nightime during the observation, whether the event was of solar origin (or it was due to energetic particles, cosmic rays etc.) or the quality of the data is acceptable. As part of the flarelist being created, quicklook images are produced to determine whether the location of the flare (centroid of its emission) originated on the Sun.

Our research extends from the 12-February-2002 to 23-February-2016, corresponding to the second half of Cycle 23 and the first half of Cycle 24 (including the two maxima the Cycle 24 reached). This time region covers the period of RHESSI's beginning of observation until its fifth anneal. There could be several

[1] https://www.ssl.berkeley.edu/~jimm/hessi/hsi_flare_list.html

[2] A way of flare classification is by measurement of their peak flux of 100-800 pm X-rays near Earth by using the GOES satellite. They are classified as type A,B,C,M or X, with a range of energies from $10^{-8}\ Wm^{-2}$ to more than $10^{-4}\ Wm^{-2}$.

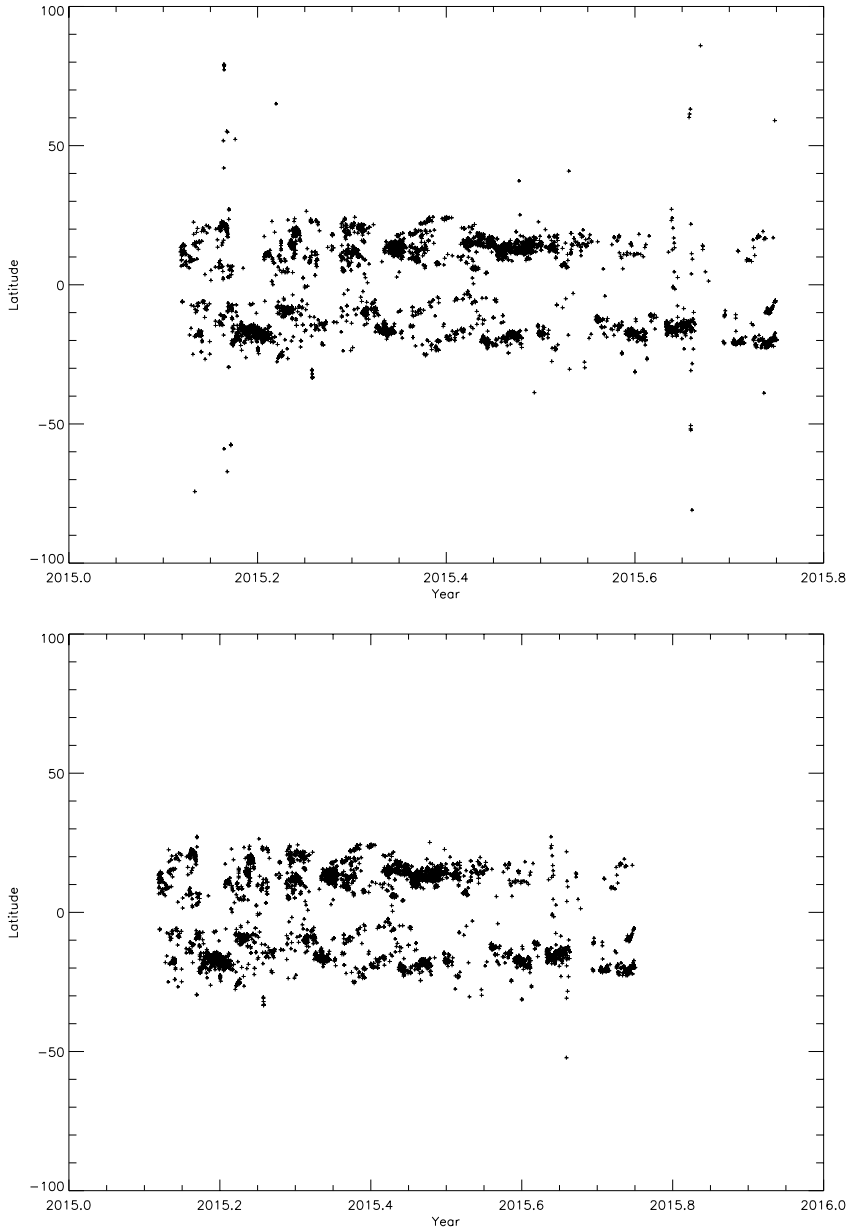

Figure 3.1: Top panel: Example of RHESSI data that have not been corrected for wrong rolling angles. Bottom panel: The same sample, after the correction.

events within the RHESSI flare list that might not be real flares so we have to check their validity. The process of creating our curated flarelist was as follows:

- The initial flarelist for those dates was downloaded via the `hsi_flare_list` procedure Solarsoft. It contained 117,427 events detected from RHESSI, providing their position from the centre of the Sun in arcseconds, start, peak, end time of the flare, the maximum GOES flux during RHESSI flare time and the GOES flux of the background during the pre-flare time that needed to be subtracted.

- Events that the keywords classified as non-solar or of poor quality were excluded, leaving 111624 events.

- For any flares where the GOES flux was not provided, we determined it using the GOES software in Solarsoft.

- If there were no counts from GOES on those times, or the value of the flare corresponded to an event of A1.0 GOES class, then those events were eventually omitted from the list. This step was the reason why most of the flares not in the final list were omitted.

- The background flux was subtracted.

- The heliographic latitude and longitudes were calculated.

- Flares with latitudes of $\geq \pm 50^o$ at the beginning of a solar cycle and greater than 20^o towards its end are identified. For each of these events we recalculate the RHESSI flare position using the routine the flare list uses but with a longer time window for the RAS database to try and obtain a more accurate spin rate and hence location. This corrects the position of many flares but some are still left with unusually high latitudes. An example of this process can be seen in Figure 3.1. For these events we manually verify if the RHESSI flare position is associated with an active region or brightening in EUV. In the vast majority of these cases the position cannot be confirmed and so they are dropped from the list.

- Flares that still had dubious locations (latitude larger that $\pm 45^o$), were manually verified comparing their positions to where active regions were using EUV images from the Atmospheric Imaging Assembly of the Solar Dynamics Observatory. In addition, we investigated whether RHESSI was just coming out from the SAA but was still wrongly documenting this event as a flare. If deemed to be shown on the wrong coordinates or non-solar the events were taken out.

- The result was a flarelist of 73711 events.

An issue not corrected was flares that were classified as two separate events when that was not the case. This can happen when a flare is being recorded and, before it ends, RHESSI crosses the South Atlantic Anomaly for a time in-between. An example of this case is given in Figure 3.2, where a flare is being recorded at time 16:41UT, RHESSI enters the SAA at 16:44UT and resumes operations at 17:03UT. The same flare will be deemed as two separate events in this case.

Due to the length of our flarelist, we adopted a less hands-on approach on checking for this source of error. We focussed on testing that the flarelist satisfies the flare characteristics accepted in literature. More specifically, we produced a Butterfly diagram using the flare latitudes provided by the flarelist (Figure 1.2) to ensure that the latitudes flares appeared at the beginning of the Solar Cycle where about $|35|^o$, and gradually reducing as the time progressed.

Figure 3.3, top left panel, checks that there is a similar amount of events on both hemispheres. There is no reason to have exactly the same number of flares per hemisphere and a certain North-South asymmetry should be expected due to the Rosenberg-Coleman effect. In our list, there were more flares in the Southern hemisphere for the declining phase of Cycle 23 and a balanced distribution for the rising phase of Cycle 24.

In the top right panel, in a plot of the frequency of flares in terms of their background subtracted GOES flux, we find a power-law with the expected index of about -2 (Hudson 1991). One can note the small dip for the very small flares. This is again expected as the smallest events are likely to be under-sampled as they are harder to detected against the background (Hannah et al. 2011).

In addition, in Figure 3.3 bottom panel, the top frame shows the histogram of

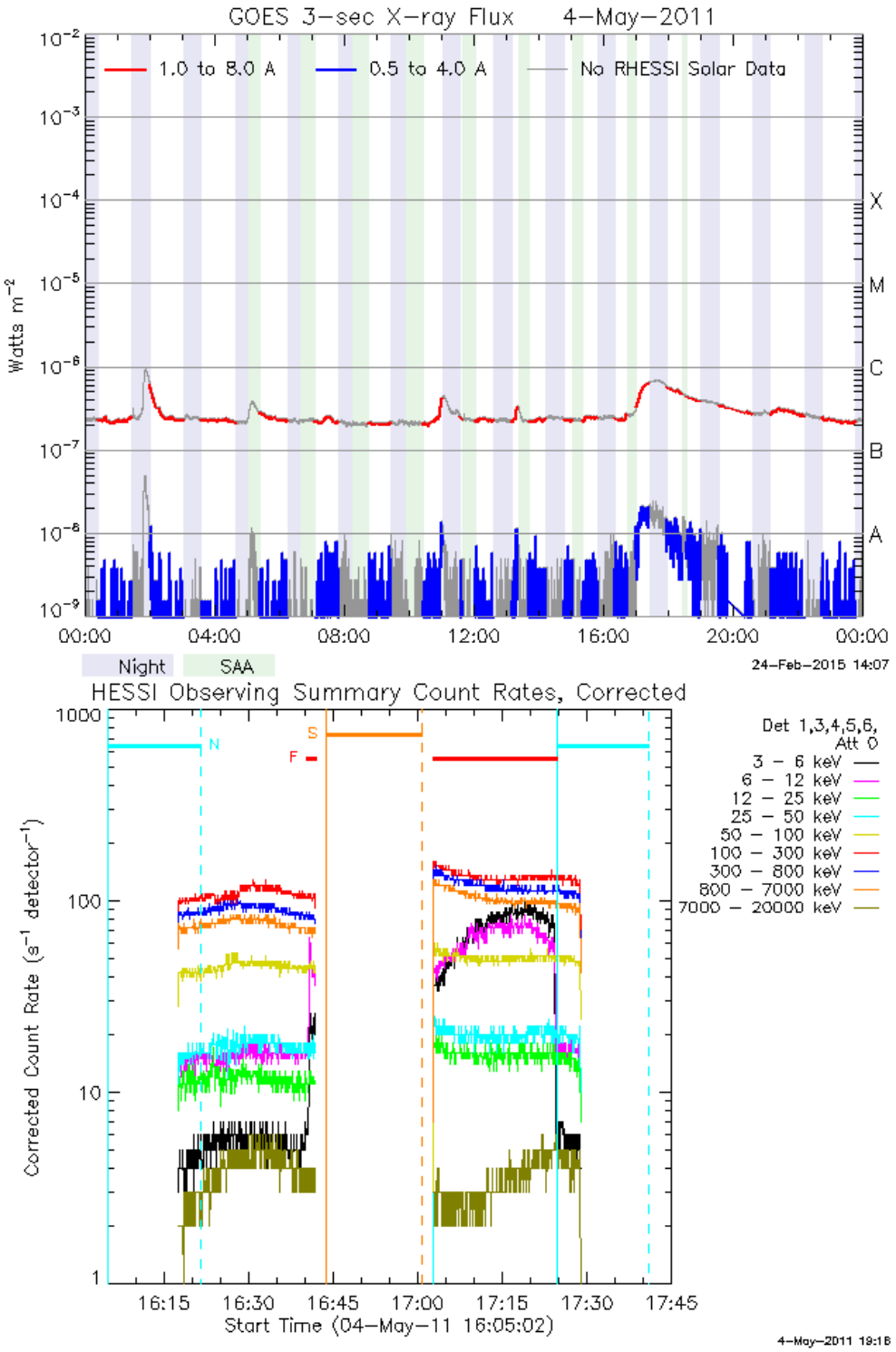

Figure 3.2: Example from the RHESSI quicklook lightcurves (http://sprg.ssl.berkeley.edu/~tohban/browser/). At the top the lightcurves from GOES are given as a comparison. The detected flare is indicated with an F and a red horizontal line. Unfortunately, RHESSI crossed the SAA after the onset, indicated with the orange line and denoted with an S. The cyan line with N is the nighttime. Note that GOES does not efficiently detect the event as the flare is of small intensity.

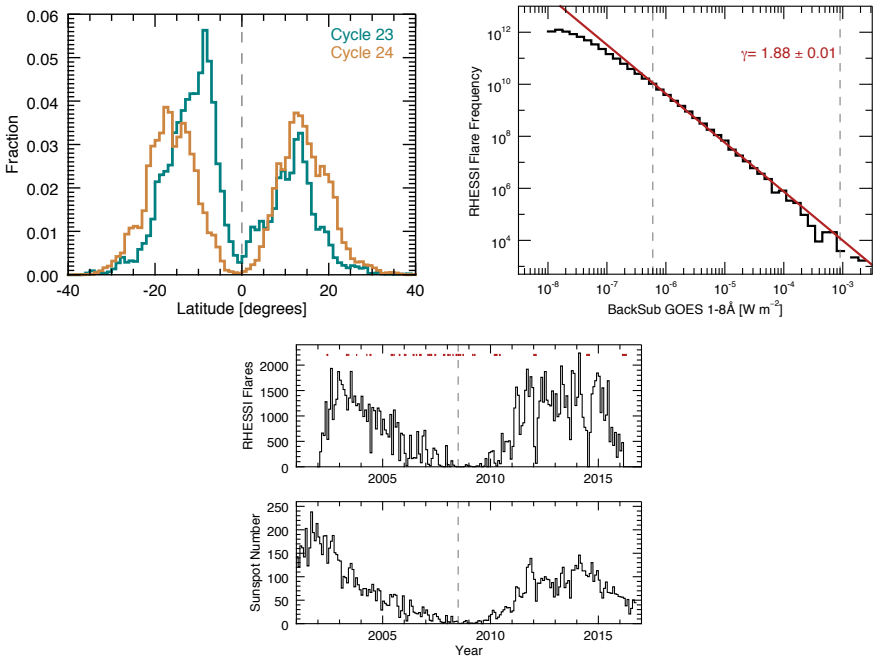

Figure 3.3: Summary of the filtered RHESSI flare list showing a histogram of the latitudes per Cycle (top left), frequency distribution of the flare GOES 1-8Å flux (top right) and number of flares and sunspots versus time (bottom). Note that the power-law fitted to the frequency distribution (red line, top right panel) was found using a Maximum Likelihood Estimator method (Crawford et al. 1970; Wheatland 2004), over the range indicated by the dashed vertical lines, and is not a direct fit to the histogram. The times during which RHESSI was not pointing at the Sun or the detectors were off is indicated by the red bars (bottom panel). Figure from Loumou, K. et al. (2018).

RHESSI flares against time (averaged per month and corrected for the time lost due to eclipse and SAA) and this roughly matches the number of sunspots with time. The two plots are similar but not identical, with some flares seeming to be absent. This is due to a number of factors:

- For the start of the time range considered one of the thin attenuators (shutters) of RHESSI was in operation, reducing the sensitivity of the instrument,
- RHESSI was in anneal or the detectors were not in operation (shown in the plot as horizontal red dashed lines),
- the instrument was pointed at non solar sources[3], such as the Crab Nebula.

Finally, the diagram of Figure 1.2 was also used to determine the beginning of Cycle 24 as July 2008, indicated by the vertical line in the plot. That was the time flares happening during Cycle 23 seemed to stop occurring, before a B and C-class flares reappeared at $+40^o$ latitude. Since sunspots are a subset of active regions, which are the location of the origin of flares in most cases, that was an acceptable way of determining the onset of the new Cycle.

3.2 Hale Sector Boundary and flares

3.2.1 Earth Sector Crossing approach

3.2.1.1 Method

We use the method of identifying the sector boundary crossing from Earth, developed by Svalgaard (1968) and Mansurov (1969) independently, presented in Section 1.3. Ground-based data provide information about the perturbation of the Earth's magnetic field as measured from stations situated in the Antarctic and the North Pole. The time the two stations observe a polarity change, corresponds to the time the sector boundary was at the Central Meridian (CM) back at the Sun, about 4.5-6.5 days before, the average time the solar wind needs to propagate towards Earth.

[3]Those times can be found at:http://sprg.ssl.berkeley.edu/~tohban/offtimes.txt

In this part of the analysis, we apply the method described in Svalgaard et al. (2011) using both the boundary crossing times as well as the flaring times reported in the RHESSI flarelist presented above. The scope is to identify the position of the flares around the time the sector boundary was at CM, see whether the majority of the flares took place above the part of the boundary that corresponds to the definition of the HSB and finally, to calculate the HSB-flare distance.

The times the sector boundary was at the CM are provided by Leif Svalgaard at `http://www.leif.org/research/sblist.txt`.

From the 73711 events of the RHESSI flarelist, we selected a subset of those with:

- latitudes less than 55^o,
- GOES class greater than $10^{-8}\mathrm{Wm}^{-2}$ (A class),
- time of occurrence 4.5-6.5 days from the time a boundary is identified at Earth (which had the most significant impact on the number of flares left for the study).

This choice of flaring time allowed for a ± 1 day variability in the solar wind speed, also reflecting the fact that those measurements are simply a proxy of what is happening back in the Sun. In fact, Bumba & Obridko (1969) and Dittmer (1975) found that flares prefer to occur in this particular time period. Getachew et al. (2017) followed a similar process to the one presented in this Chapter to study the temporal variation of HSBs, where they used the measured solar wind speed and not an approximation. However their approach returned similar results to ours (for more insight on temporal variations of HSBs see Chapter4) and therefore we think the assumption of 5.5 days average solar wind speed is appropriate.

The constraints resulted in only 9189 flares remaining.

3.2.1.2 Results

To compare the positions of HSBs and flares, we produced two dimensional histograms (Figure 3.4) of latitude versus longitude for the flares selected. There are two separate histograms, one for sectors indicating a change in magnetic field polarity from negative to positive ($-,+$: blue colour) and one for sectors indicating

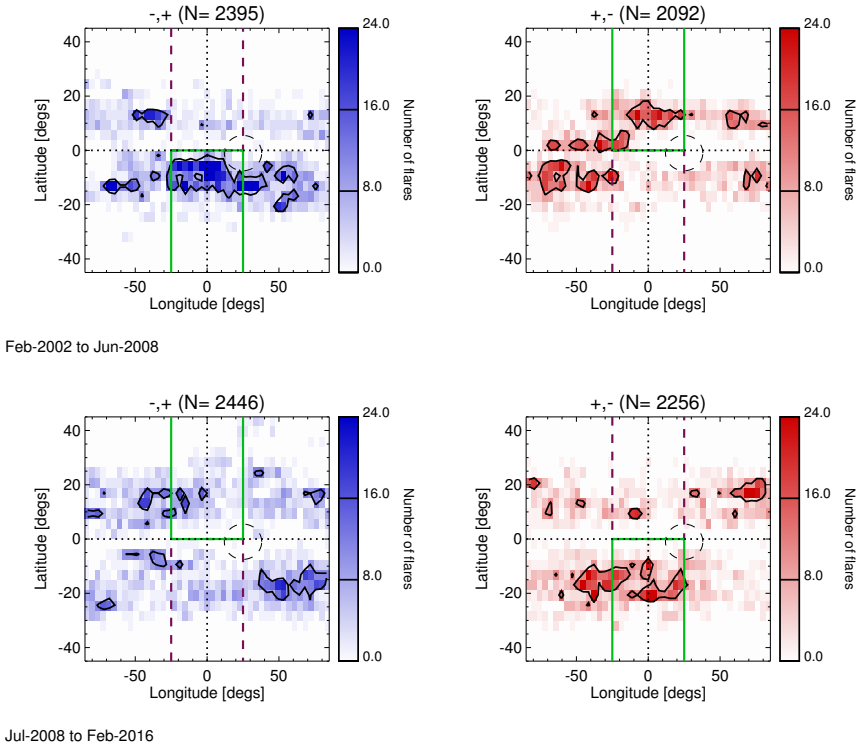

Figure 3.4: Distribution of the RHESSI flares that occur when the HSB-Earth was at central meridian, separated by the polarity change at the boundary: left (blue) for negative leading positive (-,+), right (red) for positive leading negative (+,-). In the top row we show the flares during Cycle 23 (Feb 2002 to July 2008) and bottom row for Cycle 24 (July 2008 to Feb 2016). The green lines indicate the hemisphere in which the HSB is located. The dashed circle indicates the approximate region from which RHESSI cannot determine a flare's location. The purple dashed lines indicate ±25° of meridian, the range used for the histograms in Fig. 3.5. Figure from Loumou, K. et al. (2018).

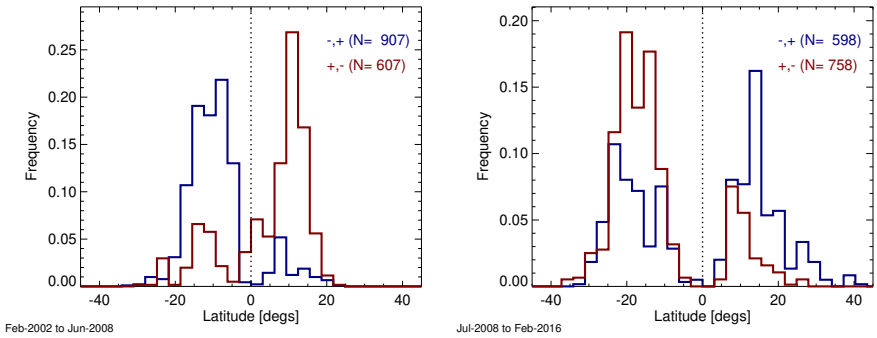

Figure 3.5: Latitude histograms of the RHESSI flares with longitudes $|\lambda_F| \leqslant 25°$ during the times the HSB was at central meridian. The histograms are separated into those from Cycle 23 (left) and Cycle 24 (right) and by the polarity change at the sector boundary of positive leading negative (+,- red) and negative leading positive (-,+ blue). Figure from Loumou, K. et al. (2018).

a change in magnetic field polarity from positive to negative $(+,-$: red colour). The flares are separated for those happening on Cycle 23 and Cycle 24 as well as flare corresponding to a (+,-)or (-,+) sector crossing, in order to be plotted at the appropriate histogram. The HSBs are located at longitude 0 of the parts of the 2D histograms signalled with a solid green box. The purple dashed line boxes indicate the non-Hale boundaries.

In the top row of Figure 3.4 we reproduce the results of Svalgaard et al. (2011) for the end of cycle 23. We find that there is a clear association between HSB and the occurrence of flares that took place about a day before or after the HSB at CM.

In Figure 3.4 bottom row, we extend the research for the first half of Cycle 24. As expected, there is a flip in the polarity from North to South. The correlation seems to be smaller but crucially the association is still present, especially for the part of the sector indicating a change in polarity (+,-). However, no clear association is been shown for the (-,+) boundary apart from a few flares starting taking place around HSB.

To have a better understanding of the distribution of flares around the HSB, we focus on the distribution of the flares located nearest to central meridian, inside the solid green and dashed red boxes of Figure 3.4. Figures 3.5-3.6 show 1-D histograms of flares occurring about HSB time and longitudes $|\lambda_F| \leqslant 25°$.

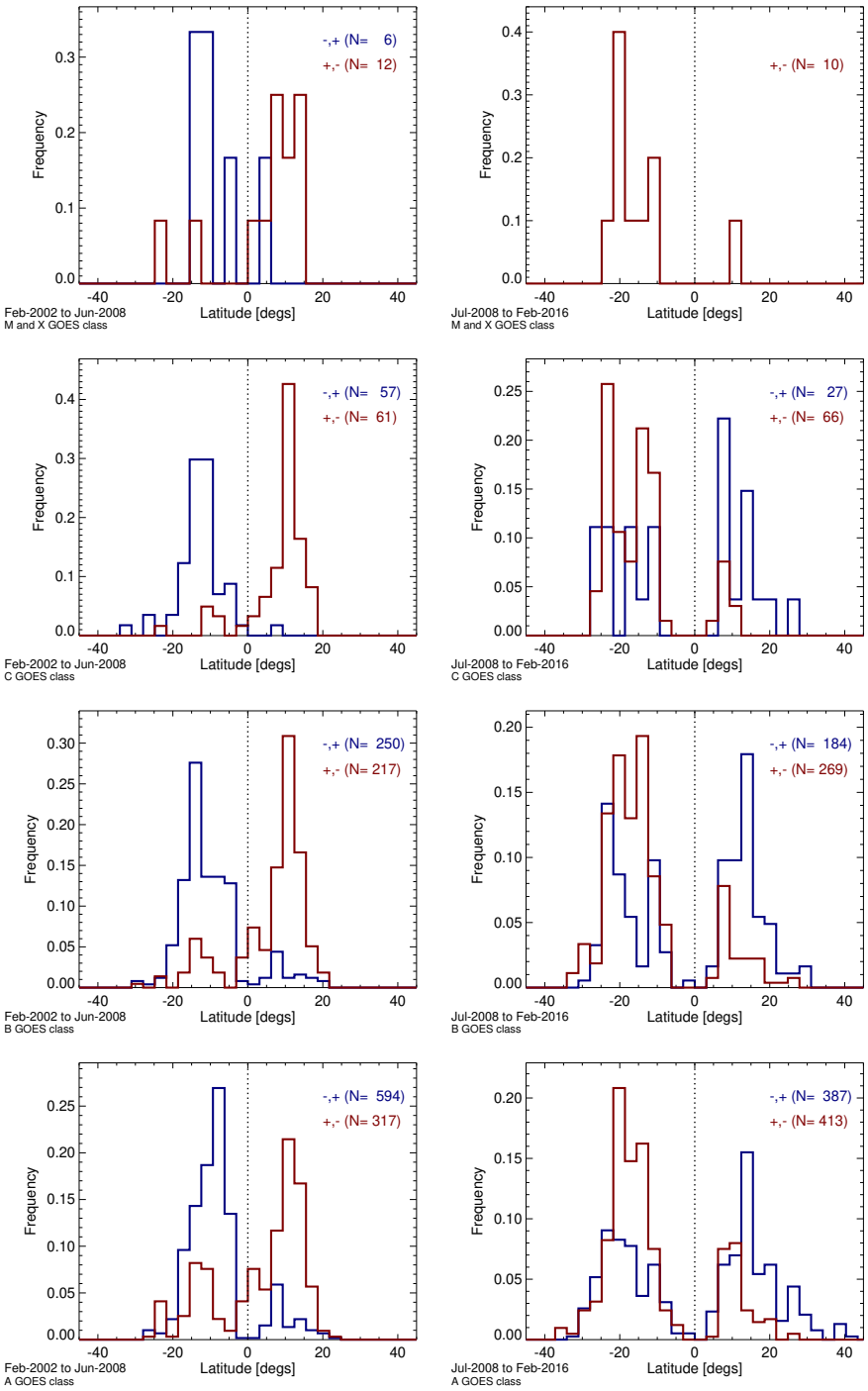

Figure 3.6: Latitude histograms of the RHESSI flares with longitudes $|\lambda_F| \leqslant 25°$ that occurred when the HSB was at central meridian. In the left column are data for Cycle 23 and the right for Cycle 24, separated by GOES class (top row X/M-class then C, B, and A-class on the bottom row). The colours indicate the polarity change at the sector boundary, with blue as (-,+) and red as (+,-). Figure from Loumou, K. et al. (2018).

The histograms were performed for all flares (Figure 3.5) as well as for each class separately (Figure 3.6). These plots exhibit the association of HSB and flares more clearly, for both solar cycles. In all cases, the hemisphere with the HSB present had a higher frequency of flares. Even for the dubious (-,+) HSB of Cycle 24, in Figures 3.5 we still see the distribution of Northern flares peaking around HSB (Figure 3.5, blue right panel) as well as having a non-trivial number of flares in the Southern hemisphere. Figure 3.6 shows that the association is not dependent on the magnitude of the flare.

3.2.2 Potential Field Source Surface extrapolations approach

Using the times of HSBs at CM produces a spatial constraint. In the approach of Section 3.2.1 (which we will now call HSB-Earth), the CM becomes the only location on the Sun we can determine the position of the boundary between two sectors from Earth. However, there is a larger number of HSBs existing at the same time and being able to take them into consideration would have a positive impact in our statistics. Furthermore, there are HSBs at all times and not only when they cross CM. Additionally, the HSB-Earth approach does not give us any insight on the latitude of the HSBs. Finally, it is dependent on the assumption that the solar wind propagated ballistically, which itself is a simplification.

3.2.2.1 Method

In this section, we present a method of using Potential Field Source Surface extrapolations (PFSS) (Altschuler & Newkirk 1969; Schatten et al. 1969) to determine the magnetic field of the Interplanetary Magnetic Field at distances much closer to the Photosphere (a method we will now call HSB-PFSS). The model as well as the magnetic data products we utilise were created by M. DeRosa and K. Schrijver, and are publicly available[4]. A PFSS extrapolation assumes harmonic expansion of the photospheric field and solves the Laplace equation in a spherical volume (Lockwood 2013). It shows the expansion of the field from a lower boundary of $1R_{\odot}$ to an outer boundary of $2.5R_{\odot}$. An additional advantage of this method is

[4] http://www.lmsal.com/~derosa/pfsspack/

the extensive documentation about it in IDL, which is the programming language we used for this analysis. We retain only the outer layer of the radial magnetic field component at a distance $2.5R_{\odot}$. This is the furthest distance from the Sun the extrapolation can provide.

The process step-by-step is as follows:

- A routine in IDL was written that downloads the files of an already computed PFSS, which calls the routine $pfss\_time2file$ in solarsoft, daily at 12:04UT.
- For each date, the code restores the extrapolation corresponding to a distance of $2.5R_{\odot}$ and keeps only the data we are interested in; the value of the radial magnetic field, the latitude and the Carrington Longitude (used later in Chapter 4).
- For each flare in the flarelist, we keep its latitude in a variable.
- For the identified flare latitude, we store the values of the radial magnetic field (Br) in all longitudes in an array.
- We identify the location of a sector boundary as follows: We move stepwise in the Br array, calculating the product of $\mathrm{Br}_i \times \mathrm{Br}_{i-1}$. If the product is negative, there was a change in the polarity, therefore position i is the location of the sector boundary.
- According to the whether the solar cycle was odd or even and whether the boundary was in the Northern or Southern hemisphere, we classify that boundary as Hale (odd cycle: northern hemisphere: positive to negative, odd cycle: southern hemisphere: negative to positive, the opposite for an even cycle) or non-Hale (odd cycle: northern hemisphere: negative to positive, odd cycle: southern hemisphere: positive to negative, the opposite for an even cycle).

A limitation of this method is that again we do not consider variations of the solar wind speed between the Photosphere and the source surface. However, we still manage to look at the large-scale magnetic field while being much closer to the Sun, with is an improvement from the HSB-Earth method.

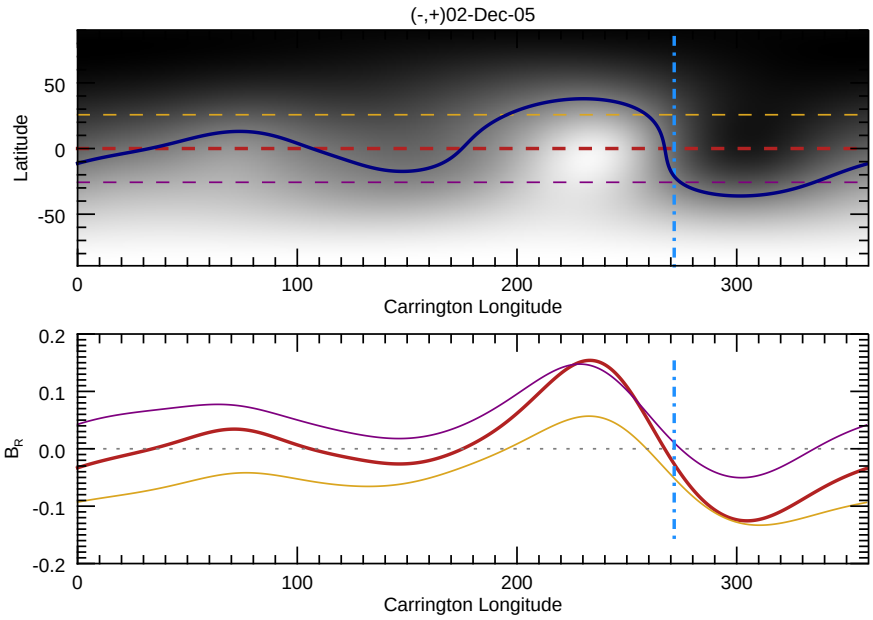

Figure 3.7: On the top: Magnetic field extrapolation of the radial magnetic field at a distance $2.5R\odot$, given per Carrington longitude and Heliographic latitude. Over-plotted with a dark blue curve is the sector boundary, as given by the contouring procedure in IDL. The three dashed, horizontal lines (in yellow, red and purple) create a "cut-through" for a specific value of latitude. They are plotted on the bottom, illustrating the value of the radial magnetic field in said latitudes, for all Carrington longitudes. The vertical, light blue line shows the position of the Central Meridian. On the bottom: The three curves give the value of the radial magnetic field for latitude indicated at the top half of the figure with the coordinated coloured horizontal, dashed line. The vertical, light blue line shows the position of the Central Meridian.

Figure 3.7 gives an example of the result of our method and provides a way to test that the code works as it should. We select a date corresponding to 5.5 days before a boundary crossing detected on Earth. In Figure 3.7 the top panel represents the values of the radial magnetic field, with three chosen latitudes -25, 0 and 25, represented by the three horizontal dashed lines. A contouring procedure inbuilt in IDL gives the structure of the sector boundary, as it would be seen from ecliptic view, shown here with a blue curve. Figure 3.7 bottom panel, for each of the previous cuts, the value of the radial magnetic field per longitude is given. On both panels the position of the CM is indicated by a vertical light blue line. Following the horizontal cuts in latitude for every step in longitude in the top panel (so imitating what code does), the longitudes where we meet the boundary of the sectors (dark blue curve) correspond to the same longitudes the magnetic field changes polarity in the bottom panel. Figure 3.7 proves the algorithm behaves as expected.

Figure 3.8 shows multiple examples of this approach for dates 5.5 days before a boundary crossing detected at Earth, with a colour scheme to match that of Figure 1.5. Yellow and blue represent the positive and negative polarities of the PFSS Br at $2.5R\odot$, the black curve shows the sector boundary, while the Hale parts of the boundary are indicated with thick brown curves. The refined flarelist of Section 3.2.1, with the same restrictions imposed, gives the position of all flares occurring ± 1 day from the date of boundary crossing at CM. These are overplotted with red diamonds.

In Figure 3.8 top row, we present examples of a two-sector (left) and a four-sector (right) structure during Cycle 23. The plots show a HSB at CM, as they should, flares occurring above the HSB or very close to it as well as some flares elsewhere on the disk (eg. 07-Jun-03 at longitudes -100 arcsecs). In Figure 3.8 middle row, we show another two cases of a two-sector (left) and a four-sector (right) structure during Cycle 24. The plots show a HSB about -20^o in longitude away from CM. For these cases it could be that the solar wind speed assumed was slower than the real value. In reality, it must have taken less time for the polarity reversal to be propagated from Sun to Earth. The profile of the RHESSI flares is again the same, with flares occurring above, near and further away from HSB. Finally, in Figure 3.8 bottom row, we showcase instances of the boundary

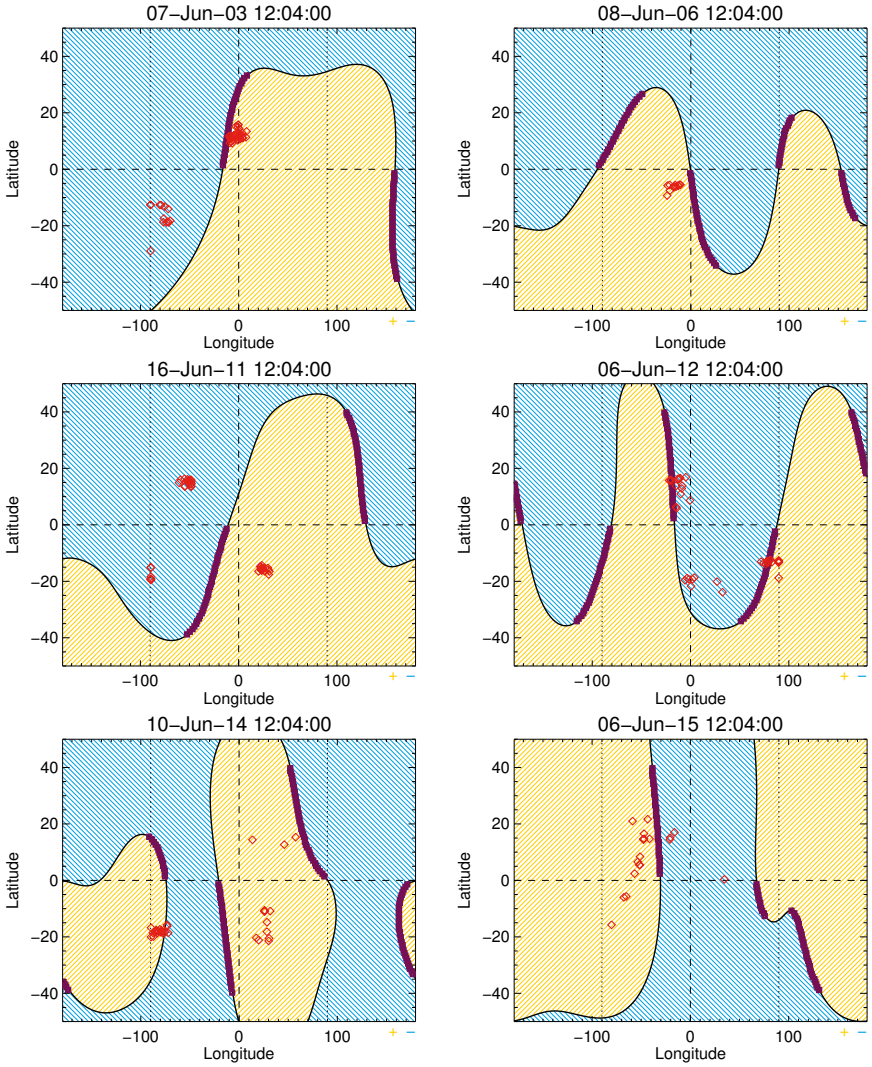

Figure 3.8: Examples of PFSS extrapolations showing the radial magnetic field component at the outermost surface ($2.5R_{\odot}$) for six different dates, on which the HSB-Earth are predicted to be at central meridian. In the intensity map blue is negative polarity, yellow is positive, with the black line being the sector boundary (neutral line). Overplotted are the RHESSI flares (red crosses) that occurred within 1 day. The parts of the sector boundary marked with purple points are the HSB, found out to ±40° latitude. Figure from Loumou, K. et al. (2018).

that has a much more complicated structure. These are again from Cycle 24 and we see HSBs at longitudes before the CM, likely due to faster solar wind. One of the largest deviations found was on 06-Jun-15 (bottom right) where the HSB occurred 30° before CM, equal to two days before. However, even in that case it is still being detected, it is at the correct hemisphere and is associated with flares. Figure 3.8 reinforces the theory that there is an association between HSBs and flares.

3.2.2.2 Results

Using the HSB-longitudes determined from the PFSS analysis and the flare longitudes as given from the RHESSI flarelist we calculate the HSB- flare distance, $\lambda_{HSB} - \lambda_F$. Due to the identification of multiple HSBs in one day, we added two further features on the process to identify the closest HSB per flare:

- We omitted flares close to the limb ($|\lambda_F| \geqslant 60°$) to avoid projection effects.
- We calculated all distances between a flare and all HSBs identified for the latitude and kept the shortest distance only.

For the HSB-PFSS approach our flarelist has 18,072 flares for Cycle 23 and 22,493 for Cycle 24. Even though that is not the full RHESSI flarelist, it is considerably more flares than we looked at using the HSB-Earth approach in Section 3.2.1.

The results (top row), alongside with their cumulative form (bottom row), are given in Figure 3.9. The plots in the left column refer to cycle 23 and in the right column to Cycle 24.

Figure 3.9, top row, the histograms show the HSB-flare distance peaking at about 0. On the left, for Cycle 23, the northern hemisphere peaks more clearly than the southern, with several flares on the southern hemisphere further away from HSB ($\lambda_{HSB} - \lambda_F < 0$). On the right, for Cycle 24, again there is a clear peak of flares around HSB ($\lambda_{HSB} - \lambda_F \simeq 0$), with some in the southern hemisphere appearing further away $\lambda_{HSB} - \lambda_F \simeq 70°$.

In Figure 3.9, bottom row, we give the cumulative distributions of those results (with dark blue for (-,+) HSBs and red for (+,-) HSBs). In an attempt

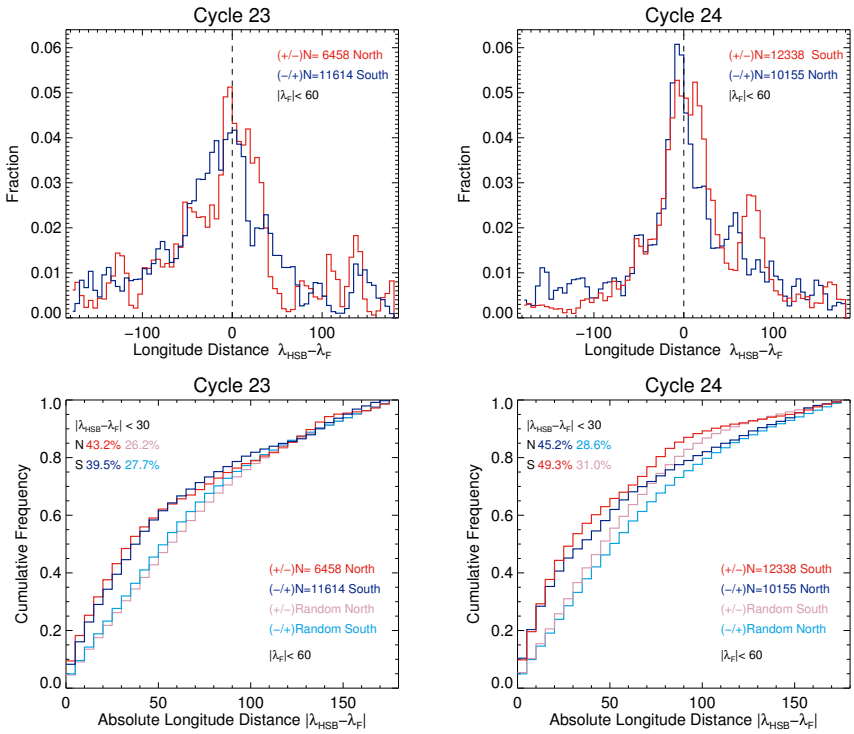

Figure 3.9: Longitudinal distance histograms (top row) of RHESSI flares with $|\lambda_F| \leqslant 60°$ from the HSB PFSS, for solar Cycle 23 and 24 (left and right columns). With red, the change in polarity from positive to negative and blue from negative to positive. Cumulative distributions of these histograms (bottom row), with additional cumulative distributions over-plotted that were produced from a set of flares with longitudes drawn from a random distribution (pink for change in polarity from positive to negative and light blue for change in polarity from negative to positive). Figure from Loumou, K. et al. (2018).

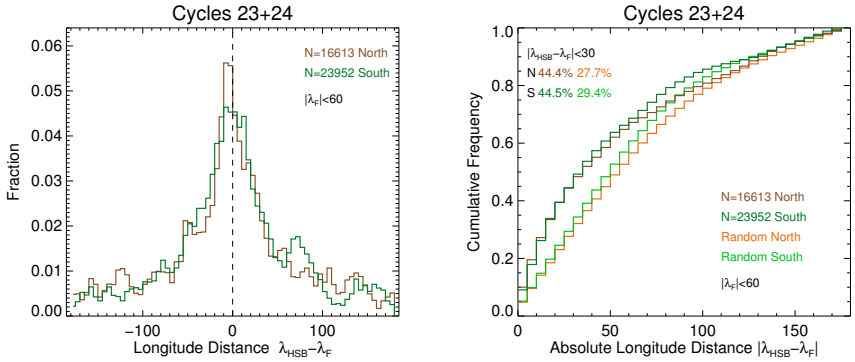

Figure 3.10: Longitudinal distance histograms (left) of RHESSI flares with $|\lambda_F| \leqslant 60°$ from the HSB PFSS, for solar Cycle 23 and 24 combined. With brown, all the flares located in the northern hemisphere and with dark green all the southern flares. Cumulative distributions of these histograms (right), with additional cumulative distributions over-plotted that were produced from a set of flares with longitudes drawn from a random distribution (orange for northern and light green for southern). Figure from Loumou, K. et al. (2018).

to test whether our findings are statistically significant, we additionally assumed a random set of flare longitudes, calculated the cumulative histograms of their distance to the same HSBs as before and overplotted the result (light blue and pink). During Cycle 23, the HSB-flare distance was within $|\lambda_{HSB} - \lambda_F| \leq 30°$ for about 43% of flares on northern hemisphere, and for about 40% of flares on the southern hemisphere. During Cycle 24, the HSB-flare distance was within $|\lambda_{HSB} - \lambda_F| \leq 30°$ for about 45% of flares on northern hemisphere, and for about 49% of flares on the southern hemisphere. The histogram for the random set of flare longitudes shows a weaker association of HSBs-flares (Cycle 23, 26% north, 28% south; Cycle 24, 29% north, 31% south), implying that our findings are statistically significant.

Figure 3.10 shows the distribution of all flares around HSB in this section, for both solar cycles (left: histogram, right: cumulative histogram with the cumulative histogram from the random sample overplotted, brown line: Northern flares, green line: Southern flares). Roughly 44% of all flares took place no further than 30° from HSB. The association is clear in both hemispheres with a sharper profile in the Northern hemisphere.

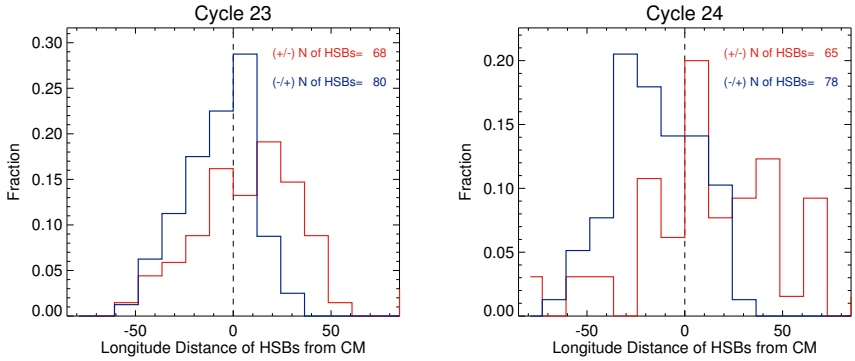

Figure 3.11: Longitudinal distance of the HSB PFSS on the days they were predicted to be at central meridian by the HSB-Earth method, for the days RHESSI observed flares. For Cycle 23, 89% of HSB PFSS with polarity change (-,+) were no further than 30^o away from central meridian, while the percentage for the HSB PFSS (+,-) was 68%. For Cycle 24 68% of HSB PFSS (-,+) were within 30^o of central meridian, with 66% for HSB PFSS (+,-). Figure from Loumou, K. et al. (2018).

3.3 Comparison of the two approaches

As the HSB-PFSS approach provides the locations of all the HSB at any time, we can compare the results to those for HSB-Earth, checking the accuracy and validity of those two methods.

We are taking a subset of HSB-PFSS only for:

- times where there is a HSB at CM - as we did in order to produce Figure 3.8,
- the equator - as the HSB-Earth provides no insight on which latitude the HSB is located,
- times there were RHESSI flares - as we are only interested in the behaviour of the HSBs when there is flaring activity.

By calculating the distance for these selected HSBs from CM, we should get a histogram with a peak about 0. The results are presented in Figure 3.11, per cycle and HSB polarity change. During Cycle 23 there is a peak either on or very close to CM, with 89% within 30^o for the (-,+) change and 68% for (+,-). At the same time, during Cycle 24 the respective values are 68% and 66% per HSB

polarity change. An interesting result is the distinct clear peak about 30^o before CM during Cycle 24's (-,+) change. This agrees with Figures 3.4 (bottom left) and 3.5 (right panel) where the HSB-flare association seemed not to be as sharp. Our analysis indicates that, for the northern hemisphere, the HSB appeared about 2 days later than we supposed on Section 1.3, so the solar wind Sun-Earth travel-time in reality was 2.5 to 4.5 days.

3.4 Summary and Conclusions

In this Chapter, we proved the association between a feature of the large-scale solar magnetic field and the occurrence of solar flares. We used two independent approaches, one initially performed by Svalgaard et al. (2011), using ground based data as an approximation of the conditions at the Sun and one making use of magnetic field extrapolations, at a distance $2.5R\odot$ in order to get a map of the magnetic field.

With the HSB-Earth method, we confirmed the results of Svalgaard et al. (2011) as well as showed that the same applies for solar Cycle 24. Our extension of their work has shown that the HSB hemispheres do swap as we change from Cycle 23 to 24. However the HSB-Earth association is not as clear in Cycle 24, especially in the northern hemisphere. This could be attributed to a larger variability of the speed of the solar wind in the northern hemisphere. In fact, Getachew et al. (2017) used the observed solar wind speed to determine the time of HSB at central meridian, finding a sharper association to flares. Although even with this approach found a weaker occurrence pattern for Cycle 24 in both hemispheres compared to Cycle 23. Despite this, we are still able to show a concentration of flares in the expected hemisphere associated with the HSB, even separated by GOES class. The same association works for large X-class flares down to A-class microflares.

The HSB-PFSS method provided a much larger statistical sample, allowing HSBs to be found for all times and flares. This resulted in a clearer picture of the sector structure closer to the solar surface, and one that is not affected by variations in the solar wind speed. We showed that 41% of flares for Cycle 23 and 47% of Cycle 24 flares with longitudes $|\lambda_F| \leq 60^\circ$ were located in distance no

further that 30^o from a HSB.

The advantage of the PFSS approach is that we achieve a near-instantaneous view of the structures on the Sun.

In order to avoid any impact of intense individual active regions, it would be interesting to investigate the behaviour of the HSBs over the period of numerous days. Another point to keep in mind is that extrapolations additionally have their own limitations, due to the approximations made and our limited knowledge of the physics governing the solar magnetic field. Therefore, enhancing the previous codes in order to fine-tune the HSB-flare distance does not necessarily promise more trustworthy results. Despite any limitations of the PFSS method, it is a valuable tool for enhancing flare forecasting as it enables the user to have an almost real time picture of the solar magnetic field while making more informed decisions as to which active region might lead to an eruption.

Our comparison between the HSB-Earth and HSB PFSS approach seems to suggest that in Cycle 24 the mean solar wind is faster than we assumed, with the actual HSB lagging behind where HSB-Earth predicted it to be. Getachew et al. (2017) used the observed solar wind speed to determine the time of HSB at central meridian, finding a sharper association to flares. Although even this approach found a weaker occurrence pattern for Cycle 24 in both hemispheres compared to Cycle 23. Despite this, we are still able to show a concentration of flares in the expected hemisphere associated with the HSB, even separated by GOES class. The same association works for large X-class flares down to A-class microflares.

Chapter 4

Hale Sector Boundary: association with active longitudes

Part of the work presented in this Chapter has been published in Loumou, K. et al. (2018)

In this Chapter we are focussing on the behaviour of the Hale Sector Boundaries with time and search for a consistent pattern in the paths they follow. We then compare those with identified paths of another structure of the large-scale magnetic field, Active Longitudes (see Chapter 1, Section 1.4). Section 4.1 presents the migration paths of the HSBs in a Carrington System. In Section 4.2 we contrast these HSB paths with the Active Longitude results of Gyenge et al. (2016). Although there is some similarity in the behaviour of the HSB and Active Longitude, they only overlap occasionally. Ultimately, we show that there is not enough evidence to suggest HSBs and Active Longitudes are the same feature.

4.1 Temporal behaviour of Hale Sector Boundaries

The poorer association of HSBs with flares for solar cycle 24 (Chapter 3, Sections 3.2.1 and 3.2.2) suggests the need to investigate their behaviour over a larger time range.

We present the location of the sector boundary through plots of its Carrington Longitude over its Carrington Rotation. This rotation system, chosen in order to avoid correcting for differential rotation, assumed the whole solar disk to have a steady rotation rate of 25.38 days[1]. We calculated the Carrington Rotation and Carrington Longitude, for the times the sector boundary was recorded on Earth to be at Central Meridian (CM) back at the Sun ±1 day - the HSB-Earth method of Chapter 3).

We produced Carrington maps for each cycle individually as well as for each change in polarity. Figure 4.1 shows the resulting plot for Cycle 23 (top) and Cycle 24 (bottom). Finally, the results were combined in order to give a complete representation of the temporal behaviour of the sector boundary, Figure 4.2. Note that in Figures 4.1 and 4.2 we have also overplotted with double the Carrington Longitude values to help identify repeating patterns.

For the rising phase of Cycle 23 (Figure 4.1, top two panels and Figure 4.2, left part of the figure) the HSB Carrington longitude vs Rotation number is relatively flat, showing that it is moving with the Carrington frame. Then about the year 2000 it starts to increase, showing that the HSB is moving faster than the Carrington rate. Up to 2002 there is also a four-sector pattern which transitions into a two-sector pattern through to 2004, after which the fours sectors appear again. As Cycle 23 heads into solar minimum during 2007 onwards, the two-sector pattern returns, but the HSB is still migrating faster than the Carrington rate. For Cycle 24 (Figure 4.1, bottom panels) the HSB slows down and moves slower than the Carrington rate until about 2013 when the pace is peaking up again. Throughout the time of Cycle 24 plotted here the four-sector structure has been

[1] http://www.bu.edu/cism/cismdx/ref/Labs/2005_AFWA_ShortCourse/Lab04/refs/CoordinateSystems.pdf

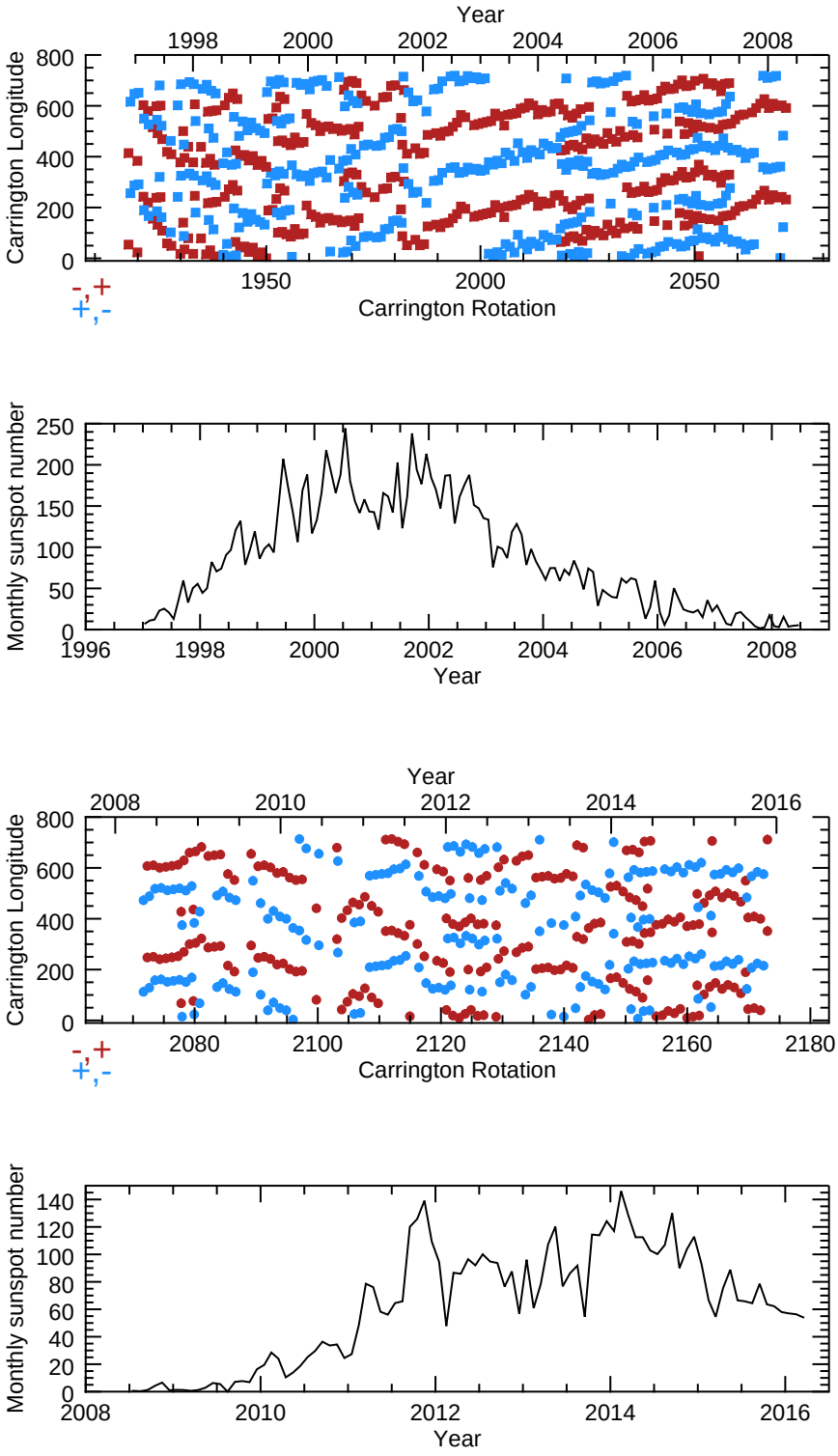

Figure 4.1: Longitude per Carrington rotation of CM at times a sector boundary was present, for cycle 23 (top) and Cycle 24 (bottom), with the sunspots number plotted underneath. The y axis has been plotted for 720^o instead of 360^o in order to have a clearer view of any effect. Sunspot number taken from `http://www.sidc.be/silso/datafiles`.

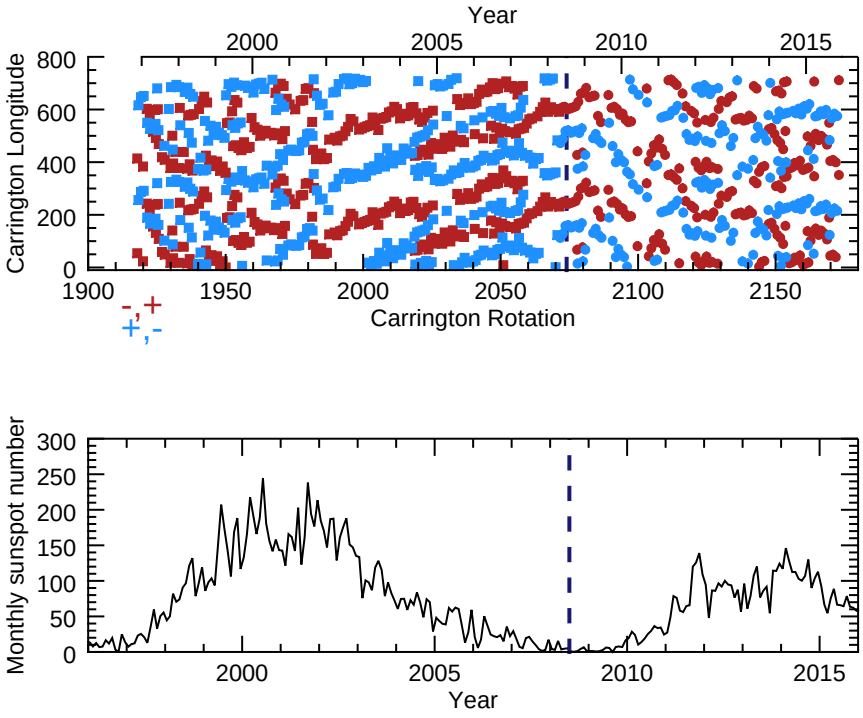

Figure 4.2: Longitude per Carrington rotation of CM at times a sector boundary was present, for solar cycles 23 and 24 combined, with the sunspots number plotted underneath. The y axis has been plotted for 720^o instead of 360^o in order to have a clearer view of any effect. Sunspot number taken from `http://www.sidc.be/silso/datafiles`.

maintained.

A clear impression that is left from these graphs is the less distinct, more chaotic paths of the HSBs during the rising phase of a Solar Cycle and the more organised trails they follow during the declining phase of the Cycle, in agreement with Getachew et al. (2017). An assumption for this behaviour is that as the new Cycle commences, the global magnetic field enters a period of reversal, where it finally reverses at about the solar maximum, This has an effect on its configuration in the Heliosphere as well. Hence the more chaotic trail of the HSB in the rising phases of Cycles 23 and 24.

4.2 Hale Sector Boundaries and Active Longitudes

We compare our HSB-Earth positions to the Active Longitudes found by Gyenge et al. (2016). The location of the Active Longitudes was determined via sunspot observations in the Debrecen photoheliographic data (Baranyi et al. 2016; Győri et al. 2017), and crucially they are given without a differential rotation being applied (private communication Gyenge 2017). These data have a weighted concentration of sunspot group area by Carrington rotation, with a high-pass filter applied to remove weaker and noisier regions. This can result in some Carrington rotations having no identified Active Longitudes as they are too faint or weak. The Carrington phases, i.e. Carrington longitude/360°, of the Active Longitudes are calculated. The Carrington phases for three additional whole rotations are also plotted so that the path of the dominant active longitude, relative to the Carrington frame over several rotations, can be identified. Repeated regions outside of this path are removed.

The resulting migration paths of the Active Longitudes over Cycles 21 to 24 are shown in Figs. 4.3 and 4.4, for the northern and southern hemispheres respectively, as points connected by a line with an uncertainty region of 20° to account for the longitudinal bins used. Over a solar Cycle, these generally show a "parabolic migration path" (Gyenge et al. 2016), with the phase initially increasing with time (due to rotation faster than the Carrington rate) before levelling out and

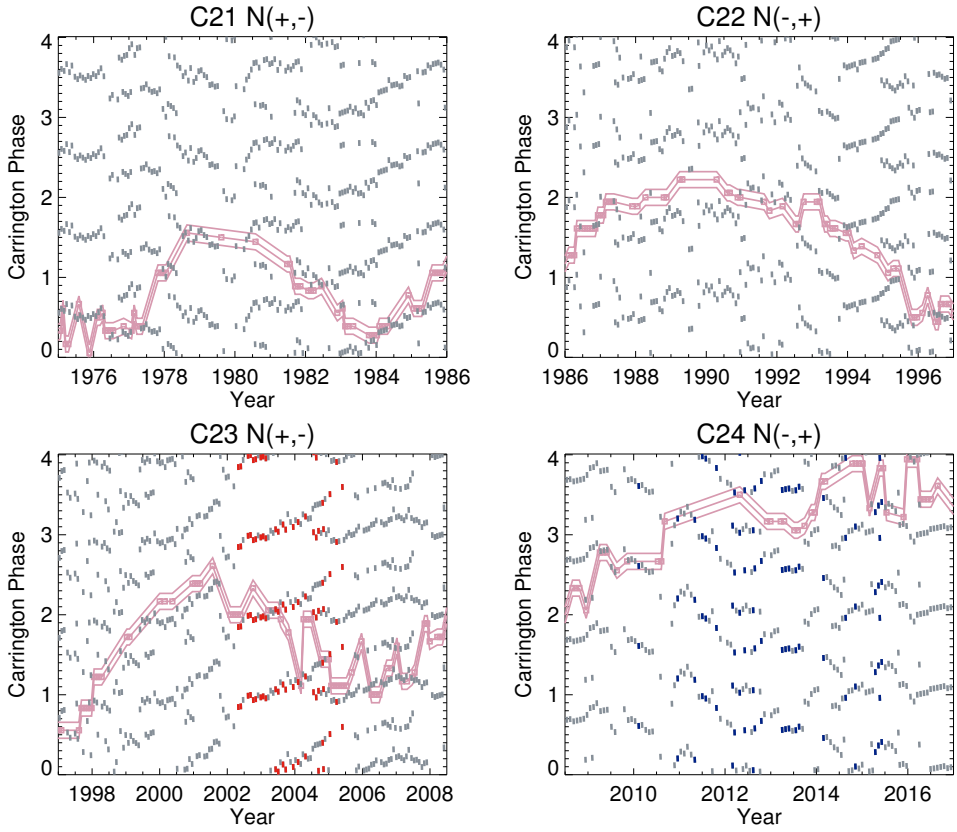

Figure 4.3: Carrington phase against year for the HSB at central meridian over Cycles 21 to 24 (top left to bottom right) in the northern hemisphere. The HSBs which had at least one RHESSI flare occuring nearby (within ±25° longitude) are coloured instead of grey, based upon the polarity change, either (+,-) red and (-,+) blue. Also shown are the observed active longitude positions (pink squares) with an uncertainty region of 20° adapted from Gyenge et al. (2016). Figure from Loumou, K. et al. (2018).

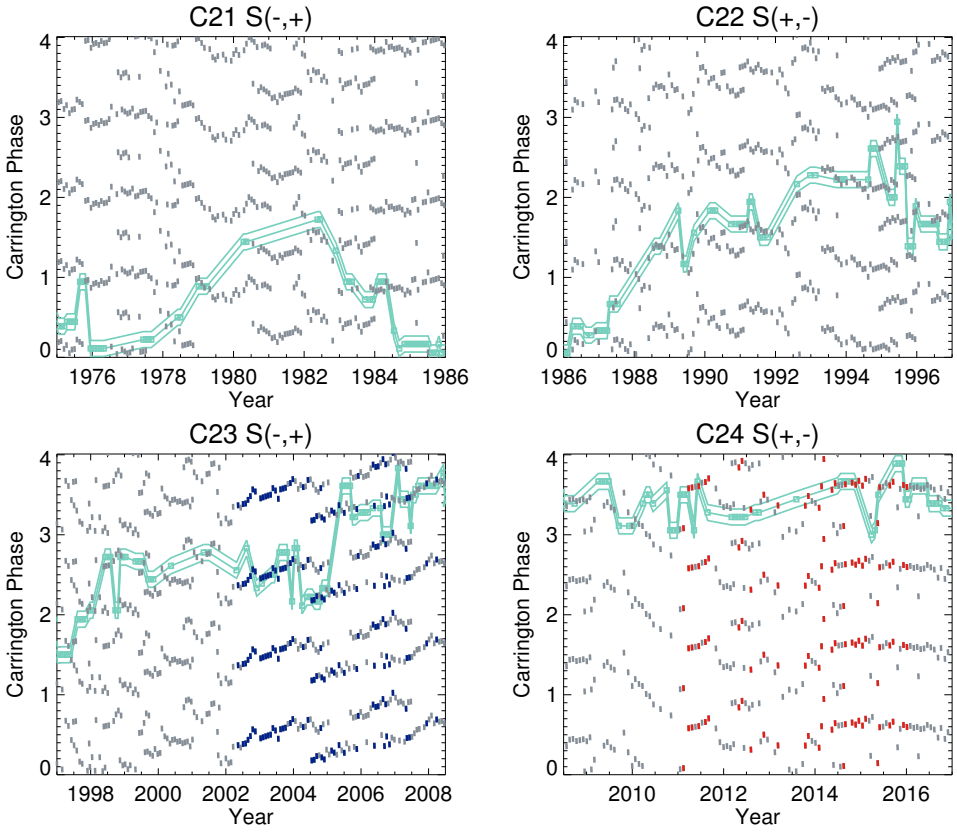

Figure 4.4: Carrington phase against year for the HSB at central meridian over Cycles 21 to 24 (top left to bottom right) in the southern hemisphere. The HSBs which had at least one RHESSI flare occuring nearby (within ±25° longitude) are coloured instead of grey, based upon the polarity change, either (+,-) red and (-,+) blue. Also shown are the observed active longitude positions (turquoise squares) with an uncertainty region of 20° adapted from Gyenge et al. (2016). Figure from Loumou, K. et al. (2018).

then decreasing (due to rotating with and then slower than the Carrington rate). On top of this we can also see the "flip-flop" behaviour (for instance, from about 2004 onwards in Fig. 4.3) where the active longitude phase is sharply jumping between two locations. These would be the locations of the two active longitude bands, but appear as a single sharp change as only the most active band in each rotation is shown.

Our HSB-Earth method is the same as in Section 4.1, giving the times the HSB was at central meridian (over a two-day range) in each hemisphere. We determine the Carrington phase of central meridian at these times to compare to the Active Longitudes. The resulting Carrington phases of the HSB-Earth are also plotted as a function of year in Figures 4.3 and 4.4, for the northern and southern hemispheres respectively. There is by no means a systematic match between the Active Longitudes and HSB-Earth but there are some periods of rather exact coincidence. This is not surprising since we expect the HSB to be associated with activity, of which the Active Longitudes are another representation. This association is not improved if we only consider the HSB that actually had RHESSI flares occur nearby (within $\pm 25^\circ$ longitude), shown as the coloured instead of grey points in Figs. 4.3 and 4.4. In particular, during Cycle 24 in the northern hemisphere there are several times with flare-associated HSB that are nowhere near the dominant active longitude (see about the vicinity of 2013 in Fig. 4.3).

The HSB drift is relative to the Carrington rate in a different manner to the migration path of the Active Longitudes. The HSBs generally show a Carrington phase that is increasing with time, showing that they are rotating faster than the Carrington rate. The phases in both hemispheres for Cycle 24 show a far flatter path (so rotating with the Carrington rate) but the Active Longitudes in the Southern hemisphere also show a flatter migration path (certainly less parabolic) for this Cycle.

The HSB phases show the expected pattern of some periods with only one HSB per hemisphere for each rotation (so two sectors overall), and others with two HSBs per hemisphere (four sectors overall). A clear example of the transition between the two and four sectors times is shown about mid-2004 (Cycle 23) in the southern hemisphere, see Fig. 4.4. It is generally during these four-sector times that we see the "flip-flop" behaviour of the Active Longitudes, jumping between

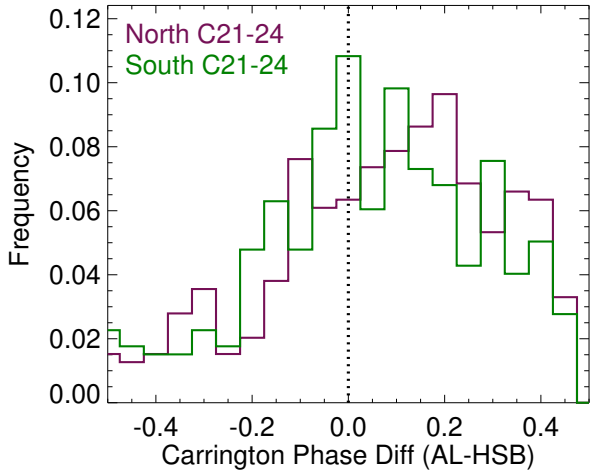

Figure 4.5: Histograms of the Carrington phase difference between the Active Longitudes and HSBs for the northern (purple) and southern (green) hemispheres. Figure from Loumou, K. et al. (2018).

the two HSB positions (such as from mid-2004 in Fig. 4.3).

This association between the Active Longitudes and HSB in Figs. 4.3 and 4.4 could be deceptive as there are numerous times in which no Active Longitudes have actually been identified. To quantify this association we could consider the Carrington phase difference between the Active Longitudes and HSB, looking for concentrated peaks. However this is difficult as only a small subset of the Active Longitudes were observed to occur within a day of the HSB being at central meridian (over the four Cycles this was 13% of the Active Longitudes in the southern hemisphere and 21% in the northern). The resulting noisy histogram of the phase difference showed no clear concentration of events, and particularly no peaks at small phase differences.

If we instead assume that the path of the Active Longitudes linearly progresses between detections, we can interpolate these observed locations onto the times at which the HSB were observed at central meridian. Note that for times in which there are two HSB present per hemisphere, we use the one with the smallest phase difference to the interpolated active longitude. The resulting histogram of the Carrington phase difference between the Active Longitudes interpolated to the HSB times is shown in Fig. 4.5. There is an association between the Active

Longitudes and HSB in the southern hemisphere, with the largest peaks at small phase differences. However things are more complicated as there are also peaks at non-zero phase differences. The association in the northern hemisphere is not as strong, and the phase difference peaks at about 0.2, suggesting that there is some association but possibly with a consistent offset. For both hemispheres there are more positive than negative phase differences, which corresponds to the HSB moving faster relative to the Carrington rotation rate than the active longitude. This is consistent with the migration paths as we have interpreted them in Figs. 4.3 and 4.4, with the Active Longitudes having periods of the phase increasing and decreasing but the HSB generally having the phase increasing. However these differences in phase could be due to one or more of the assumptions used in their determination (constant solar wind speed for the HSB, linear interpolation between the observed active longitude positions, only using the dominant active longitude position) and not indicative of a physically real link between them.

4.3 Summary and Discussion

In this Chapter, we studied the migration paths of the Hale Sector Boundaries with time, focussing on their organisation as the Solar Cycle progresses. We further contrasted them with the paths of the Active Longitudes. For the limited timeframe we created Carrington maps for, there seemed to be an association between the ascending and descending periods of the Solar Cycle with how those are mapped on the large-scale structure of the Interplanetary Magnetic Field. The two ascending phases of the solar Cycle we plotted for were associated with a more chaotic four-sector structure while the descending phase of the cycle had a more neat two-sector pattern. Echer & Svalgaard (2004) assumed that there would be a clearer HSB in the ascending phase due to the prevalence of the Rosenberg-Coleman effect, but we can see that this is not the case. Our findings were confirmed in the more thorough study on temporal variation of the HSB by Getachew et al. (2017). It is possible that the emergence of flux as we reach solar maximum cause a restructuring of the field, which is reflected on the appearance of the HSB.

The confirmation that the HSB and active longitudes do overlap sometimes is

expected, since the former has an association with activity and the latter is directly derived from activity indicators. However it is clear that they are not exactly the same thing, and show differences in migration paths; the parabolic passage of the active longitudes over time, as found by Usoskin et al. (2005); Gyenge et al. (2016) are not apparent in the HSB. The closest matching occurs when both are rotating at about, or slightly faster, than the Carrington rate, with the "flip-flop" between dominant active longitudes seen as jumping between a two-sector structure in that hemisphere (during a period of overall four-sectors). Considering the difference in Carrington phase between the active longitudes and HSB does help quantify this association, with some concentration near zero. However this varies between hemispheres and the majority of phase differences are positive, showing that the HSB Carrington phase is mostly larger than the active longitude's. This might be due to the observed migration paths, with the HSB mostly appearing to steadily increase in phase with time, whereas the active longitudes' phases increase and decrease with time. However there are several limitations and assumptions to this HSB and active longitude comparison presented in this paper that merit investigation in future studies. It is problematic that the active longitudes are not detected at all times, and linear interpolation has to be used for a full comparison to the HSB. In addition, we only considered the most dominant active longitudes, so future work could benefit from comparing the HSB to both active longitude bands. Using the HSB found from the PFSS approach could help, removing uncertainties arising from a variable solar wind speed, but this would be limited to more recent Cycles due to the availability of suitable magnetograms. Another discrepancy is that the identified active longitudes persist across several cycles while the HSB of each type swaps hemisphere as the cycle changes. As this occurs during solar minimum, it is not a major issue for the HSB-flare association, but would certainly merit further work to determine how the location of the HSB evolves as the Cycles changes, especially in comparison to the active longitudes.

The advantage of the HSB is that it can be detected at the Earth and be mapped back to activity on the Sun, providing a fast and simple approach to determine longitudinal regions of concentrated activity compared to the long term averaging and filtering required in active longitude studies. Given that the HSB can often be determined at times when the active longitude cannot be found, a

combination of both could be vital for not only helping to predict future activity but for understanding the internal source of the phenomena. It is possible to speculate as to why active regions emerge repeatedly at similar longitudinal regions (e.g. Bigazzi & Ruzmaikin 2004; Berdyugina et al. 2006; Usoskin et al. 2007), but why this should be reflected in the large-scale magnetic field through the HSB is still not clear and requires further investigation.

Chapter 5

Approaches for tracking magnetic fragments

In this part of the thesis we are staying in the realm of magnetic field changes and flare occurrence, but move from the large scale structure to much smaller scales. In the following two Chapters we will investigate two methods that allow fragment tracking in a timeseries of LoS magnetograms. We use them on data from regions that had a series of microflares in order to investigate how their magnetic field properties changed.

Separating magnetograms into smaller areas - interchangeably referred to in the literature as fragments or segments - and calculating the changes in the field together with their exact location is not new; a background on this topic can be found in Section 1.5. However, that research often focussed mainly on large flares. To the best of our knowledge, no publication addresses extensively what changes happen to the field before microflares, leading to an inability to understand their triggers and how or if they differ from flares of larger output in that respect. Castellanos Durán et al. (2018) report a C3.0 GOES class as the smallest flare with a stepwise change (Sudol & Harvey 2005) in the magnetic field. However, they note that they think this can be attributed to the selection of thresholds they chose and the resolution of the HMI data, which is the same instrument made use of in this Chapter. Therefore, we keep in mind that there is a possibility no changes will be obvious from the timelines of the bulk properties.

To perform segmentation, we make use of two distinct methods. The first

(Downhill, see section 5.1.3) was implemented by Dr. Fraser Watson during his PhD thesis, which was based on the work from Canfield & Russell (2007). The part of the pipeline regarding segmentation via downhill comes from his code, which was translated from Matlab into Python and makes use of SunPy[1] (Community et al. 2015) and the measure module of the scikit-image library[2] (van der Walt et al. 2014).

This approach appeared to return highly fragmented images. For that reason, we adopted a second approach (Watershed, see section 5.1.4) using the algorithm that was already available through the scikit-image library of SciPy. This code has an internal check that corrects for over-fragmentation as well as spurious pixels. We used both of the approaches for comparison and validation between that and downhill.

Not only do we wish to fragment individual magnetograms but we also want to be able to identify and track these fragments in time. The very first version of our time tracking code (see section 5.2.4) was a collaboration with Dr.Watson which was later expanded for the analysis presented in the following two Chapters.

Section 5.1 gives an overview of methods used to segment images and track with time the segments identified. Section 5.2 gives a detailed breakdown of the methods used to set up our experiment before starting the analysis. Finally, in section 5.3 we see this methodology been applied in a small flux emergence case and the results that this region yielded. Application on a small region allowed for testing and validation of the two methods, identifying which thresholds should be used at each stage of the pipeline and what limitations we are facing.

5.1 Overview of active region segmentation methods

Image segmentation has been a valuable process for a variety of disciplines. Consequently, there are numerous segmentation algorithms, a comprehensive summary of which can be found in Khan & Ravi (2013) and for application in solar physics in particular in DeForest et al. (2007) and Aschwanden (2010).

[1] https://sunpy.org/

[2] https://scikit-image.org/docs/dev/api/skimage.measure.html

As mentioned in DeForest et al. (2007), a characteristic of the segmentation methods developed for solar physics - and one of their limitations- is that they were created with a particular physical question in mind. As a result, they can be very project-specific. However, these differences are not as large as to not be able to use different methods on the same datasets, what it means is that they will not deliver exactly the same results. The following is a quick overview on fragmentation and tracking methods used on LoS magnetograms.

5.1.1 Previous approaches to magnetogram segmentation

CURV (Strous et al. 1996; Hagenaar et al. 1999) was a method first designed for quiet Sun Michelson Doppler Imager (MDI) data. It identifies segments by calculating the curvature of neighbouring pixels in a local maxima basis. If the curvature of a pixel with every one of its neighbours is positive, all of those pixels will constitute a segment together. This last part of the methodology is referred to in DeForest et al. (2007) as " direct clumping". It is interesting to note that the description of the algorithm from Strous et al. (1996) is very similar to the one of Watershed (see section 5.1.4).

MCAT (Parnell et al. 2009) was created to study the distribution of magnetic fluxes on the quiet Sun background during solar minimum from MDI datasets. Firstly, two different thresholds are defined, λ, which is the flux cut-off level and σ, which is the $\frac{FWHM}{2}$ of a Gaussian distribution that has been fitted to the core of the histogram created from the pixel intensity of the magnetogram. All pixels below the $\lambda - \sigma$ value are been ignored. From the pixels remaining, the ones adjacent to each other, provided they have an area of at least a minimum threshold and lived for at least a number of frames defined by the user, form a segment together.

The Southwest Automatic Identification Suite (SWAMIS) (Lamb & Deforest 2003; DeForest et al. 2007; Lamb et al. 2008) was designed to study apparent unipolar regions on MDI data. Lamb et al. (2008), after de-spiking, de-rotating, temporally averaging the dataset and determining the average noise threshold, clump pixels together if they satisfy a higher and a lower flux threshold, similar to MCAT. DeForest et al. (2007) calls that way of identifying specific segments

"downhill clumping". In SWAMIS, not only space, but time is also taken into account as a dimension. Therefore, two pixels can be adjacent either in time or space.

The Yet Another Fragmentation Tracking Algorithm (YAFTA) (Welsch & Longcope 2003) was designed to segment and track active regions on MDI data. In that case, very weak features were not of interest and a simple threshold for the magnetic flux was enough to distinguish the background. In contrast, CURV, MCAT and SWAMIS had two thresholds for the magnetic flux, a high one for lone pixels and a smaller one for pixels whose neighbours have already been assigned a label. YAFTA also follows a downhill approach, where the pixels are sorted from brightest to faintest. Reading through that sorted array, if a pixel in the $n+1$ position is a neighbour, from any direction, to the pixel in the n position, they constitute a segment together and both adopt the label the n_{th} pixel had at a previous step. Section 5.1.3 gives a more detailed explanation of how a downhill algorithm works.

Magnetic Balltracking (Potts & Diver 2008) was developed to study velocity flows but has since additionally been used to segment Photospheric fields by Attie & Innes (2015). The premise of the algorithm in the context is identifying the image as a topological surface, locate the local maxima, use them as the valleys of the surface (so effectively become the local minima). By moving from frame to frame, defined concentrations are let to drop on the gradient of the image, like balls sliding on a slope towards a basin. Concentrations that fall and meet other previously dropped are merging together and become the new local minimum. Section 5.1.4 gives a greater insight on how segmentation of an image as a topological surface works.

The variety offered leads to the question of why using an in-house algorithm instead of one of the above choices. The reasons are multitude. Firstly, it was essential to have a code that will be appropriate for microflaring regions. Secondly, heritage was a factor, as we were interesting in seeing how the algorithm previously implemented by Dr. Fraser Watson would fare on such regions. Finally, we were interested in using a code in Python in order to create a modern pipeline, taking advantage of the freely available as well as the pre-existing image processing software and the presence of a very active developer community.

The need for using a fragmentation method as opposed to readily available products such as the HMI Active Region PatsheS provided by JSOC or the Spatial Clustering Algorithm (SPoCA) active regions developed at the Royal Observatory of Belgium stems from the fact that they are offered as as a product that returns the active region as a whole entity. However, we are interested in asking which specific changes of the field lead to microflares and where exactly in the active region do they occur. Thus, it is vital to divide a magnetogram in distinguishable fragments and then track them with time.

5.1.2 Fragment time tracking approaches

There are two different methodologies of tracking the identified fragments in time, from each subsequent image. First, one can calculate the centroid of fragments and compare them between two consecutive frames, taking into account differential rotation and setting an angular distance limit (eg. Parnell 2002; Watson et al. 2009; Higgins et al. 2011). This is the approach used in this work, a detailed description of which can be found in Section 5.2.4. Another, is to study the intersections of the areas of fragments between two consecutive images. Combined with correction for differential rotation and a spatial limit of their centroids, it allows both for tracking but also starts the process for identification of merging or splitting (eg. Hagenaar et al. 1999; Welsch & Longcope 2003; Parnell et al. 2009; Anusha et al. 2017).

There have also been methods created for vector magnetograms and magnetic flows (Differential Affine Velocity Estimator, Fourier Local Correlation Tracking to name a few) that go beyond the scope of this thesis.

5.1.3 Downhill segmentation

The first segmentation method we used is an adaptation of the method detailed in Watson (2012). It follows a downhill approach, as presented in Canfield & Russell (2007) and similar to the YAFTA process of Welsch & Longcope (2003), described in paragraph 5.1.1. Downhill segments an image by identifying the peaks in its intensity profile and searching whether two of those peaks are adjacent to each other. The following breakdown explains how that process is implemented:

- Starting by reading in a two-dimensional image, it splits it in two separate ones, according to the polarity of the magnetic field. The following steps are being repeated for both polarities.

- The arrays are padded with a zero value pixel along the edge rows and columns to avoid edge effects.

- The 2D arrays are flattened to a single 1D array which is ordered from brightest to faintest unsigned magnetic flux. The location of the pixels in the original 2D array is also stored.

- Pixels corresponding to a magnetic flux less than a threshold specified by the user are set to zero.

- A 2D array the same size as the original image, with all values set to 0 is created and will be used as the *labelled map* .

- Starting with the first element in the 1D array (i.e. the brightest pixel), the location of this in the labelled map is given the value "1".

- The location of the second brightest pixel is then considered. If its location in the labelled map is one of the eight pixels neighbouring the pixel labelled "1" in the next step, then the value at this location is also set to "1". If it is not neighbouring the pixel labelled "1" then a new label value of "2" is put at this location.

- The algorithm then loops through the rest of the pixels, from brightest to faintest, and sets a value at each of their positions in the labelled map based on whether it is neighbouring a previously labelled fragment. If it is, the value is set to that previous label. Otherwise a new label is used (one larger than the previous highest label).

Overall, we are finding the peaks of intensity in each image, checking each time if the pixel identified belongs to the peak of the previous pixel or a new one. The results of this process are a negative and a positive image, separated in segments according to the pixel intensity. This way of segmentation leads to

a positive discrimination towards the brightest regions, which will be present for all images segmented with the downhill algorithm.

Note that after the final step, Watson (2012) merges any segments of the same polarity, where the smaller segment has an area of less than 6 pixels. If their pixels are neighbouring each other in a 4-connected way (so one is directly next to, on top of or under the other), they are merged as one region, to avoid over-segmentation. This is a step we did not perform as the changes to the field in microflares might be in very small scales, both in time and location. Watson (2012) used this merging approach as they were focused on the large scale behaviour of active regions producing medium to large flares.

In addition, we encountered very small regions of low intensity that ended up encircled by regions of higher brightness, getting an effect of large fragments with a small hole inside. More specifically, a pixel in the outer region that is being picked up a few pixels away from where the spurious pixel will eventually appear will be regarded as a seed pixel and start forming a segment. Then, the spurious pixel will be caught and treated as a seed pixel as it is not touching any other region pixels. They both spread until one surrounds the other. Ideally we would like the very small encircled region to become part of the bigger one. To be able to check the "noise" that these small segments are introducing we also produced the segmented labelled maps using a second approach, called watershed, detailed in paragraph 5.1.4.

5.1.4 Watershed segmentation

Watershed segmentation (Beucher & Lantuéjoul 1979)[3] works by regarding the intensity of a greyscale image as a topological surface with peaks and valleys. The image gets "filled" by the algorithm starting from the basins of the surface. The resulting segments are the contours created at the regions where the overspilling of one region meets the other. The contours themselves correspond to the gradient of a grayscale image, therefore leading to segmentation. In a marker controlled watershed, the user sets some pointers, named markers, from where they want the fragmentation to start from.

[3]See also http://www.cmm.mines-paristech.fr/~beucher/wtshed.html

We used the watershed algorithm part of the morphology module of the scikit-image library in SciPy[4].

The watershed algorithm applied to our data is implemented as:

- Starting by reading in a two-dimensional image, it splits it in two separate ones, according to the polarity of the magnetic field. The following steps are being repeated for both polarities.

- The background is set as the 0 level. The algorithm calculates the distance of each pixel from the background and identifies the position of the local maxima. The watershed is done on the $-1 * distance$ array so the peak local maxima are really the minima. These will be the markers for the watershed to start from.

- The segmentation starts from were the markers where specified, until reaching all local maxima. In the end, the contours of the resulting waterlines are the contours of each fragment.

The important feature of the watershed is that the time a pixel on the tensor of the basin is being read is being stored in memory and the pixel awaits in a queue to be allocated in a basin. This way the pixels will be allocated to the closest marker.

In addition, the developers tackled the issue of the fainter pixels encircled by brighter pixels encountered in the downhill by following the method proposed by Soille & Ansoult (1990). The spurious pixels are expected at regions where the gradient is smaller and the surfaces plateau. For those regions, a pixel will be assigned to the neighbour that has the largest gradient. In the case the gradient is equal to zero, those pixels will be split and shared between two opposite markers.

[4] https://scikit-image.org/docs/0.13.x/api/skimage.morphology.html?highlight=watershed#skimage.morphology.watershed

5.2 Methodology

5.2.1 HMI data preparation

5.2.1.1 Choosing the appropriate area to study

Our general procedure starts by us selecting a subregion of the full HMI map that was large enough to cover the whole extent of the active region of interest. This was then rotated to a reference time - usually the first time in a sequence of HMI maps - to follow the differential rotation of the Sun, according to $\omega = A + B\sin^2\varphi + C\sin^4\varphi$, where the rotation coefficients are A = 2.894±0.011, B = -0.428±0.070 and C = -0.370±0.077 in $\mu rads^{-1}$ and φ is the latitude of each pixel (Howard et al. 1990). As a result, the width of the submap changes as the Sun rotates; for example for a region first observed at the Eastern part of the Sun, the map will appear wider as the region approaches Sun-centre and will shorten as it moves to the West. An example of the resulting submap can be seen in Figure 5.1, when we present our testing region in section 5.3.

To determine the appropriate size of the submaps, we created a number of them for a variety of times and contrasted them with images from Helioviewer[5], to ensure we did not miss any of the magnetic field as the time progressed.

Welsch et al. (2011) when studying field changes for the Whole Heliospheric Interval applied a cosine correction to the B_{LOS}. However, Petrie & Sudol (2010) showed that the field from the photosphere that exhibits flaring activity, is mainly horizontal -although for their work they were studying larger flares and not microflares. That, in addition with the fact that we are studying smaller timescales, from a few hours to 3 days maximum, led to the decision to not proceed with that correction. As will be shown in Chapter 6 this was not the correct decision and a cos correction should be applied in the future. Petrie & Sudol (2010) performed a study over 4 hours, which did not allow for geometrical effects to have an effect in their results.

The final submaps, for all times, were then saved out as .fits files.

[5] https://helioviewer.org/

5.2.1.2 Choosing the line-of-sight magnetic field threshold

We need to determine an appropriate absolute B_{LOS} threshold so that we only find fragments of significant magnetic flux and can exclude background noise. Any pixel with a flux below that limit will be disregarded. We overlaid contours of the submaps according to the pixel intensity. The threshold was decided to be the value of the magnetic field that excluded noisy background, without losing information on the regions that were flare related. Figure 5.3, bottom panel, shows an example of a test region we used and contours for pixels of $|50G|$ or $|100G|$. Those contoured plots were repeated for the times we had flares and we checked whether the fragments around the flaring locations had survived the threshold. For the test region we determined a threshold of $|50G|$ to be appropriate.

As a way to see how the threshold fits in the frequency of the values of the image field recorded, we created histograms of the magnetic field of the submaps. For the test region in the next section, the histograms in the first four panels of Figure 5.3 (histograms of full submaps on the left and a close up to the core on the right) indicate that a limit of $|50G|$ indeed does not omit any changes of the field.

Creating a histogram of the map and choosing the threshold as a standard deviation of the histogram is a typical way for its determination. Burtseva & Petrie (2013) used a 1.3σ standard deviation to decide the threshold on the core of GONG magnetograms and Parnell et al. (2009) applied a 2σ standard deviation threshold on MDI magnetograms as a start and 3σ after tracking segments with time. DeForest et al. (2007) suggested a threshold of 3σ for MDI and GONG magnetograms.

5.2.2 Segmentation algorithms

We load in the submaps from the previous step and start the segmentation processes described in Section 5.1, for the pixels satisfying the B_{LOS} threshold. The output of both algorithms is a labelled map, that is a numpy integer array where every pixel belonging to a segment has been assigned a label (positive integer). Pixels below the flux threshold are not part of the resulting fragments and so have a value of 0. The labelled maps are then saved out before the properties of the

Table 5.1: Fragment properties determined from scikit-image measure regionprops. In the thesis, the output of the first four properties are being presented.

Property	Units
Centroid position	deg and pixels
Weighted centroid position	deg and pixels
Area of segment	cm^2 and pixels
Magnetic flux	Mx and Gauss
Location of corners if bounding box surrounding the segment	deg
Area of bounding box	px
Centroid coordinate with respect to the bounding box	deg
Eccentricity of an ellipse fitted on the segment	-
Major axis of an ellipse fitted on the segment	-
Minor axis of an ellipse fitted on the segment	-
Orientation angle: angle between the 0th row of the segment and the major axis of the ellipse	rad

fragments are determined (see Section 5.2.3).

Figure 5.2 shows an example of identified fragments using the downhill and watershed approaches. As expected, the downhill approach segments the regions into more fragments. As previously mentioned, we have not implemented the additional step of merging 4 or 8-connected neighbouring regions of small areas as a final step of the downhill approach. This would likely have resulted in the output of downhill and watershed being even more similar.

5.2.3 Determination of Fragment Properties

We make use of the regionprops algorithm from the scikit-image library of SciPy [6], whose function is to take a labelled integer array as input and calculate a number of physical properties for each labelled region. Regionprops has the ability to return 38 properties, a selection of which we saved out in text files for our analysis. Table

[6] https://scikit-image.org/docs/dev/api/skimage.measure.html#skimage.measure.regionprops

Table 5.2: Bulk properties of the whole region saved out.

Property	Units
Date	-
Number of fragments	-
Total area	px
Total magnetic flux	Mx

5.1 details the properties saved out, a portion of which we used later in Section 5.3 for a test region, and then for three more active regions in Chapter 6. The spatial properties are returned in terms of pixel location in the differentially rotated HMI submaps. So, for some of the properties we convert these positions into degrees in the Heliographic Stonyhurst Coordinates, via the SunPy tools, i.e the fragment centroid is given in submap pixel x,y and also Stonyhurst longitude and latitude.

For every image, some of the properties are additionally summed up and saved out in a separate file as bulk properties of the whole active region, Table 5.2 . The bulk properties allow for tracking changes in the whole region before and after flaring. Our analysis is mainly based on these, as time did not allow to make more use of the fragment properties themselves.

5.2.4 Time-tracking of fragments

After segmentation has been completed, one wants to track the segments with time. To determine which segment propagated from one frame to the next, we developed an algorithm that uses their centroid position to track their movement from frame to frame.

The time tracking is performed using the following steps:

1. Properties of all fragments of the first image are loaded.
2. Before proceeding we can optionally apply an area restriction, filtering out any fragments that are too small.
3. The properties of all fragments are stored and assigned a new label (“0”, “1”, “2”, ...). These labels will be consistent over time and different from those of

individual frames discussed in Section 5.2.2. The properties found to be associated to a label will be stored next to it.

4. The current time and centroid locations of the fragments are temporarily stored as the "old" properties.

5. The properties of the fragments from the next image in the time series are loaded and temporarily stored as the "new" properties.

6. The "new" fragment centroid longitudes and latitudes (in Heliographic coordinates) are differentially rotated back to the time of the previous image. Then the euclidean distance is calculated between all the"old" and differentially rotated "new" fragment centroids. We keep track of which distance relates to which pair of fragments in the "old" and "new" images.

7. The distances are sorted from smallest to largest. This sorted order is also applied to the index describing which old and new fragment each distance refers to.

8. Any distance exceeding our chosen distance limit is disregarded.

9. Starting from the shortest distance, the associated old and new fragments are identified. The properties of the identified new fragment are stored alongside the properties of the old fragment, in the structure from step 3, next to the label of the old fragment.

10. In our distance list, we can now remove all distances between the assigned old or new fragment and with any other fragments.

11. Steps 9-10 are repeated, starting with the next smallest distance on our list. This process repeats until all the distances have been assigned or deleted. After this stage has been completed there could still be fragments left on the "new" list and so they are given a new label (+1 numerically from the last label assigned).

12. We additionally keep track of how many newly appeared fragments we get per image and save out their bulk properties in a separate structure, for each frame.

13. Similarly, if, all entries in the list "new" have been erased, but there are still entries left in "old", these are fragments that did not propagate to the next frame. We keep track of how many non-propagated fragments we end up with per image and save out their bulk properties in a separate structure, for each frame.

14. All three structures (properties of time tracked fragments, bulk properties of new fragments, bulk properties of non-propagated fragments) created are being saved out.

Fragments are allowed to move up to 0.05^o (in Heliographic Stonyhurst coordinates) for 45 seconds cadence data and up to 0.15^o for data of 720s resolution. The angular distance limit was decided by looking at movies depicting the centroids of fragments across the whole timeline studied. We estimated what was the largest displacement of a centroid, as far as we could see, and calculated to how many degrees that corresponds to. We tried a variety of limits, ran the time-tracking code and created movies of the output. We settled for the limits that seemed to allow fragments to propagate from frame to frame without mis-identifying fragments with neighbouring regions. In addition, the appropriate limit should allow a fragment to move from frame to frame, without being re-labelled only because it shifted further than it was permitted to. Thirdly, a generous limit increases the probability of a fragment being wrongly thought as having existed in more frames that it actually did. However, a distance limit that is higher than the correct value would have had a smaller impact on the output compared to a distance limit that is smaller than the correct value. This is down to step 9 in the description of the code above, since the segments are being tracked based on the shortest distance calculated. Calculating more distances than needed does make the pipeline slower, but frequently it has no additional effect. Any further distances calculated for a fragment that has been tracked, are deleted in step 10. We believe we chose the appropriate limit to satisfy these criteria. By watching the movies, we could also see large fragments merging with smaller ones. The label of the larger fragments persisted while the label of what was the smaller fragment would vanish after merging, as it should. A more refined approach would be to track those distances with time and correct the angular distance limit as the region moves across the

disk. However, in this work we have chosen a limit that works for a range of longitude positions across the solar disk.

The newly labelled fragments from step 12 can be the product of emergence, merging, splitting, or they were present as a fragment a few images back, then fell below the B_{LOS} threshold for at least one frame and rose above it in the current image. The pipeline has no additional check for this event currently. A way to tackle this would be to identify all new fragments, and re-run 3-4 of the previous frames for the frame they first appeared to see if they existed in the position they should occupy after de-rotation. However, that would be computationally expensive. Another way is to add a lifetime criterion. For example, Welsch et al. (2011) apply a criterion that a fragment is taken into account if it has lived in at least 4 frames. DeForest et al. (2007) advise that such a move additionally acts as a precaution again spiking from cosmic rays. However, microflares might be the result of only small disturbances and such a criterion increases the timescale of the changes we see. Therefore, a lifetime threshold does not seem appropriate for this research.

The non-propagated fragments of step 13 have either merged, split, fell below the B_{LOS} threshold or cancelled out.

5.3 Algorithm implementation and testing

For the testing of the two fragmentation methods we used a small scale flux emergence region, classified by the Spatial Possibilistic Clustering Algorithm (SPoCA) suite (Verbeeck et al. 2014) as region SPoCA 21717. It was a distinct bipolar small region, chosen for its small size and production of a small microflare with a simple loop structure. The region first appeared on 9th of April 2018, at 05:30:00 UTC and formed clearly at 06:30:00 UTC, which is the time the analysis of the region began. Figure 5.1 shows the region in four different instances, with the first and last frame showing the start and end time of the analysis. The third frame of the image has the location of the flare overlaid, as reported in the HEK catalogue. RHESSI did not record the flare, so we could not overplot the RHESSI image.

SPoCA 21717 produced an A2.5 GOES class flare, with start time at 12:30:00

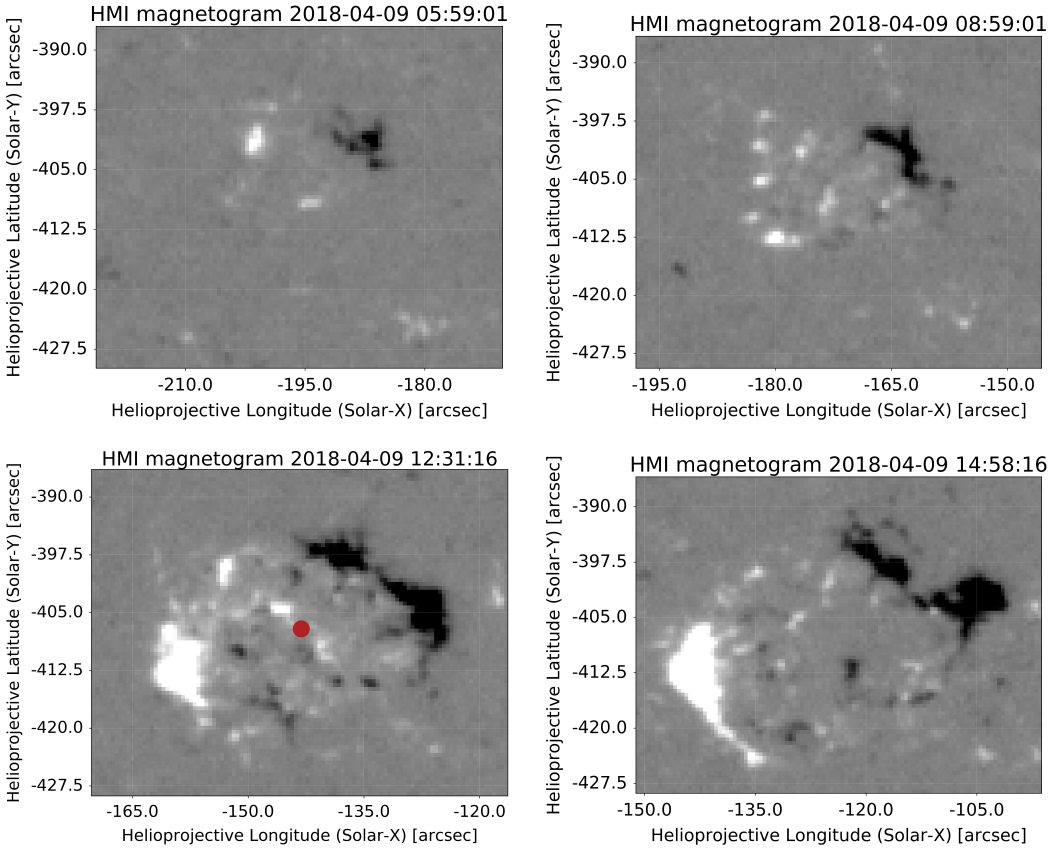

Figure 5.1: Frames of the submaps studied for region SPoCA21717, starting from the beginning of the observation until the end. The red dot on magnetogram 12:31:16 indicates the position of the A2.5 flare, as given in the HEK catalogue.

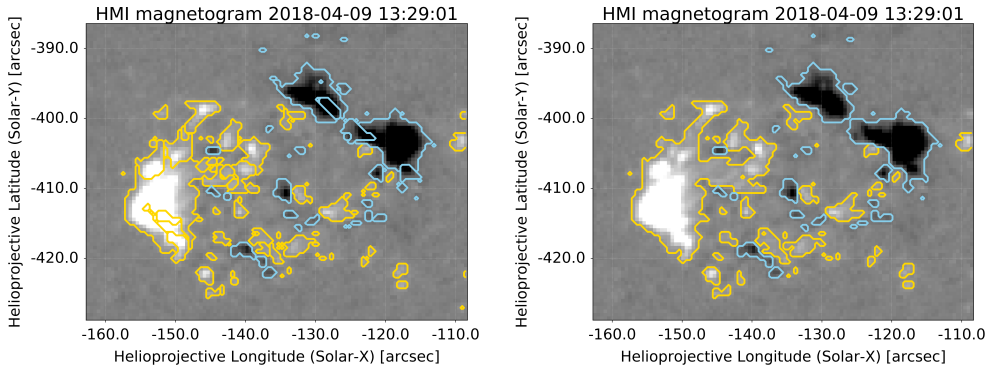

Figure 5.2: Fragmentation of HMI LOS magnetograms of SPoCA21717 test region produced by the downhill (left) and watershed (right) algorithms. Downhill returned 73 positive segments and 40 negative segments for this instance. In contrast, the watershed returned 37 positive and 27 negative respectively. A $|50G|$ threshold has been applied.

UTC and end time 13:41:00 UTC on the same day. The analysis of the region was extended no further than 14:59:00 UTC, as the primary motivation was to establish that the fragmentation process is robust and provides reliable results. The next goal was to study what happens to the field before the microflare.

5.3.1 Output of choosing line-of-sight magnetic field threshold

Following the procedure detailed in section 5.2, after the size of the submaps was defined, they were then processed to determine the B_{LOS} threshold, see Section 5.2.1. Figure 5.3, bottom panel, shows the contours of pixels of at least $|50G|$ in lilac and $|100G|$ in purple. Repeating those maps for a number of times during which the flare was taking place, it was clear that a $|100G|$ threshold was not allowing fragments around the location of the flare to appear. As a result, the $|50G|$ lower limit was thought to both include interesting magnetic features and exclude background noise. Figure 5.3, top four panels, indicate where the $|50G|$ and $|100G|$ thresholds are placed in a histogram of the magnetic field of the submaps, for a time where the region had small (05:59:01 UT) and larger emergence (11:59:01 UT).

Since this was a test region, all results are presented, including the ones corresponding to the $|100G|$ threshold.

5.3.2 Time profiles of field changes

We applied the approach described in Section 5.2 to identify and time track the magnetic fragments, as well as calculate the properties. We used two separate algorithms for fragment identification (downhill and watershed). In this Section we are concentrating on testing the stability and behaviour of each approach primarily and secondarily, see the effect of the microflare on the bulk properties of the region.

Figures 5.4 - 5.13 present the time profile of the total surface fragment area, the unsigned flux, the average area and average unsigned flux per fragment as well as the average unsigned flux per area, as returned from each fragmentation method. Figures 5.14 - 5.17 show the number of fragments and the number of

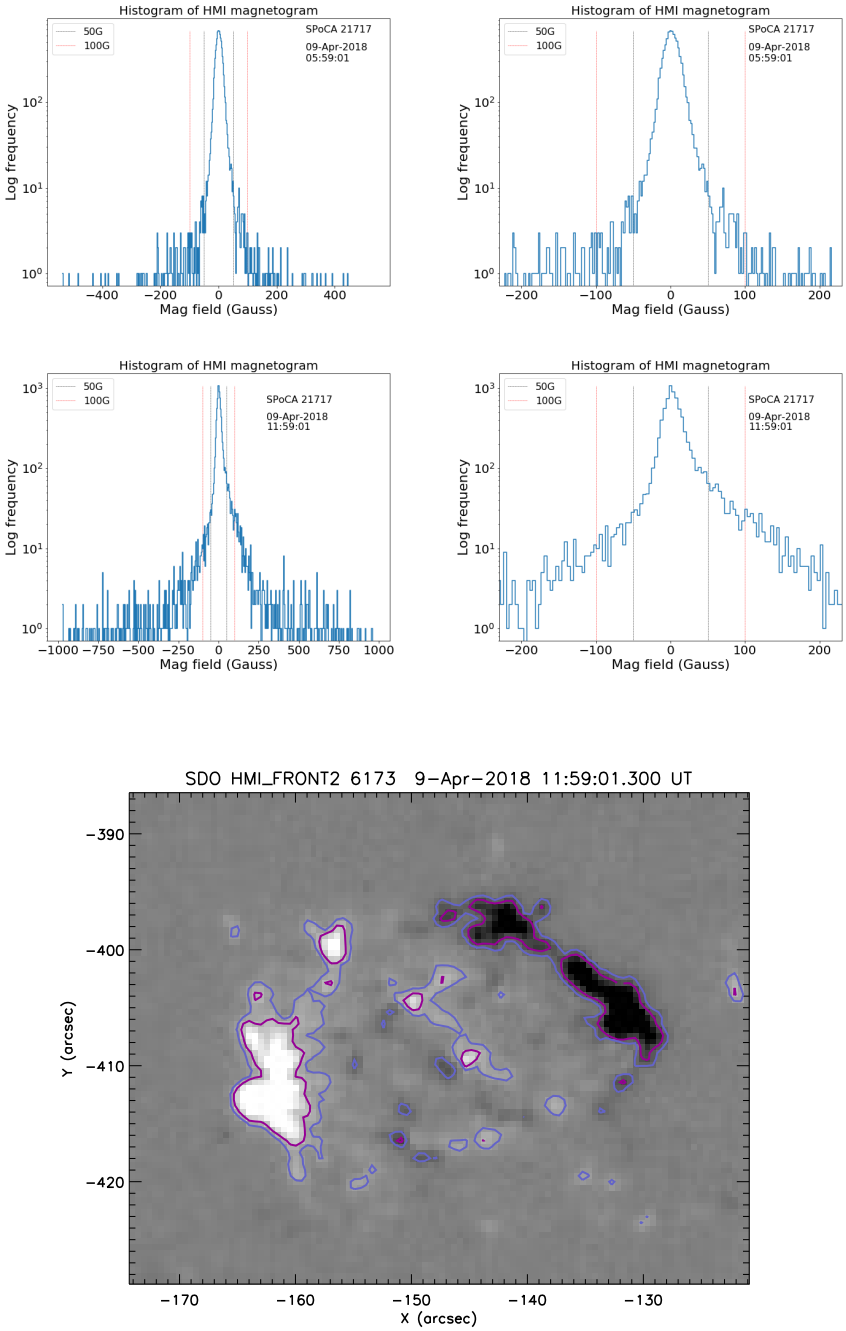

Figure 5.3: Top four panels, left: Histograms of the line of sight magnetic field for HMI magnetograms of active region SPoCA 21717. First four panels, right: A close-up around 0 of the histograms on the left. Bottom panel: Submap of the SPoCA region, for the time of the histograms on the second row. With lilac contours of all magnetic field of at least $|50G|$. With light purple contours of all magnetic field of at least $|100G|$.

new fragments registered, for all fragmentation methods and B_{LOS} thresholds. The blue vertical dashed line indicates the start time of the flare observed and the black solid line the flare end time, allowing to look for changes before, during and after the flare occurred.

The plots are given for a variety of fragment surface area thresholds. This was done as a way to determine how a restriction on the fragment area affected our plots and what would be a good limit. The plots show that such a threshold has no significant impact on the bulk properties. Therefore, they are not a strong indicator of what the smallest area threshold should be, leaving visual inspection of the movies created as the main way of determining this parameter, if it is to be applied.

The reason behind the consistently higher values of positive fragments compared to the negative can be attributed to the fact that there was an imbalance in the field of the region, between positive and negative. Looking at the timeline of the submaps of the region, there is the impression of more positive field arising. Since there was no other region nearby, the negative field must have been spread widely and looked as part of the quiet Sun and possibly was below the B_{LOS} threshold. In fact, Lamb et al. (2013) and DeForest et al. (2007) warn about the effect this illusion can have on the resulting plots.

All plots generally behave as expected. With no area restriction applied, the two methods should give identical results for the total unsigned flux, total fragment area, and unsigned flux per area. We see this to be the case as well as the expected behaviour that as we increase the area restriction (filtering out the smallest fragments) this effects the downhill method more than the watershed. This is because the watershed should generally segment into larger fragments, as confirmed in the average area plots.

In Figures 5.4-5.5 we see that the fragment area has a steady increase with time, particularly for the positive fragments. This reverses after the start of the flare and then again after the end time. This behaviour fits into the context of a region where reconnection is happening, so fragments of opposite polarities are cancelling out. It also indicates that the flaring process slows down or halts merging. A change in flux or area is also considered an indication of a flux tube tilting (Spirock et al. 2002; Wang et al. 2002). In the large statistical study by

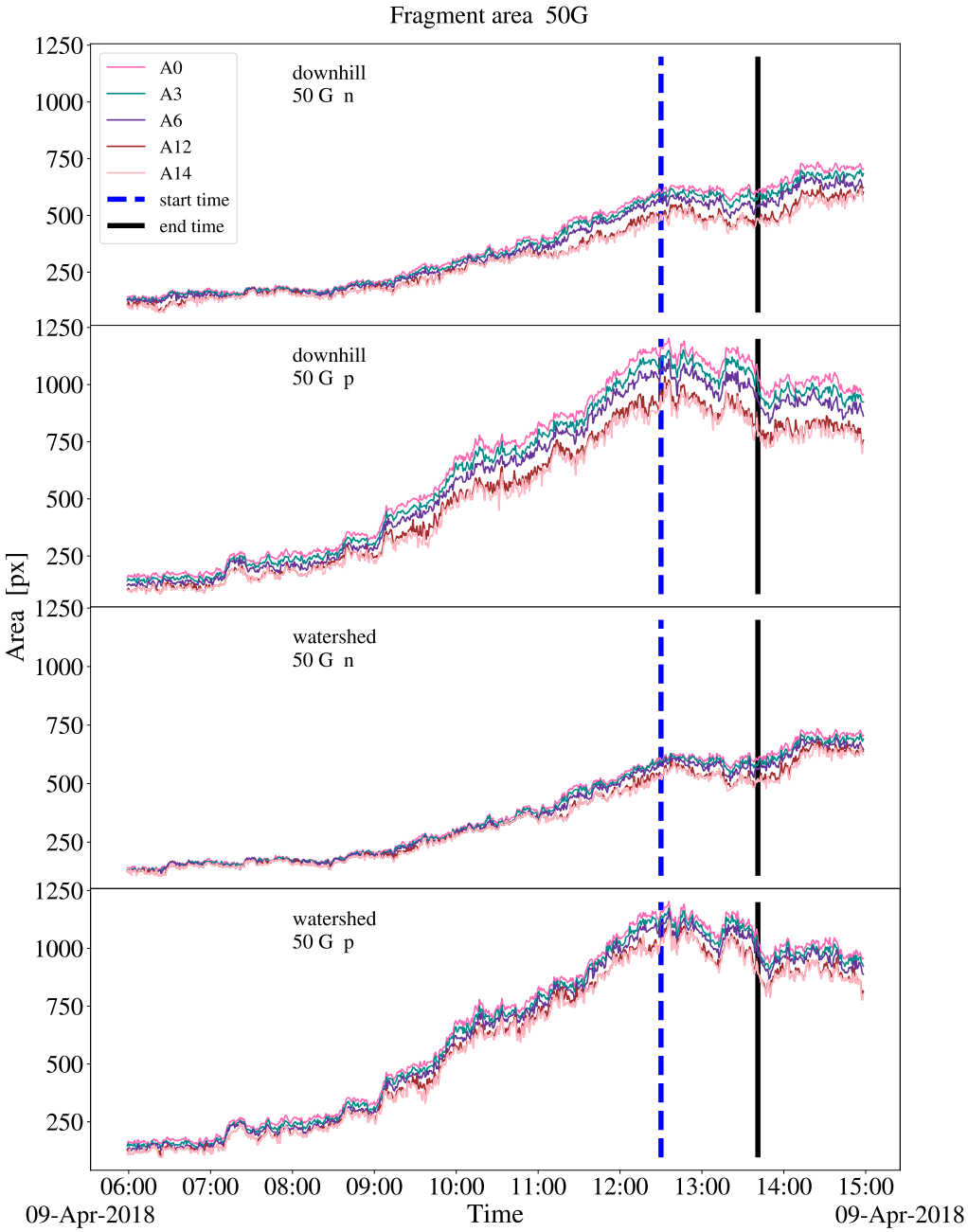

Figure 5.4: Timeseries of the total area from all fragments for region SPoCA21717, using downhill fragmentation (top two panels) and watershed fragmentation method (bottom two panels). Rows alternate from negative (n) to positive (p) polarities. A magnetic field threshold of 50G was applied. The different coloured solid lines indicate the fragment area threshold. The blue vertical dashed line indicates the start time and the solid black the end time of the A2.5 GOES class flare.

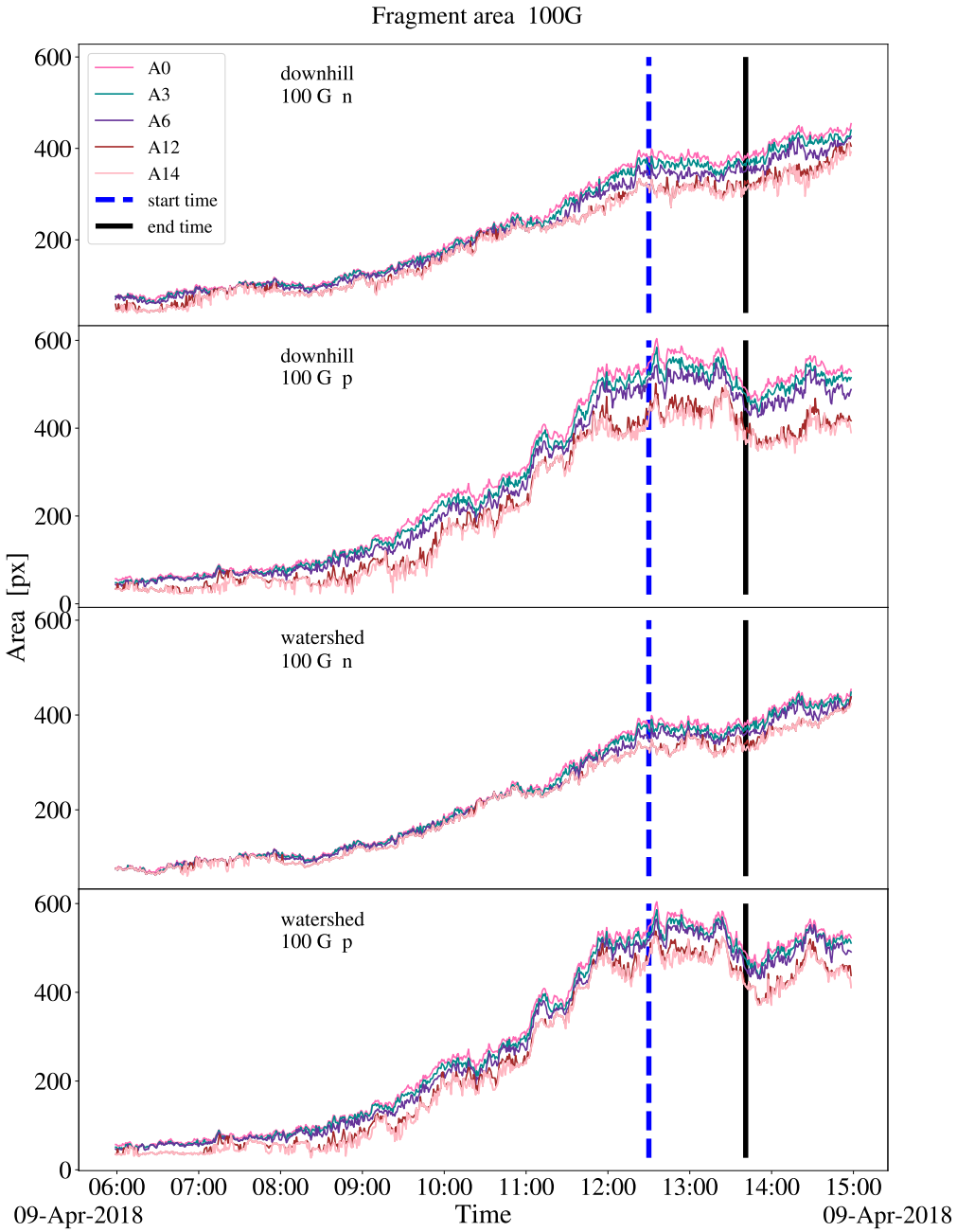

Figure 5.5: As in Figure 5.4, but with a magnetic field threshold of 100G.

Castellanos Durán et al. (2018) this was not re-confirmed.

Figures 5.6-5.7 show that the sum of the unsigned flux is also has a steady increase with time. For the curve of the watershed fragmentation there are three small dips in the profile after the start, about the peak and end flare time. The flare did not seem to cause significant disturbance in the field. If the increase in flux is considered emergence, it has not been halted throughout the flaring process.

As we can see in Figures 5.8-5.9 - although the plots from watershed become more difficult to judge due to the smaller number of fragments - the average area generally seems to be unaffected by the flare. The same applies for the average unsigned flux, Figures 5.10-5.11.

In Figures 5.12-5.13 the peaks in the plots at times around 08:30 UT, 09:00 UT and 11:00 UT have been caused from the merging of positive fragments of large areas, causing the fraction of mean flux per area to increase. As a note, at the location of the flare, the fragments split in both fragmentation methods.

For the test region we studied in this section, both fragmentation methods have yielded similar results, as expected. The plots of most of the bulk properties (the exception being the number of fragments and properties that are a product of them) should be the same no matter the fragmentation method chosen, as long as there is no area restriction, since they are the summation of a property of the magnetogram above the chosen threshold.

The different area limits have not made a significant impact on the plots. After visually inspecting the fragments for a number of cases, a least area limit of 12 pixels seems to be the largest limit before significant number of fragments were not being identified at all. This does not seem to have a specific physical meaning.

As a next step, we focus on the time profiles of the new fragments appearing. Figures 5.14 to 5.17 present the time profiles of all fragments, paired with the profiles of the new fragments, for the same area and threshold restrictions.

The number of new fragments in this particular region did not give an indication for the flare that took place on 12:30:00 UTC. There is however a clear increase in the number of new fragments throughout the time range considered. This makes sense as this is an emerging region which spreads out and further fragments with time. Of course from our code a newly labelled fragment could be

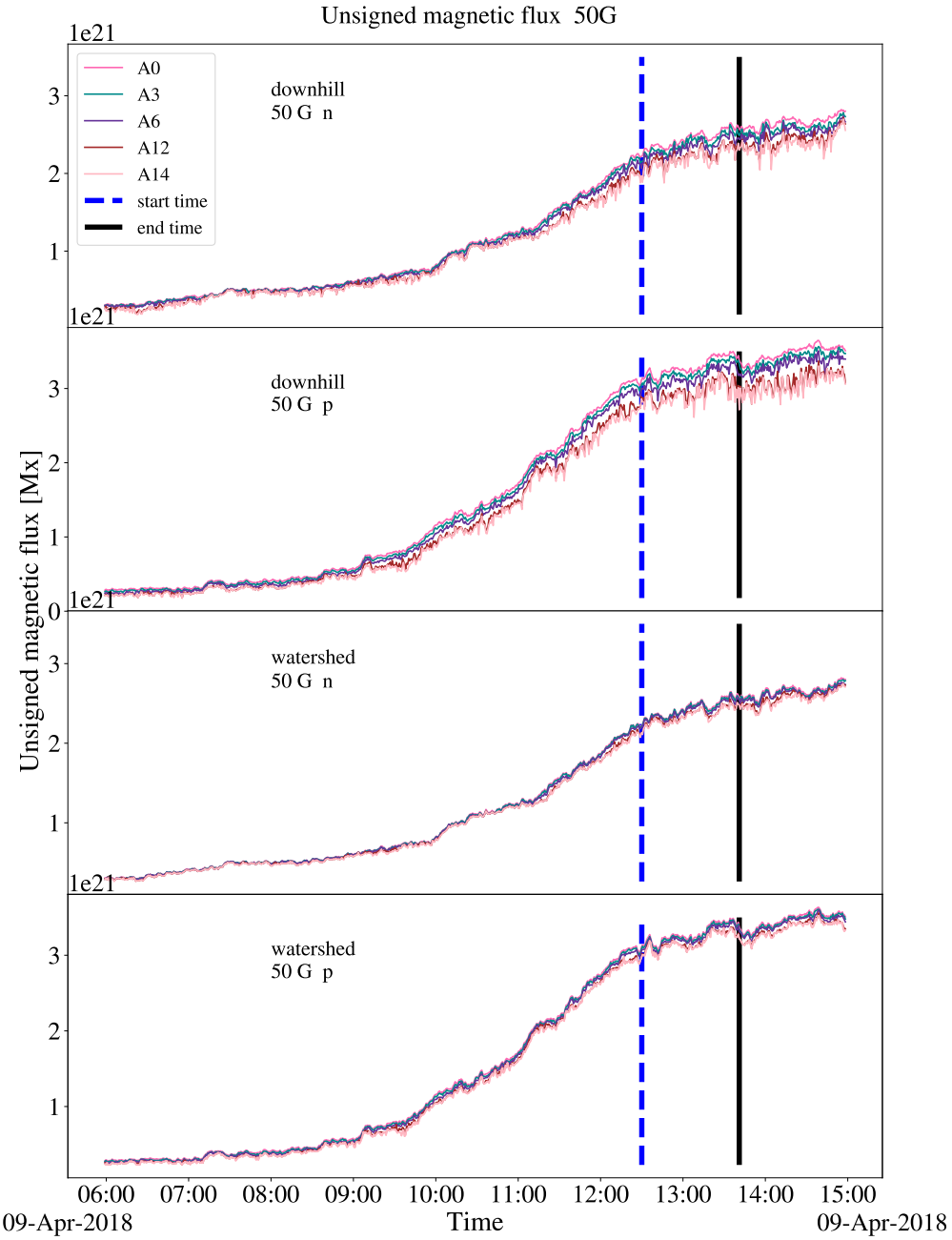

Figure 5.6: Timeseries of the total unsigned flux from all fragments for region SPoCA21717, using downhill fragmentation (top two panels) and watershed fragmentation method (bottom two panels). Rows alternate from negative (n) to positive (p) polarities. A magnetic field threshold of $50G$ was applied. The different coloured solid lines indicate the fragment area threshold. The blue vertical dashed line indicates the start time and the solid black the end time of the A2.5 GOES class flare.

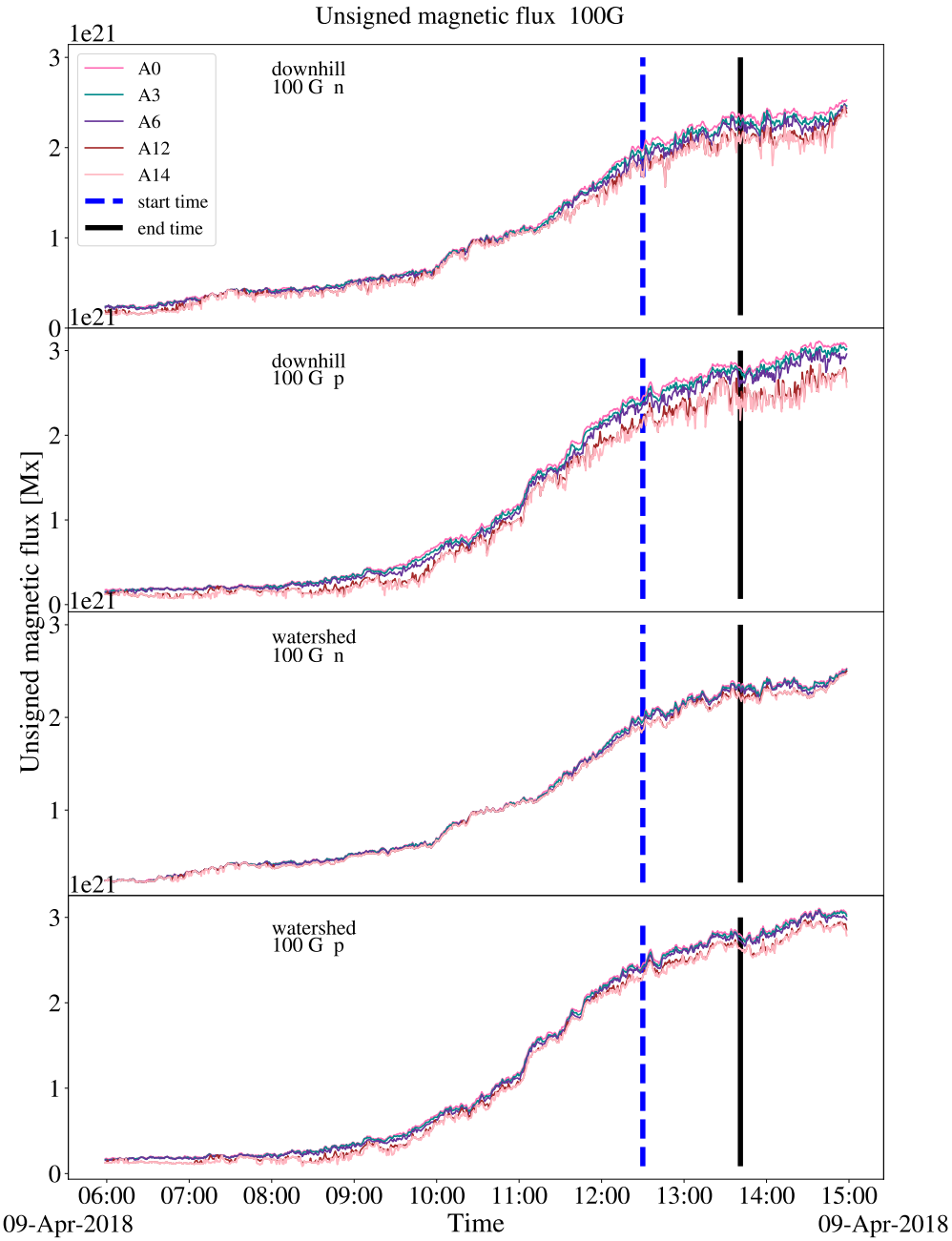

Figure 5.7: As in Figure 5.6, but with a magnetic field threshold of $100G$.

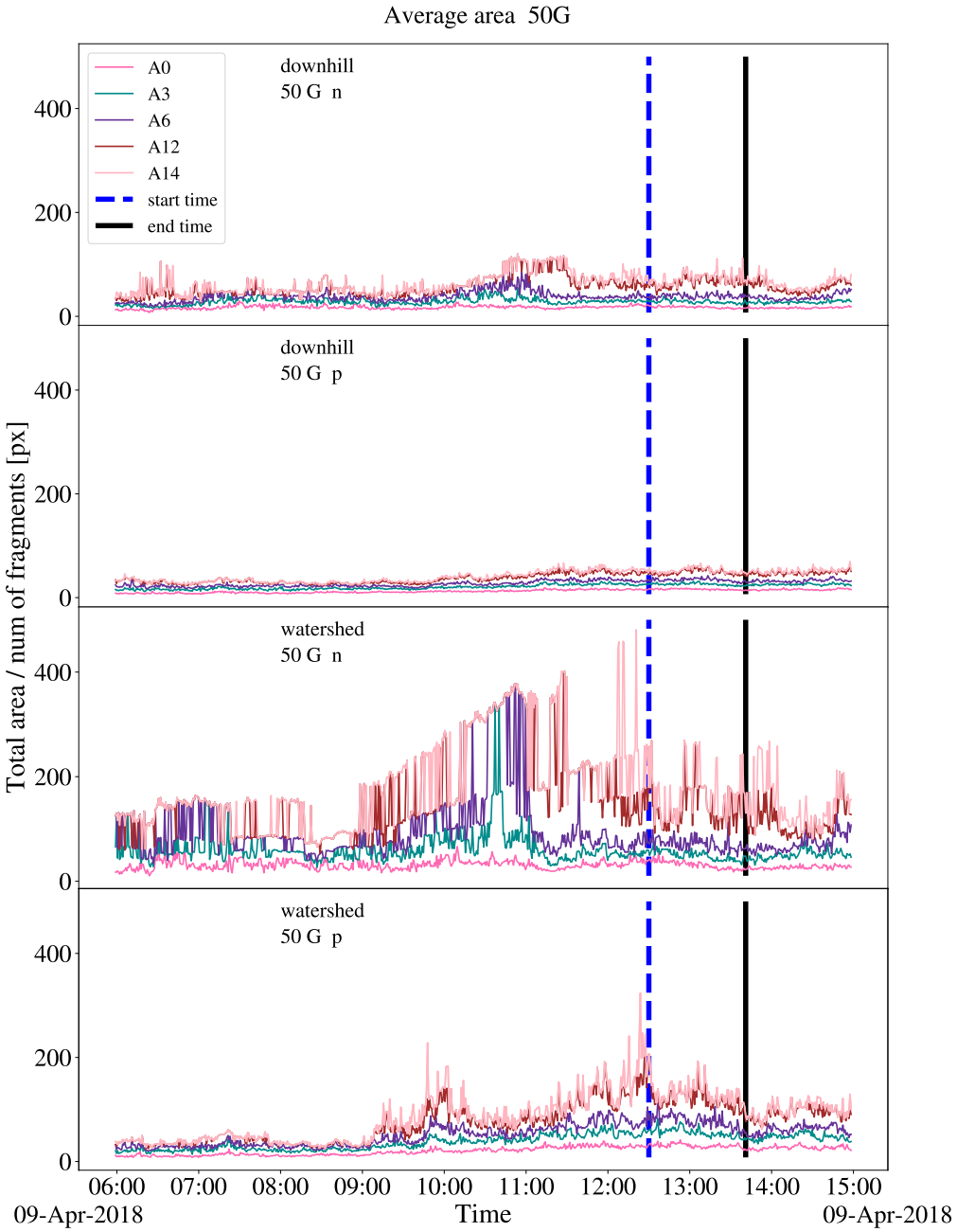

Figure 5.8: Timeseries of the average area per fragment for region SPoCA21717, using downhill fragmentation (top two panels) and watershed fragmentation method (bottom two panels). Rows alternate from negative (n) to positive (p). A magnetic field threshold of 50G was applied. The different coloured solid lines indicate the fragment area threshold. The blue vertical dashed line indicates the start time and the solid black the end time of the A2.5 GOES class flare.

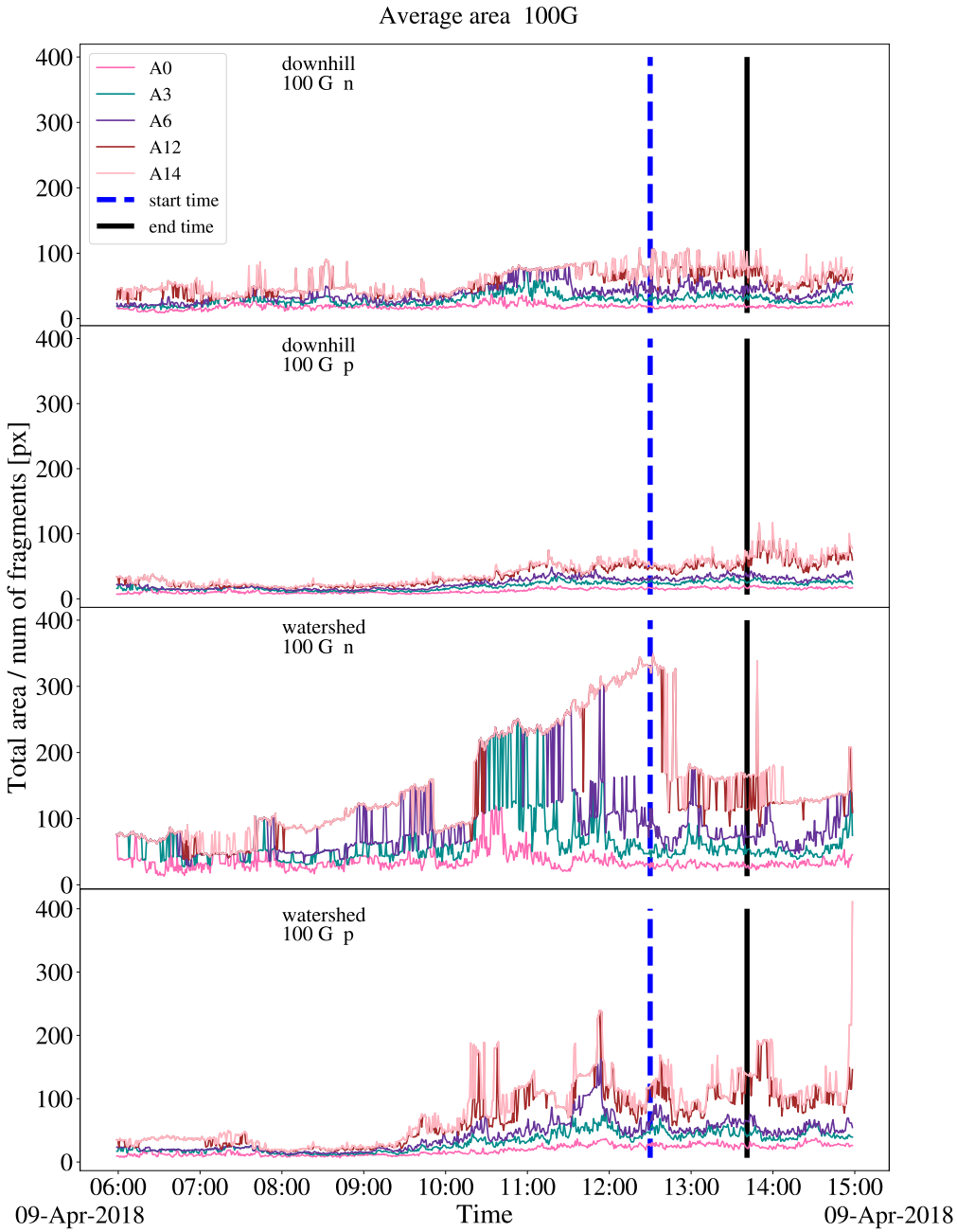

Figure 5.9: As in Figure 5.8, but with a magnetic field threshold of $100G$.

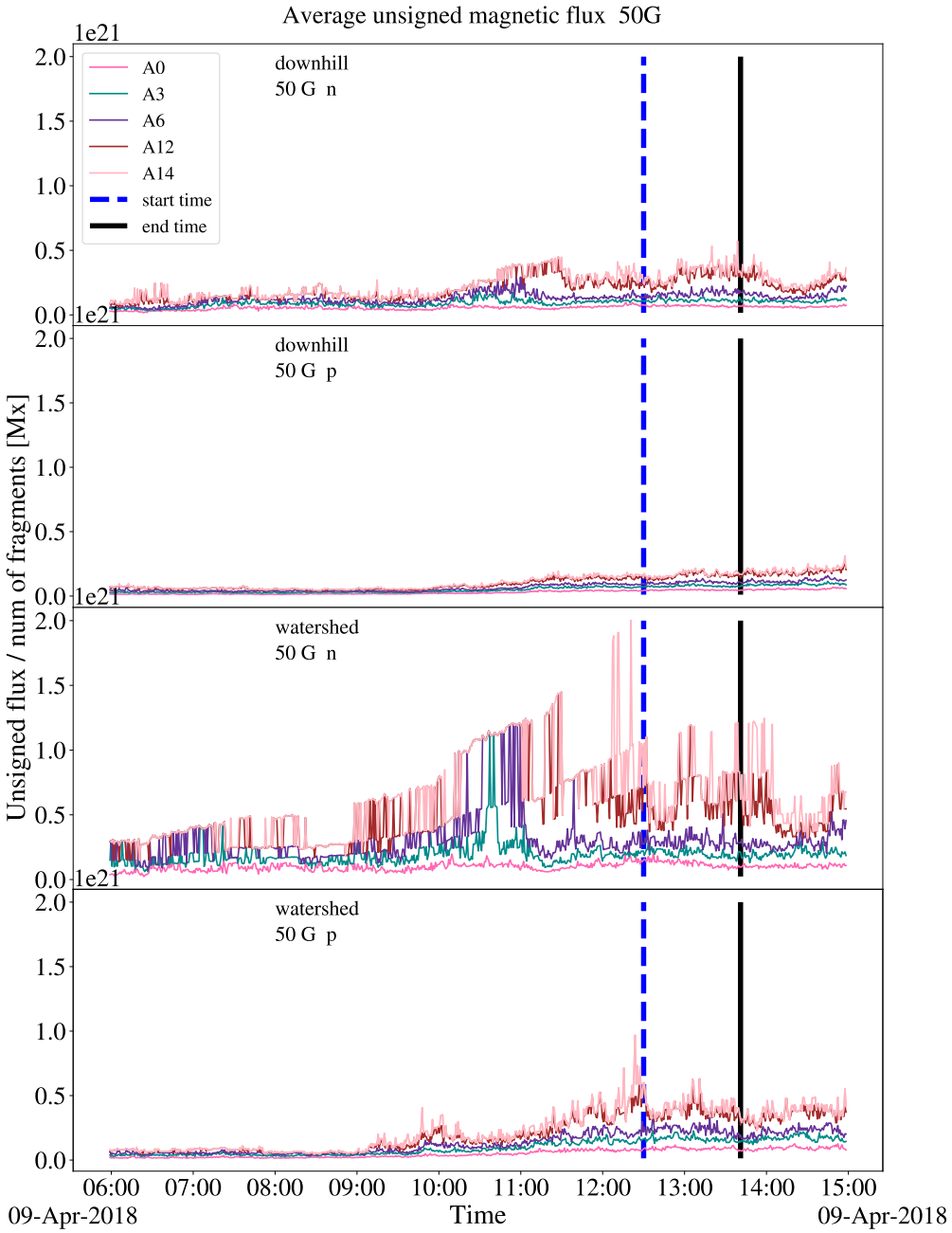

Figure 5.10: Timeseries of the average unsigned flux per fragment for region SPoCA21717, using downhill fragmentation (top two panels) and watershed fragmentation method (bottom two panels). Rows alternate from negative (n) to positive (p). A magnetic field threshold of 50G was applied. The different coloured solid lines indicate the fragment area threshold. The blue vertical dashed line indicates the start time and the solid black the end time of the A2.5 GOES class flare.

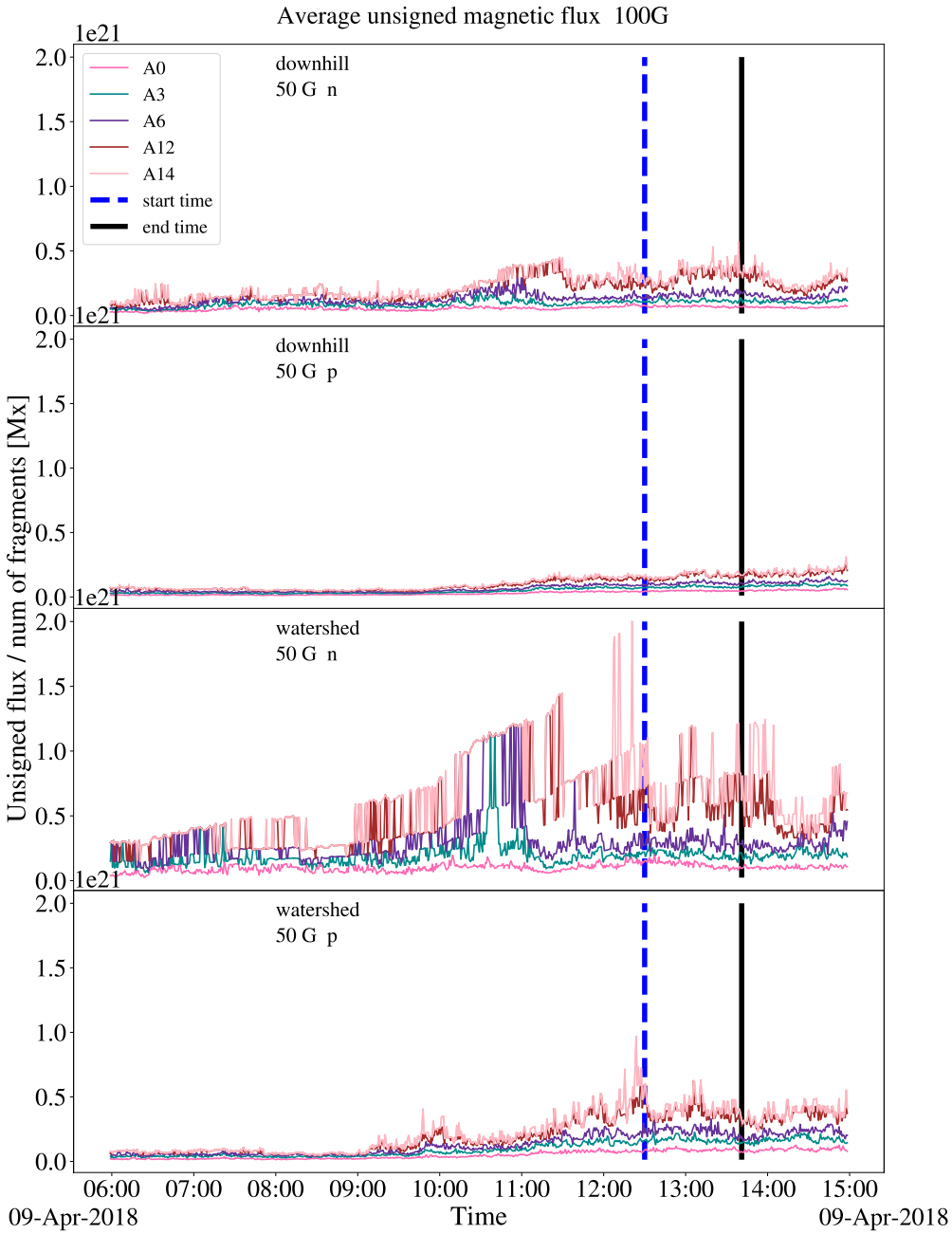

Figure 5.11: As in Figure 5.10, but with a magnetic field threshold of $100G$.

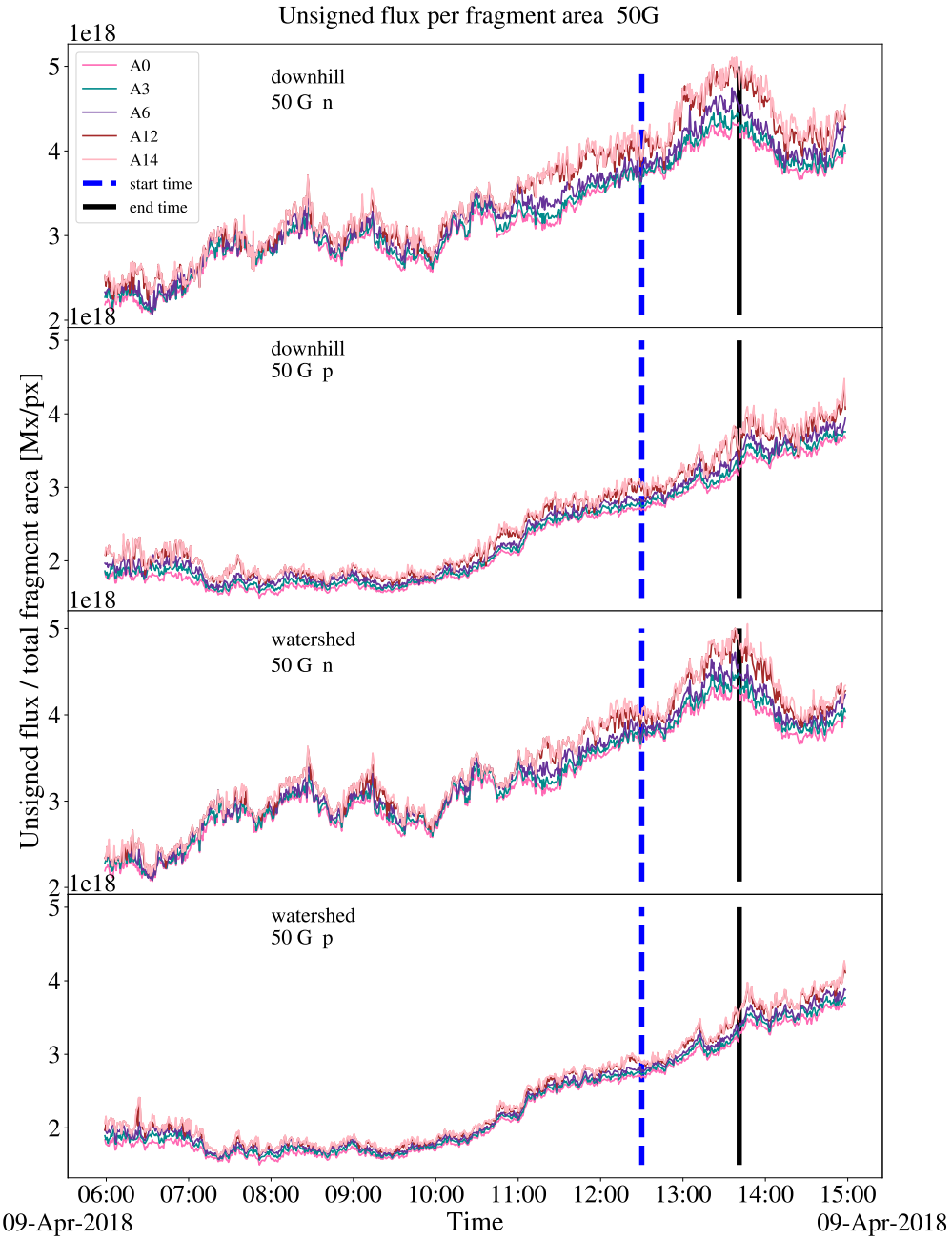

Figure 5.12: Timeseries of the average flux per fragment area for region SPoCA21717 using downhill fragmentation (top two panels) and watershed fragmentation method (bottom two panels). Rows alternate from negative (n) to positive (p). A magnetic field threshold of 50G was applied. The different coloured solid lines indicate the fragment area threshold. The blue vertical dashed line indicates the start time and the solid black the end time of the A2.5 GOES class flare.

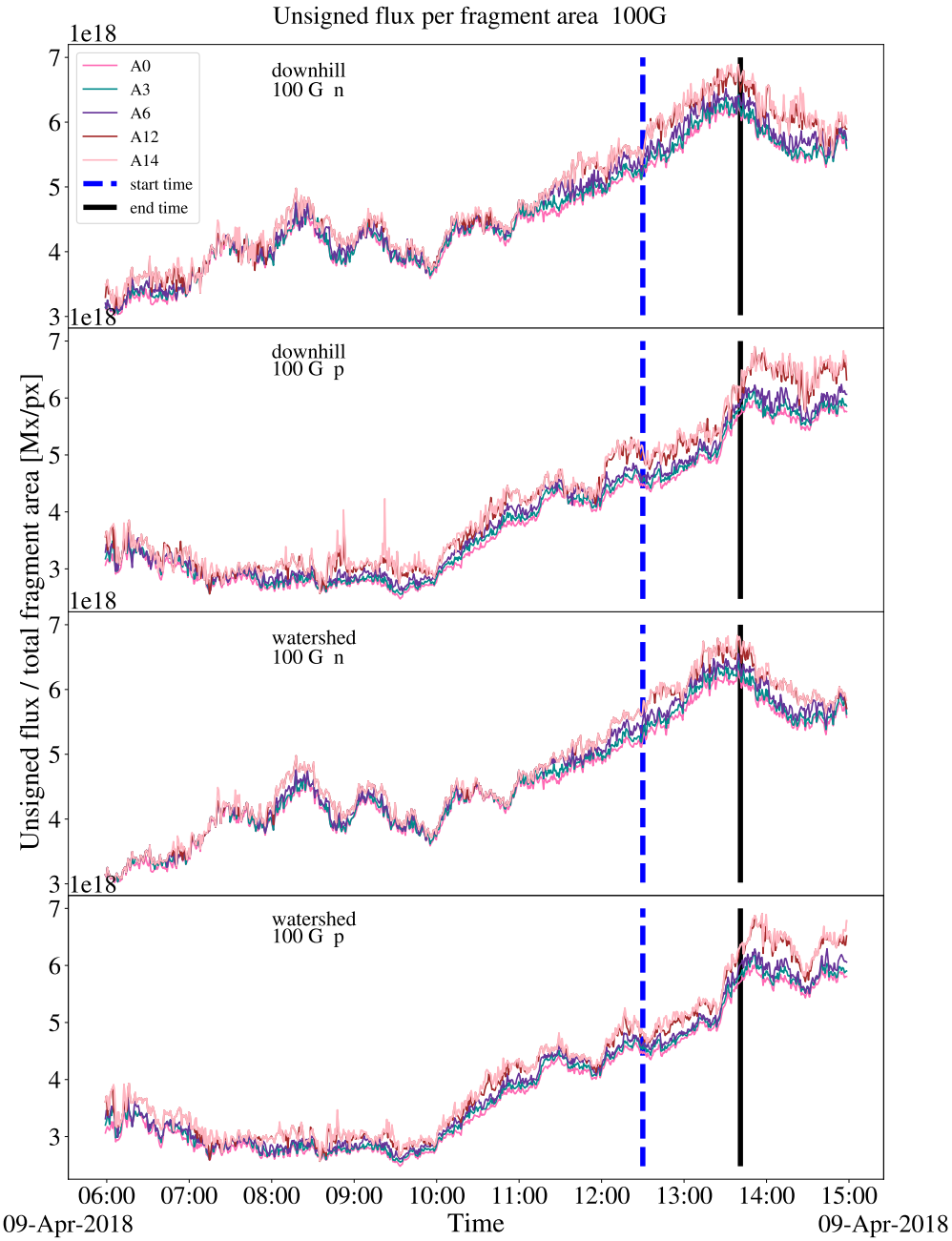

Figure 5.13: As in Figure 5.12, but with a magnetic field threshold of $100G$.

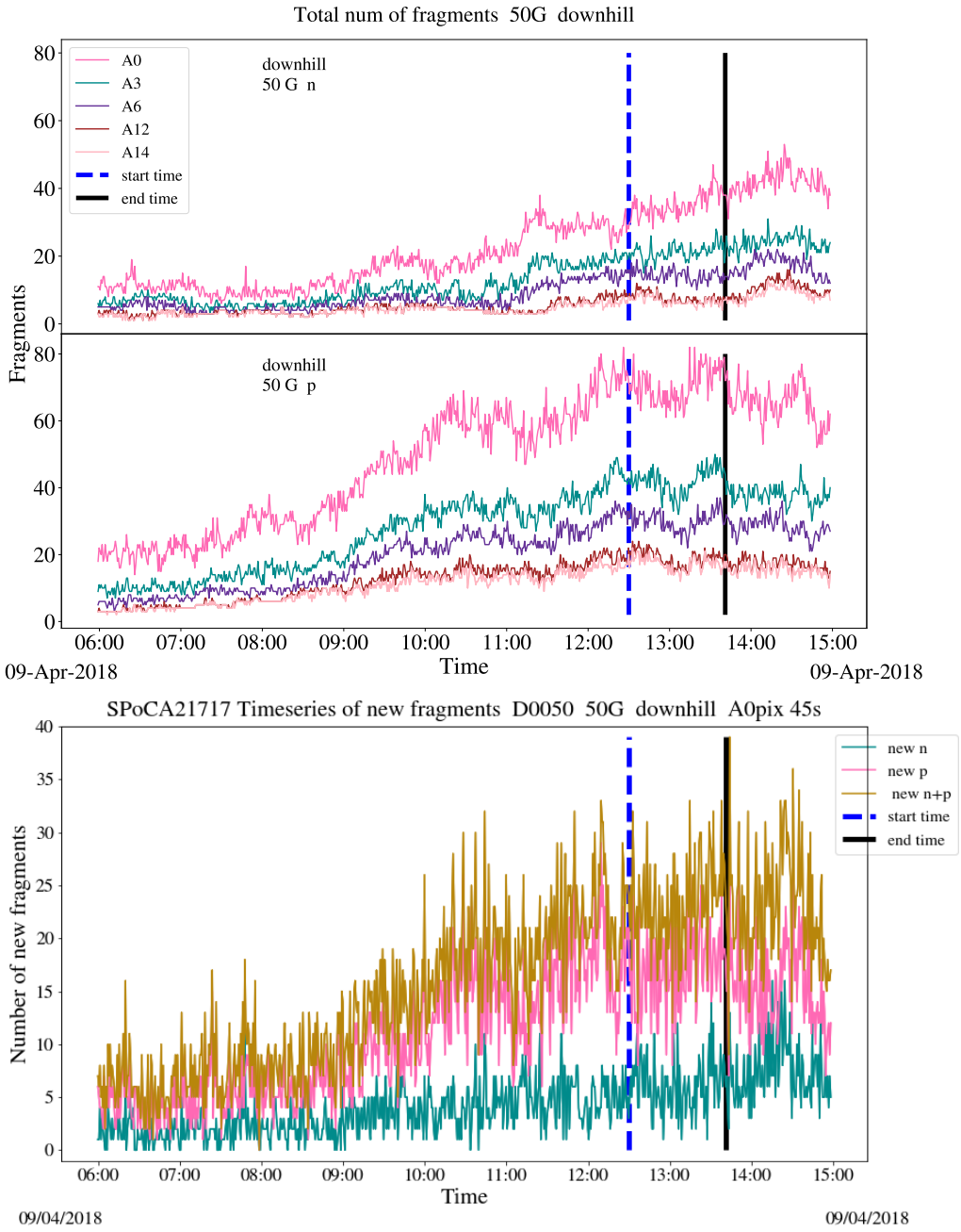

Figure 5.14: Top panel: Timeseries of the total number of fragments for region SPoCA21717, using downhill fragmentation, magnetic field threshold $\geq |50G|$ and angular distance limit ≤ 0.05 degrees . Rows alternate from negative (n) to positive (p). The different coloured solid lines indicate the fragment area threshold. Bottom panel: Timeseries of the number of new fragments appearing for same region. Cyan indicates the number of new negatives fragments and pink of new positive, while golden shows all new fragments. The blue vertical dashed line shows the start time and the solid black the end time of the A2.5 GOES class flare.

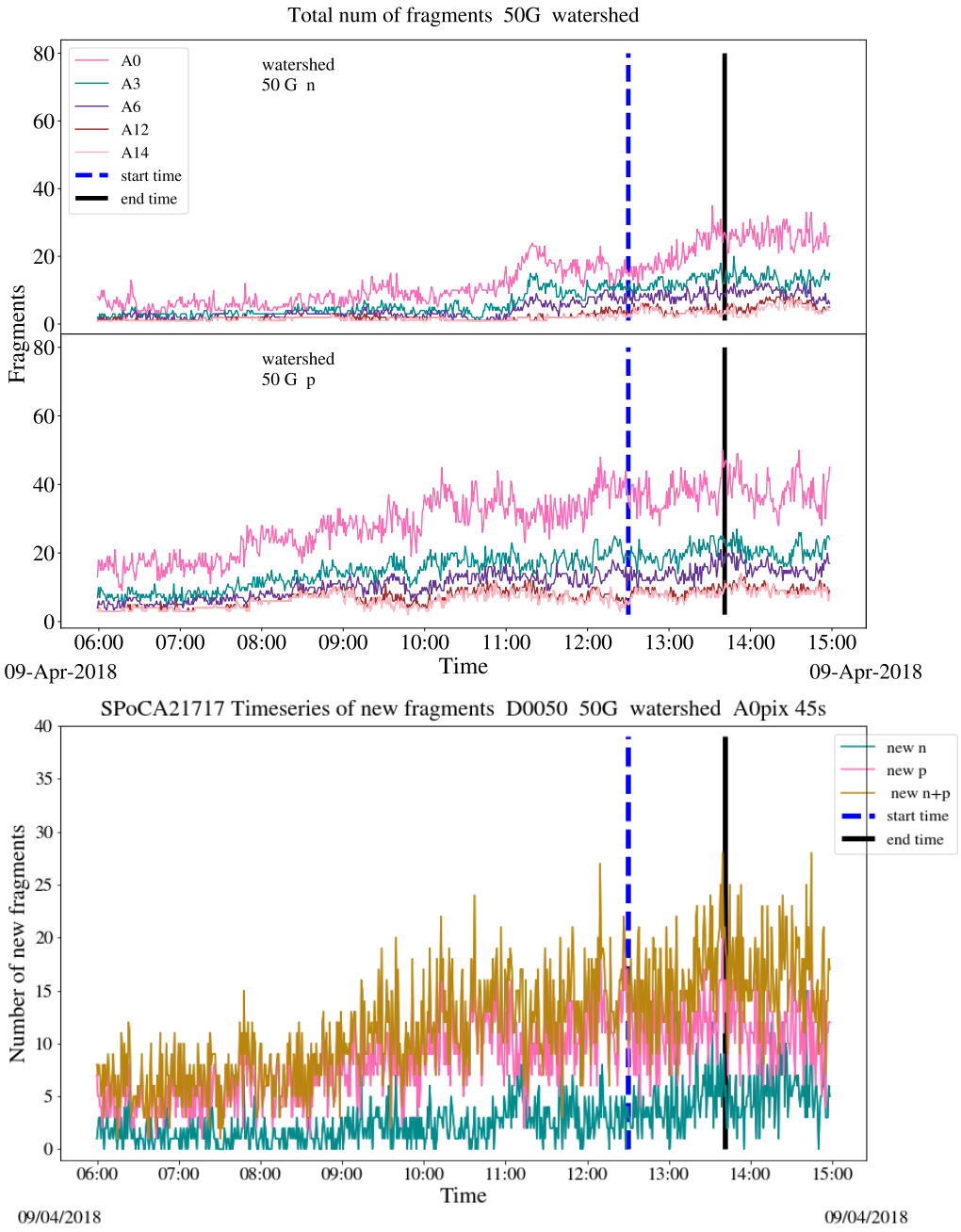

Figure 5.15: As Figure 5.14, for watershed fragmentation.

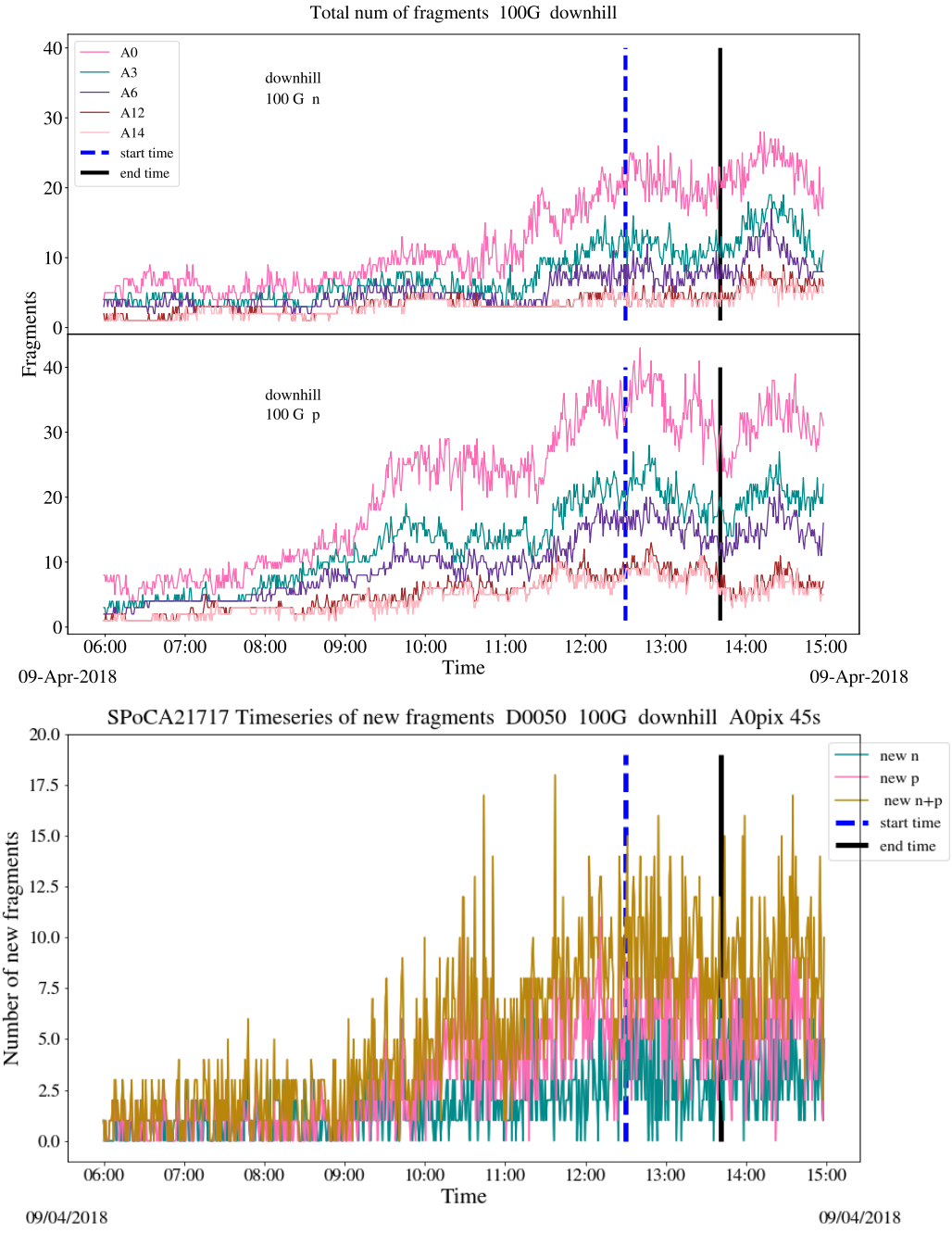

Figure 5.16: As in Figure 5.14, but with a magnetic field threshold of 100G.

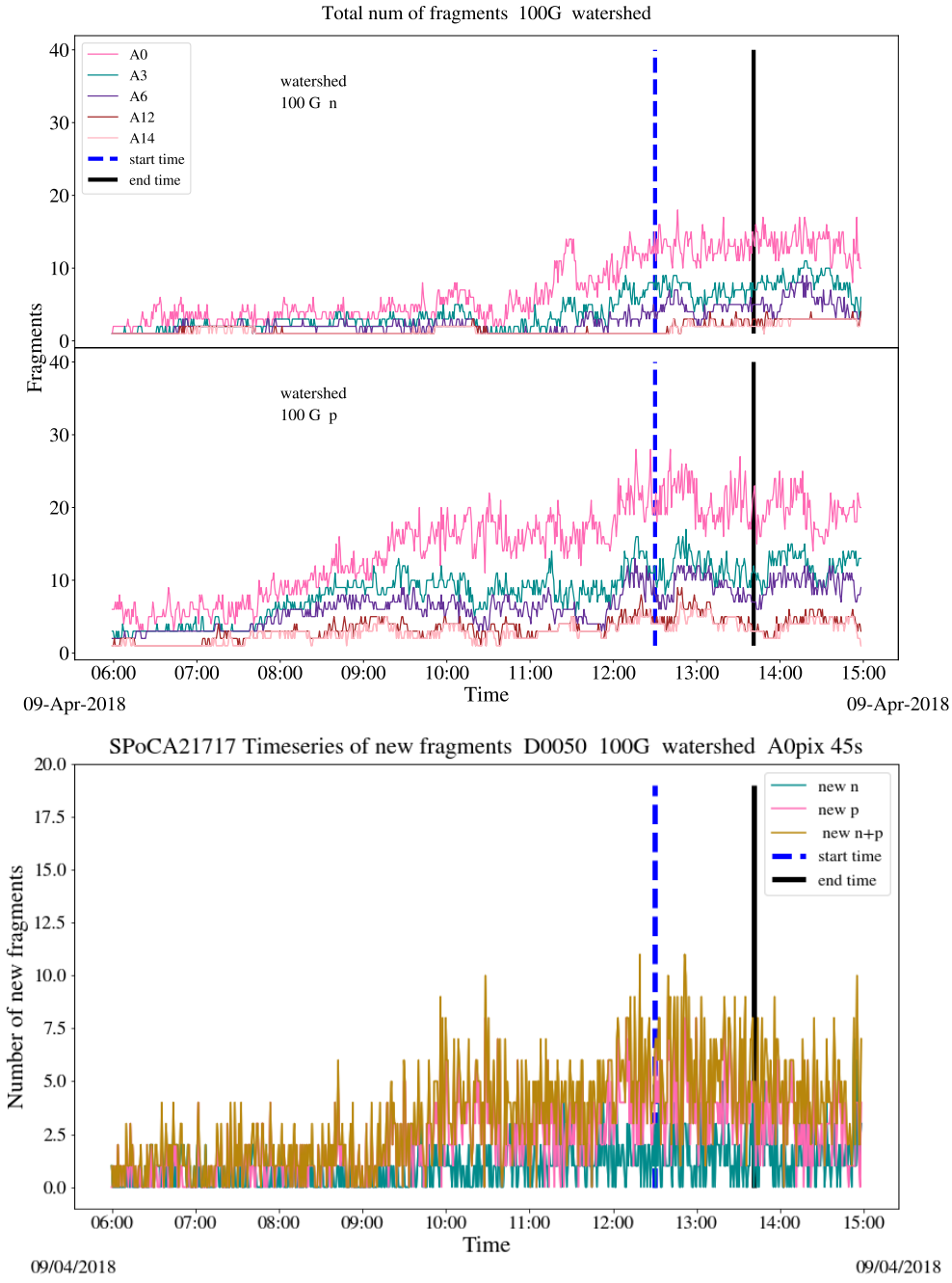

Figure 5.17: As in Figure 5.15, but with a magnetic field threshold of $100G$.

due to emergence of new flux or merging or splitting of existing fragments.

If we use the number of new fragments (Figures 5.14 - 5.15) as an indication of emerging flux we see that according to the downhill method, there was significant increase in emergence 4 hours before the flare took place, while watershed shows a general upwards trend. The difference in the behaviour of the algorithms is not necessarily due to the source, but to the properties of the different approaches. Viewing movies of the regions, watershed tends to create larger segments, with more stable positions, while downhill is more sensitive to slight changes of the intensity of the image fragmented, splitting regions in two more easily. Therefore, the high increase of new fragments could be attributed to the sensitivity of the algorithm to noise in the image.

From all the bulk properties plots, the ones that should differ the most from one fragmentation method to the other are the ones depending on the number of fragments; downhill is expected to produce more fragments than watershed, which is what we see. Therefore, the plots establish that the two methods work as expected and are consistent. Choosing between the two of them becomes a matter of stability of the location of the fragment. After time-tracking the fragments with the method described in Section 5.2.4, we created new movies for all submaps, with the labels of each tracked fragment overplotted at centroid position. Watershed segmentation returned tracked fragments whose centroid seemed more stable from frame to frame, compared to downhill.

5.3.3 Spatial evolution of longest-lived fragment

This section focuses on the movement of the fragments of region SPoCA21717. Figures 5.18-5.22 show the displacement of the centroid of each fragment per frame, where its location at first detection is taken as the reference point (0,0). Each of the figures has been run for a different lower fragment surface area, specifically 0, 3, 6, 12 and 14 pixels. The maximum distance a fragment is allowed to have moved from one frame to the next is 0.05 deg as we used 45 second cadence magnetograms. The size of the scatter plot indicates the surface area of the fragment in pixels and its colour is coded with time. The time on the colourbar covers the whole time range the active region was observed.

Note that with every run of the algorithm where any of the parameters (fragmentation method, lower surface area threshold, lower magnetic field threshold, fragment polarity) changes, the fragments were tracked and assigned a label unique to that specific run. Therefore, it should not be assumed that the figures portray the trail of the same fragment, although in some instances this can be the case. For example, in Figures 5.18 and 5.19, comparing the plots for downhill for the negative fragment, it is obvious the same fragment has been tracked. However, comparing the trails for downhill for the positive, it becomes apparent that different fragments have lived for the longest time in each run.

For the negative field, the downhill fragmentation (top left panel) seems to have tracked the same fragment for all area thresholds. As the time evolves, the centroid longitudinal displacement $x_i - x_0$ is positive, meaning the fragment moves to Sun West. Watershed (top right panel) seems to present the trail of two different fragments. The trail in Figures 5.18-5.19 also moved to Sun West, while in Figures 5.20-5.22 it wobbles about its location of first detection, slowly moving to Sun East.

For the positive field, the downhill fragmentation (bottom left panel) seems to have tracked three different fragments. In Figure 5.18, the fragment centroid longitudinal displacement $x_i - x_0$ is negative, meaning the fragment moves to Sun East. The same applies for Figures 5.21-5.22. In Figures 5.19-5.20, it wobbles about its location of first detection, slowly moving towards the opposite direction, Sun West. Watershed seems also to present the trail of three different fragments. In Figures 5.18-5.20 the fragment smoothly moves to Sun East, while the fragments in Figures 5.21 and 5.22 wobble about location of first direction or slowly move to Sun West.

These plots did not show much more details about the drift of the region. They follow the general pattern that we see during the movies, where the positive and negative polarities pull apart from each other, with the negative polarity moving to the western part and the positive one to the eastern part of the Sun. A next step would be to average the displacement of all fragments with time and calculate their speed from frame to frame, to see if the region had a preferred drift.

To sum up, in this Chapter we presented in detail two methods of fragmenting LoS magnetograms as well as a method of tracking them with time. We tested

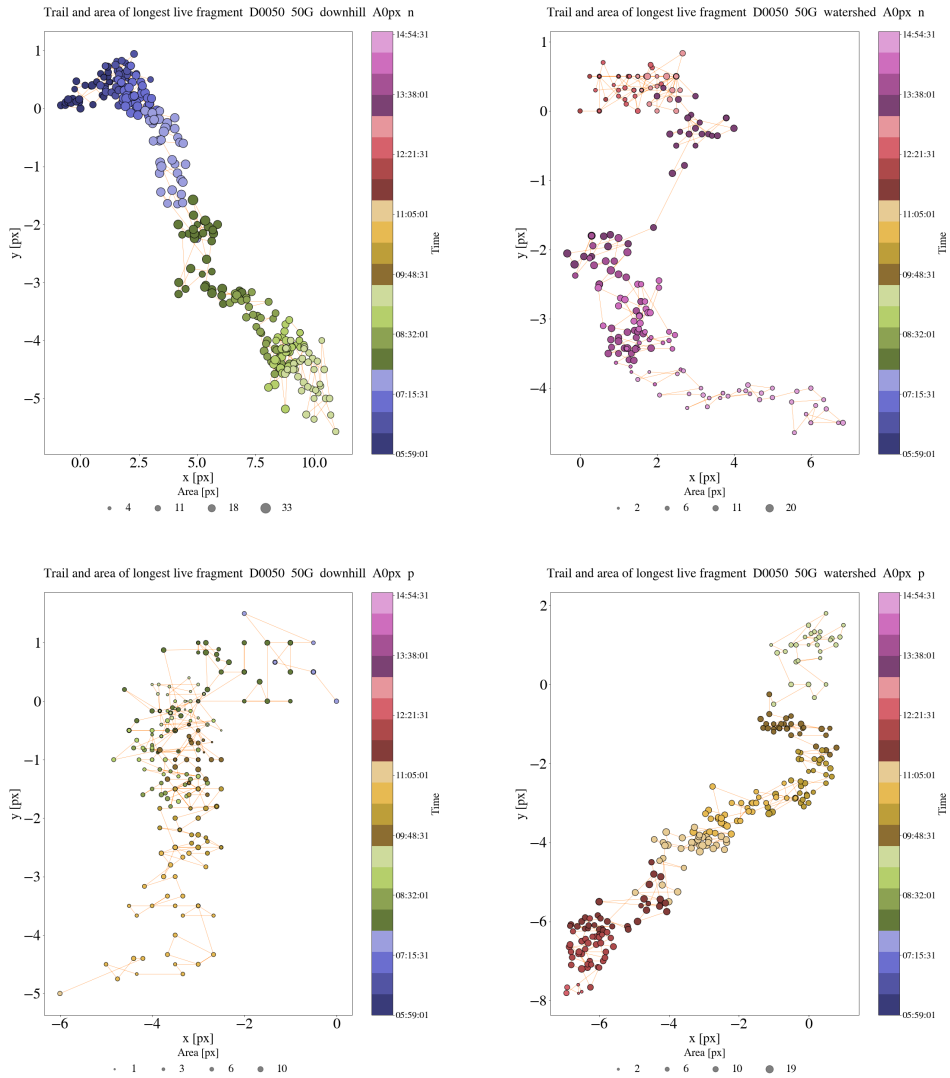

Figure 5.18: Timeseries of the x and y position (in pixels) of the geometric centroid of the fragment that was tracked for the longest time during this observation. The position given is relative to the position the fragment was first detected. All fragments with area of at least 0 pixels are included. The colour of the bullets changes with time from blue to red and their size indicates the surface area of the fragment, in pixels. Shown are the result for the downhill method (left column), watershed method (right column) and the longest lived negative (top) and positive (bottom) fragments. Bottom of figure: Fragment surface area legend. The first and last value in the legend represent the minimum and maximum surface area of the fragment tracked.

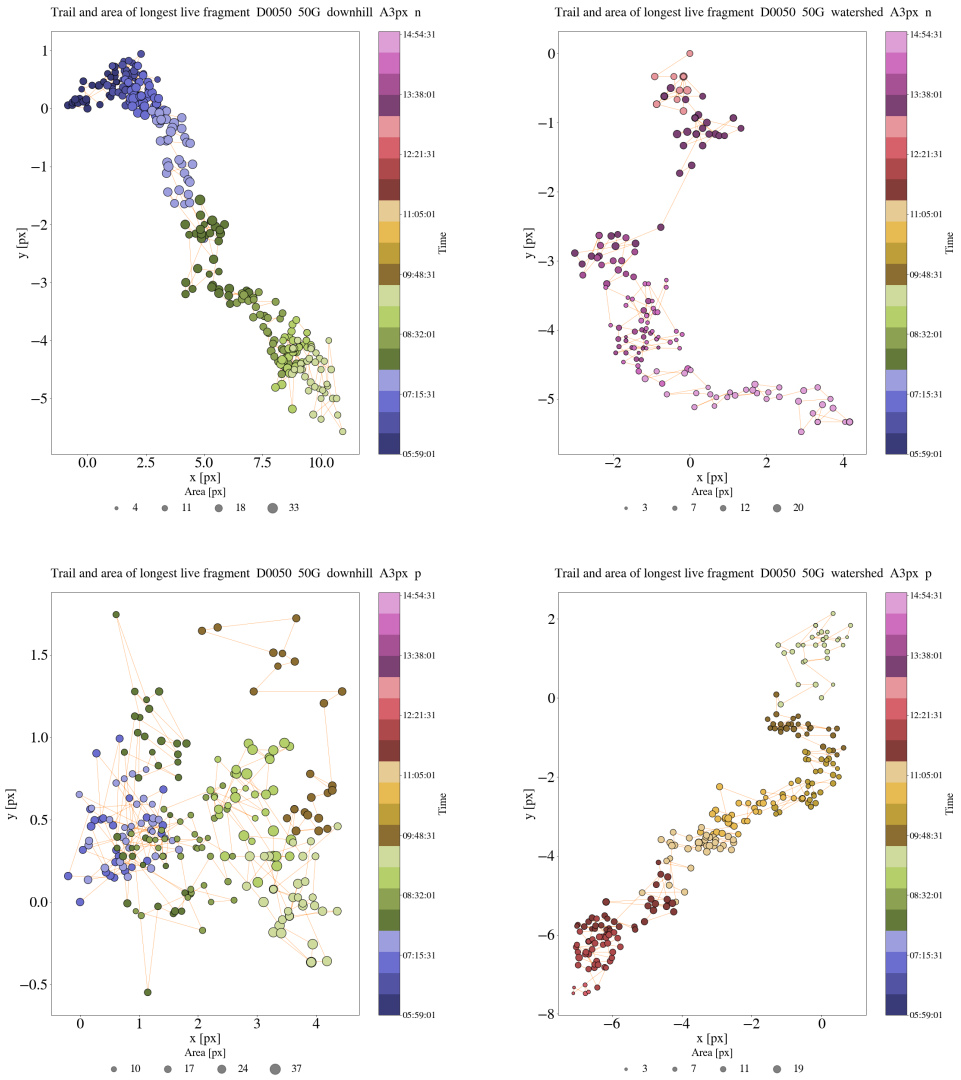

Figure 5.19: As Figure 5.18 but with a fragments area restriction of at least 3 pixels.

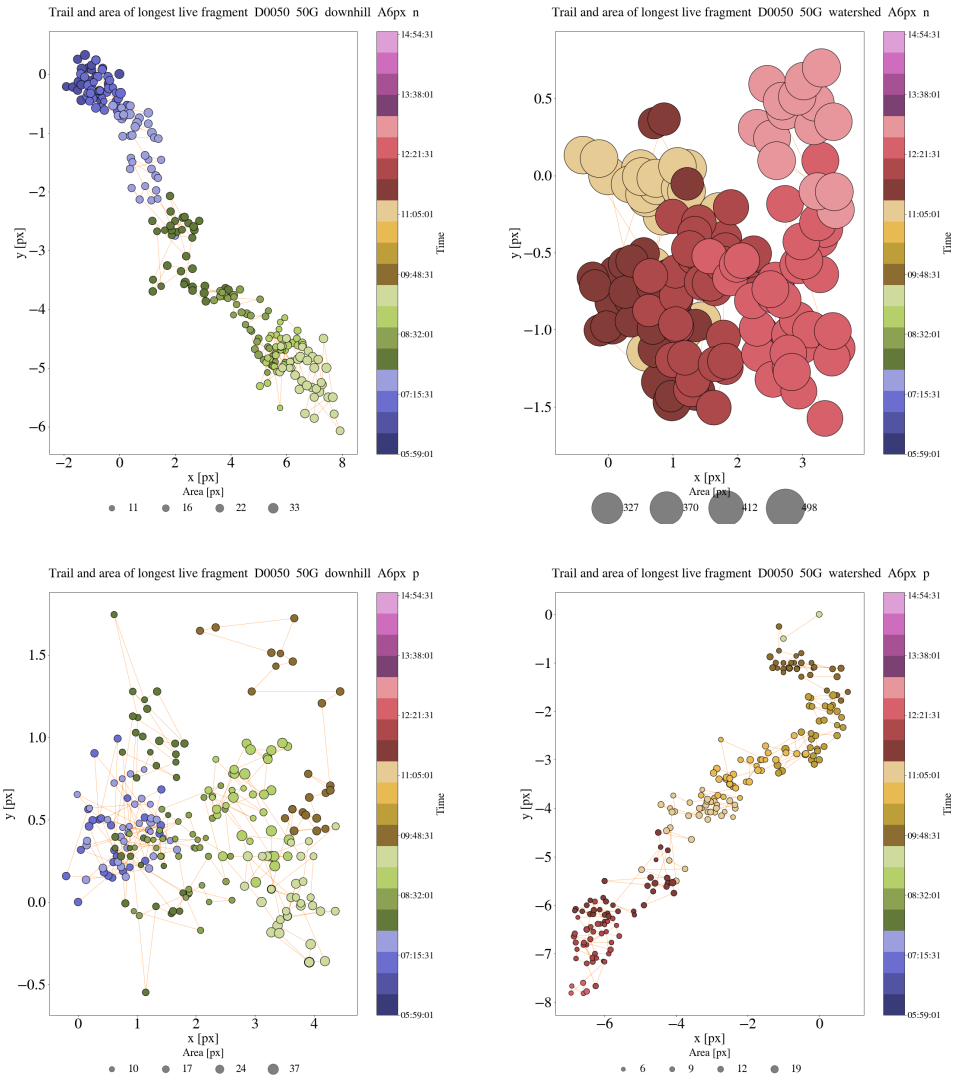

Figure 5.20: As Figure 5.18 but with a fragments area restriction of at least 6 pixels.

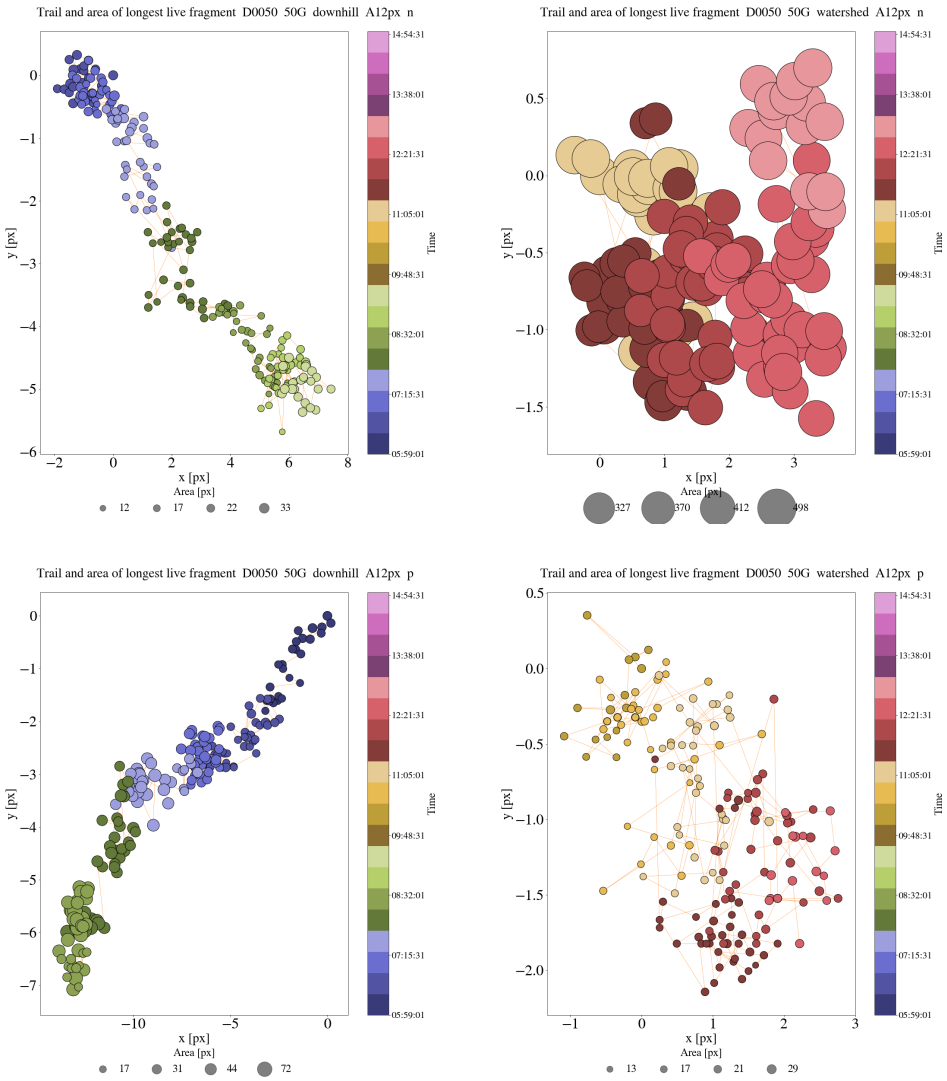

Figure 5.21: As Figure 5.18 but with a fragments area restriction of at least 12 pixels.

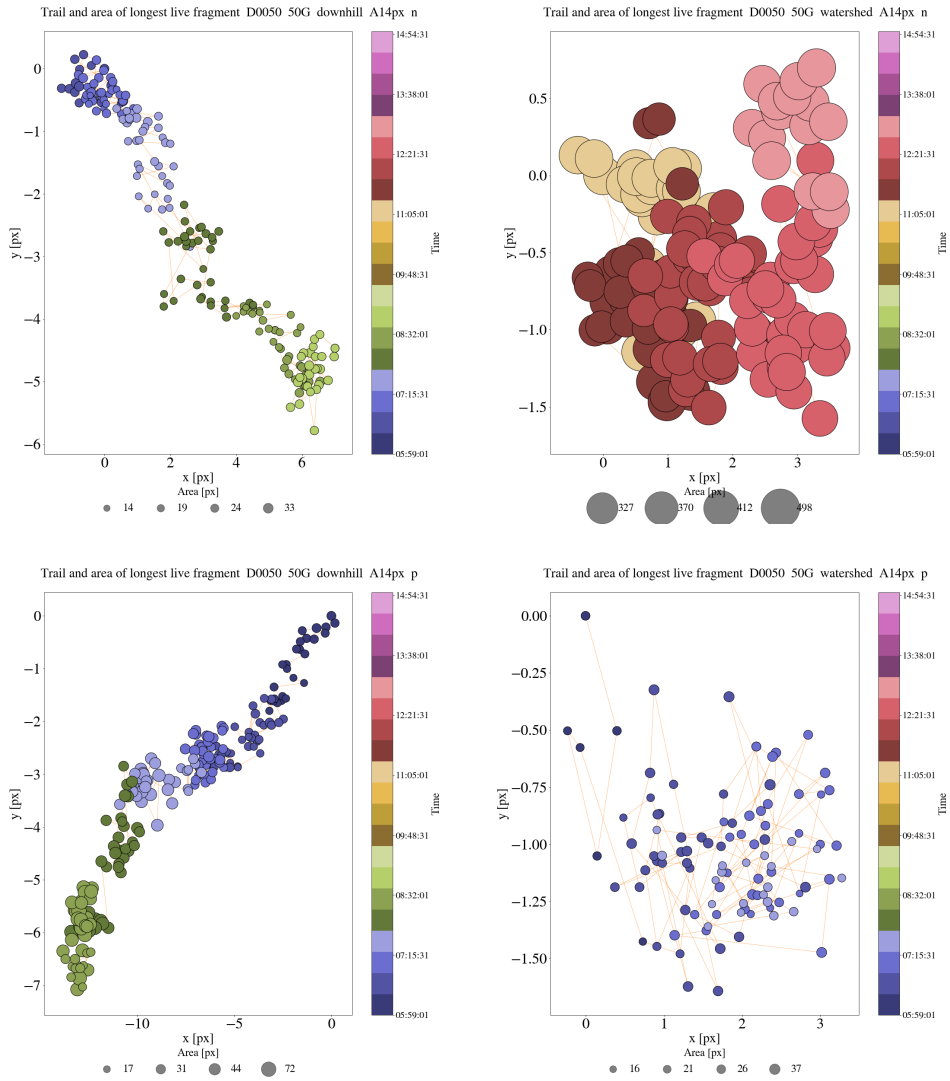

Figure 5.22: As Figure 5.18 but with a fragments area restriction of at least 14 pixels.

them on a small flux emergence event and found that they are stable, and have the expected behaviour. We determined that the two approaches give similar results, with Downhill being more susceptible to noise (helped also by movies created from the products of the pipeline). We identified ways to determine a magnetic field threshold and made a decision on which values are the best for each threshold. Additionally, we calculated the bulk properties of the negative and positive fragments and plotted them with time, alongside the start and end time of a A2.5 GOES flare that took place in the region. We found that the increase in fragment area stopped for the duration of the flare and resumed afterwards. Similarly with flux, there were some decreases on total unsigned flux during and right after the end of the flare. There were no changes for the average area and flux. We also concluded that an area threshold has no significant effect on the profile of the bulk properties.

In the next chapter, we apply the same process on three microflaring regions to investigate whether there is a consistent change in magnetograms before periods of repeatedly microflaring activity.

Chapter 6

Magnetic tracking of microflaring regions

Having established the methodology to use, tested for its validity and performance and determined the thresholds to be applied, this Chapter is dedicated to applying the process on appropriate active regions. Ultimately, we want to investigate the question of whether there are detectable changes of the B_{LOS} that result in multiple small flares (i.e. microflares) and in such a case, what are those changes.

Sudol & Harvey (2005) in a statistical study found permanent changes in the background flux of the magnetic field that last as little as 10 minutes for X-class flares, confirmed by Petrie & Sudol (2010) also for M flares. There were both increases and decreases of the background level, with the decreases being 1.4 times more frequent. Specifically weak field are more likely to decrease and strong fields more likely to increase. In addition, microflares are typically events of shorter duration of just a few to tens of minutes (Christe et al. 2008). The Heleioseismic and Magnetic Imager (HMI) (see Section 2.2) offers LoS data in two different cadences, 45 and 720 seconds. Therefore, in order to see the ΔB_{LOS} possibly related or leading to microflares, we would need to use the 45 seconds dataset. A 720 seconds cadence would show more readily the general behaviour of the region.

In Chapter 5 we established that from the two segmentation methods tested, Watershed is the most stable, whilst not losing much information through the internal checks for over-segmentation.

In the application of a variety of limits on the least area that the pixels of the test region should have, we saw no effect in the resulting figures (see Section 5.3.2, Figures 5.4 - 5.13). Additionally, in movies of fragmented regions where the location of the RHESSI flares was overplotted, flares tended to happen around small fragments. As a result, no area restriction is being applied in this part of the analysis, so the fragments around which flares happened are being tracked.

Finally, when tracking the fragments and applying a variety of angular distance thresholds, the most appropriate limits on how much a fragment is allowed to move from frame to frame was determined to be 0.05 deg for 45s data and 0.15 deg for the 720s datasets. This roughly corresponds to 1 pixel per frame, depending on the coordinates of the pixels and time of observation.

Section 6.1 expounds the method of selecting appropriate microflaring regions, while Section 6.2 contains the results of the analysis. Furthermore, maps of HMI data have quicklook RHESSI image overplotted, to indicate the full structure of the flare (footpoints and loop) and not just the centroid of the emission.

6.1 Selection of microflaring active regions

In order to identify microflaring active regions, we made use of the RHESSI flarelist we created for the analysis in Chapter 3. That was a list of all flares recorded by the RHESSI instrument from 12-Feb-2002 to 23-Feb-2016, complete with GOES flux information and corrected for non-solar events.

A desirable active region had to satisfy the following criteria:

1. Have longitude no more than 600 arcseconds, as that is the limit where the downhill fragmentation provides reliable results (Watson 2012).

2. Not be highly sheared as the downhill fragmentation does not work well on such regions (Watson 2012).

3. Not have fully formed before becoming visible in order to reduce the risk of studying a region that has already flared.

4. The region has to have produced a series of microflares, either

    - in a long series of flaring,

Table 6.1: List of active regions used (first column), with their flares reported from SolarMonitor(second column), RHESSI flares determined to be originating from them (third column) and the time the regions emerged before flaring (forth column).

NOAA number	Flares reported on Solar Monitor	RHESSI flares	Time of emergence before flaring
11630	C1.4/C5.5	16 A, 3 B, 1 C	72 hours
11819	-	4 A and 2 B	81 hours
12234	C3.9/C1.7/C4.0	6 A, 2 B, 2 C	19 hours

Table 6.2: List of active regions used, with their McIntosh and Hale class.

NOAA number	Mcintosh class	Hale class
11630	Cro/Cro/Dao/Dai/Cai/Dao	consistently β
11819	Axx/Bxo/Hrx/Cro/Dso/Cao/Bxo	$\alpha/\beta/\alpha/\beta/\beta/\beta/\beta$
12234	Cro/Dac/Dao/Cao/Cso/Hsx/Hsx/Hsx	$\beta/\beta\gamma/\beta\gamma/\beta/\beta/\alpha/\alpha/\alpha$

- flaring with bursts of microflares,
- being quiet and then flaring,
- flaring while emerging,
- being already established before flaring.

Table 6.1 lists the active regions we identified using the RHESSI flarelist. The regions had a flare of C5.5-class or less (X-ray peak flux at least 5×10^{-6} W m^{-2}), with longitudes less than or equal to |600| arcseconds. Six candidate active regions were identified but these three active regions were the most suitable. Table 6.2 documents their McIntosh sunspot (McIntosh 1990) and Hale region classification (Hale et al. 1919), as given by the SolarMonitor webpage[1]. One reason potential candidate regions were not selected was due to the fact that they were formed at about |600| arcseconds in longitude and were not deemed ideal for the downhill algorithm, or they were in very close proximity of a much larger region, making

[1]https://www.solarmonitor.org/

Table 6.3: RHESSI flares for region AR 11630.

GOES class	Start time	Peak time	End time
B4.9	09/12/2012 19:55	09/12/2012 20:01	09/12/2012 20:04
B1.2	09/12/2012 20:04	09/12/2012 20:07	09/12/2012 20:14
A6.1	09/12/2012 20:21	09/12/2012 20:27	09/12/2012 20:30
A3.5	10/12/2012 00:21	10/12/2012 00:25	10/12/2012 00:32
A3.7	10/12/2012 02:06	10/12/2012 02:06	10/12/2012 02:09
A9.1	10/12/2012 05:21	10/12/2012 05:23	10/12/2012 05:26
A9.9	10/12/2012 05:39	10/12/2012 05:42	10/12/2012 05:46
A2.6	10/12/2012 05:46	10/12/2012 05:47	10/12/2012 05:48
C5.3	10/12/2012 05:48	10/12/2012 05:57	10/12/2012 06:04
A3.1	10/12/2012 09:10	10/12/2012 09:12	10/12/2012 09:13
A2.4	10/12/2012 09:51	10/12/2012 09:51	10/12/2012 09:52
A3.9	10/12/2012 11:26	10/12/2012 11:27	10/12/2012 11:30
A9.6	11/12/2012 03:55	11/12/2012 03:57	11/12/2012 04:03
A2.1	11/12/2012 07:05	11/12/2012 07:06	11/12/2012 07:08
A8.5	11/12/2012 07:10	11/12/2012 07:14	11/12/2012 07:18
B3.5	12/12/2012 00:03	12/12/2012 00:08	12/12/2012 00:15
A2.6	12/12/2012 00:21	12/12/2012 00:22	12/12/2012 00:23
A4.6	12/12/2012 02:13	12/12/2012 02:14	12/12/2012 02:20
A3.5	12/12/2012 05:08	12/12/2012 05:08	12/12/2012 05:09
A7.1	12/12/2012 08:19	12/12/2012 08:20	12/12/2012 08:31

deciphering which field belong to which region very difficult.

6.2 Analysis of microflaring active regions

6.2.1 AR 11630

Active region NOAA 11630 first emerged close to the centre of the Sun approximately on 6-Dec-2012 18:00 UTC and formed as a region (i.e. there was a clear establishment of sunspots) on 8 December 2012 06:00:00 UTC . The first RHESSI flare was recorded on 09 December 2012 19:55:16 UTC but emission can be seen

in AIA from 18:30:00 UTC onwards, while the analysis lasted from 9 December 2012 12:58:09 until 12 December 2012 17:46:09 UTC. It was selected due to its location of first appearance, at longitude about −180 arcsecs. During the time of the analysis it crosses the disk and by the end it has longitude almost 584 arcsecs. The region crosses the Central Meridian on 10 December 2012. This will have an impact on the profiles of the bulk properties, as the LoS component will be increasing approaching Sun-centre and decreasing approaching the limb. The region exhibited a long series of microflares, in small bursts. Table 6.3 shows a list of the 20 RHESSI flares that took place in the region.

Movies created in Helioviewer using the 171 and 193$\mathring{A}$ SDO/AIA channels show the region started from a bipolar configuration, reconnected with the surrounding field and ended up with a sigmoid structure.

Figure 6.1 presents the HMI map (in pixel coordinates) on 720s data with the contours of RHESSI image overplotted (pink and purple). The flare contours were created using the 6-12 keV bandwidth, with the CLEAN algorithm, detectors 3,5,6,7,9 and using the quicklook image time from the RHESSI database. Over this energy range a RHESSI image shows the position and shape of the thermal loop and possibly the footpoint emission of the microflare. The flare location that we also used in Chapter 3, is really the centroid of this 6-12 keV emission, found as part of the RHESSI quicklook products and flarelist. The contours of the fragments returned by the watershed algorithm are also given (cyan for negative and yellow for positive). Some of the flares mainly happened around the Polarity Inversion Line, as expected. The flare locations are mainly found around small fragments, which were small concentrations of flux that kept occurring throughout the entirety of the analysis. There is an exception for flares 12-Dec-2013 00:22UT and 02:10UT which were associated with a large negative fragment. Judging by the flare loop location, for the time profiles, we would expect that both polarities of the field will exhibit changes.

6.2.1.1 Time profiles of field changes

As in Section 5.3.2 of Chapter 5, here we are examining the bulk properties of the active region's B_{LOS} as a first step to see if there is a noticeable change about the times of the microflares. Due to the large timescales of the analysis, we are looking

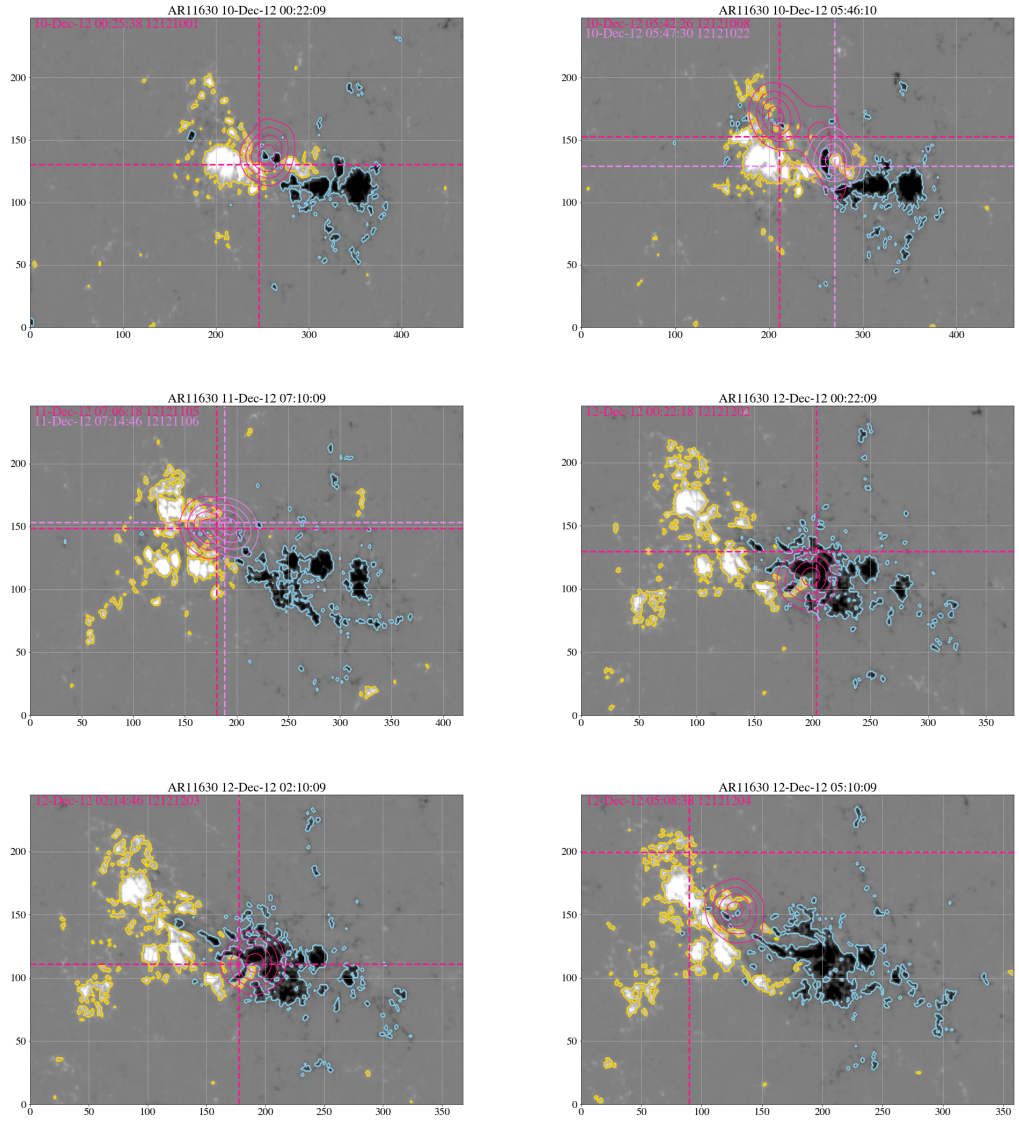

Figure 6.1: HMI submaps of region AR 11630, with pink contours overplotted indicating the RHESSI flare loops. With coloured text the peak time of the flare. The contours indicate the fragments identified by the Watershed fragmentation (positive: yellow, negative: cyan).

for permanent changes in the background level of the magnetic field, meaning a change that happened before or during the flare and the field did not immediately return to its previous state. Therefore, we are looking for a profile that looked different close in time before and after a flare occurred. This was the first step, exploring what can be done in future studies. Therefore, in this Chapter, we have not defined way to differentiate between the continually changing properties of the field and those occurring before or after flares. This step should be implemented in the future.

As for the results from testing region SPoCA 21717, Figures 6.2 - 6.6 present the time profile of the total surface fragment area, the unsigned flux, the average area and average unsigned flux per fragment as well as the average unsigned flux per area, as returned from each fragmentation method and for both datasets. Figures 6.7 - 6.8 show the number of fragments and the number of new fragments registered, for all fragmentation methods and datasets. The vertical lines indicate the start time of the flares observed, colour-coded according to the GOES class of the flares.

The first impression given from the plots is the similarity between the 45s and 720s data. Both sets seem suitable for studying the general behaviour of the region and the changes that are associated with flares, if any, are slight. For AR 11630 a comparison will be made between the plots from downhill and watershed for the 45s data, but for the last two regions we will focus on the results from watershed, due to its stability. The 720s data are also given for comparison, but due to the cadence they cannot show small changes in the field, for these shorter duration flares.

For region AR 11630, the two methods returned identical results in both cadence data for the total unsigned flux, total fragment area, and unsigned flux per area. The profiles of those properties should be independent of the fragmentation method since they are the properties of the whole image. This is what we expected and matches the results from the testing region in Chapter 5. The region started close to Sun centre and by the time the first 12 flares happened it has reached a complete central location.

As far as the general behaviour of Figures 6.2 and 6.3 is concerned, we see that the fragment area and flux exhibit a steady increase in time as it starts crossing

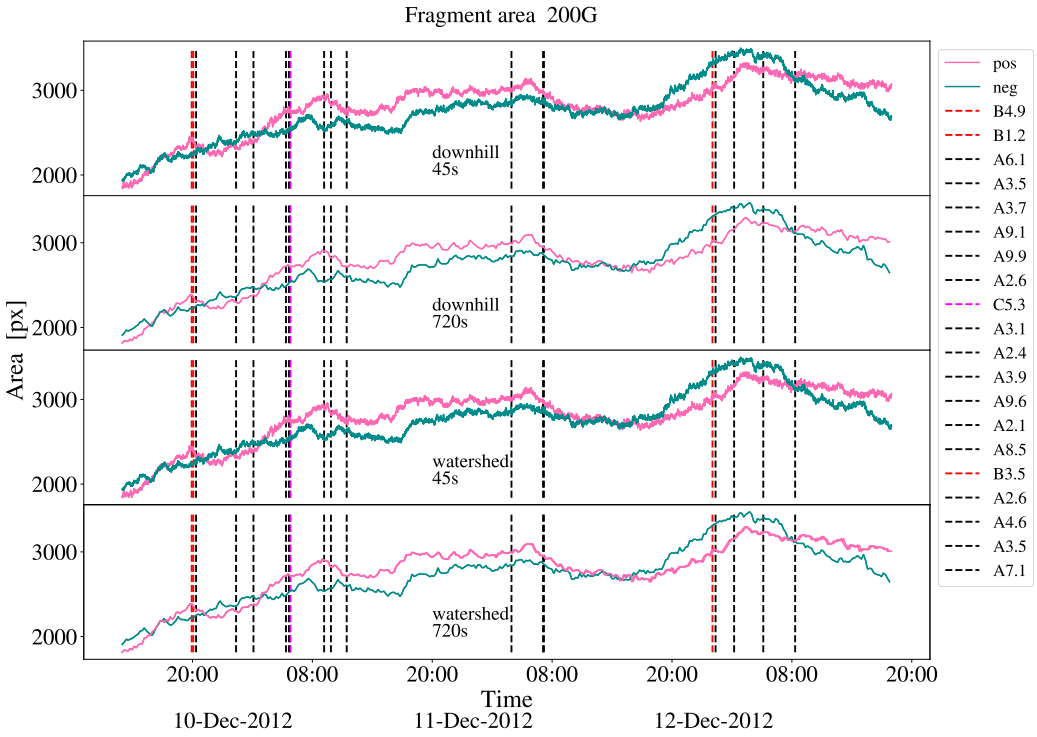

Figure 6.2: Total area from all fragments for region AR 11630, using downhill fragmentation (top two panels) and watershed fragmentation method (bottom two panels), with magnetic field threshold of $200G$. Green line is for negative fragments and pink for positives. The vertical dashed lines indicate the start time of the RHESSI flares (black: A, red: B, purple: C-class).

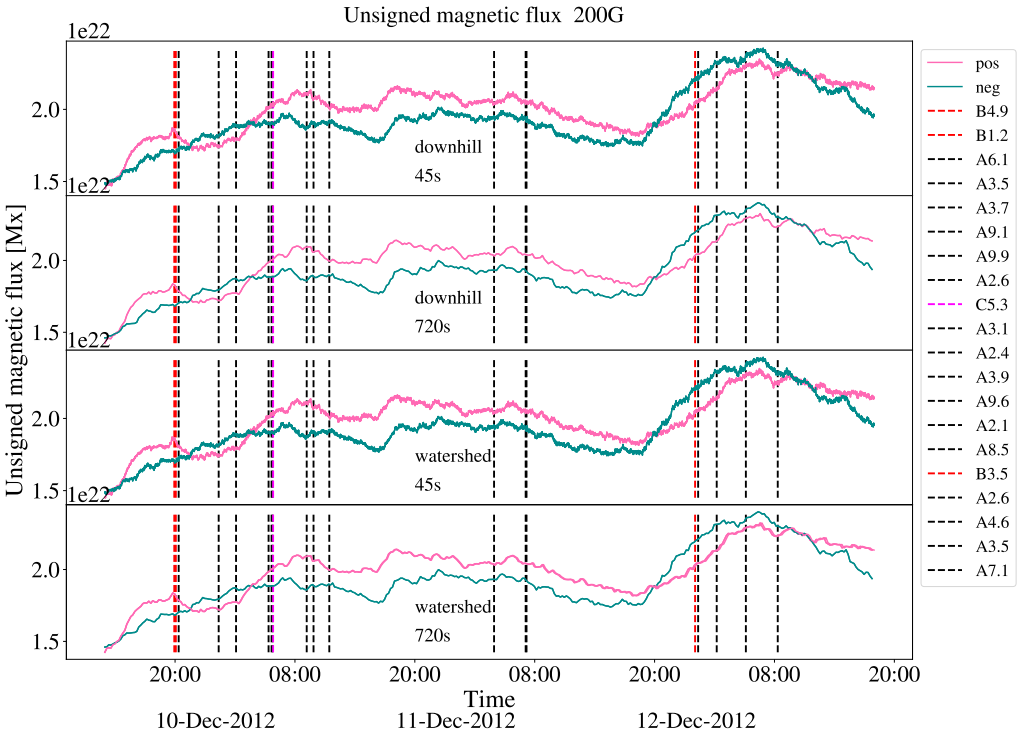

Figure 6.3: Total unsigned flux from all fragments for region AR 11630, using downhill fragmentation (top two panels) and watershed fragmentation method (bottom two panels), with magnetic field threshold of $200G$. Green line is for negative fragments and pink for positives. The vertical dashed lines indicate the start time of the RHESSI flares(black: A, red: B, purple: C-class).

the Central Meridian. The increase is halted about 10-Dec-2012 11:26UT, which is after the time of the first 12 microflares. It then plateaus for the period of a day while 3 flares occur and then again slightly decreases about 11-Dec-2012 07:10UT. Finally, it increases on 12-Dec-2012 while 5 flares take place. The first flux increase could be associated with geometrical effects. However, the second phase of flux positive gradient has to be genuine flux emergence, since the region was at Sun West by that point. In this plot, there is not specific pattern of behaviour that seems to be connected with the time of flare occurrence. It is noteworthy that the region seems to also be shearing during 10-Dec (determined by watching movies of the HMI maps), which explains the high rate of flaring. Then the fragment area plateaus for as long as the region crosses the disk. There is a time of reconfiguration, leading to a more complex structure until around 11-Dec-2014 21:00 both the area and flux start increasing and finally flaring.

When looking for changes in the 45s data about the time of the microflares, differences start to arise. In Figure 6.2, there seems to be changes in the positive fragments associated with the occurrence of the microflares. However, these could be coincidences. For example, focussing in Figure 6.2, on the time of the first 4 flares (9-Dec-2012 20:21UT and 10-Dec-2012 00:21UT) as well as about the bundle of C and A flares (11-Dec-2012 05:48UT) there is a pattern of the first flare happening, a small increase in total area for positive occurs and then a decrease while leaving the negative unaffected. Similarly, the B and A flares at 12-Dec-2012 00:21UT occurred before a sudden temporary increase for the positive flux and area can be seen. On the other hand, there is generally an increasing trend for the negative fragments. However there are some periods in which there are similar changes in both the positive and negative field. The A-class flare at 10-Dec-2012 11:28UT happened about the time ofa slight increase, seen as a small bump to both polarities, for both fragmentations. The next three flares, (11-Dec-2012 03:55UT) and (11-Dec-2012 07:05UT and 07:10UT) occurred when the profile of the properties did not change at all. All these changes happened after the start time of the flare, with the exception of the decrease of the area in the very first flare, which happened before.

In summary, for Figure 6.2, for the positive fragments, in all cases of B and C class flares we saw small temporary increases in the fragment area both before

and after flares, while 8 out of the 9 instances where we had a lone A flare was followed by a change of the profile -increase (10-Dec-2012 09:51UT), slight increase (10-Dec-2012 05:48UT) or plateau (10-Dec-2012 03:55). None of the bigger flares seemed to be associated with any changes on the negative fragments and 4 out of 9 lone A flares happened before either a slight decrease (12-Dec-2012 02:13UT), an increase (10-Dec-2012 00:21UT) or a plateau (10-Dec-2012 03:55UT). This is surprising as one would expect more disruption to be associated with a larger flare.

Questioning why there was an increase in the fragment area of region AR 11630, the cases of a fragment having a larger area are:

- if it merges with another fragment
- if there is emergence
- if there is a tilt in the magnetic loop
- if the flux of the fragment goes above the flux threshold or the resolution of the instrument and more area is being picked up as a result (a phenomenon DeForest et al. (2007) defined as coalescence)

Movies created from the maps such as in Figure 6.1 show a lot more positive field arising and moving about, while the negative is concentrated with a relatively smaller area. Viewing similar movies of AIA data, we see the positive field interacting both with the negative and with the surrounding field, as the region changes from being bipolar to a more complicated structure. In addition, the flux limit seems to be an issue in this case, as the structure of the loops is present, implying that the field is there. As a result, there is a good reason to believe we chose a high flux threshold, missing some information.

Looking at the total unsigned magnetic flux in Figure 6.3, for the positive fragments, there was a noticeable profile about the time of the B and C class flares, with a sharp increase of flux right before the flare on 9-Dec-2012 20:21 and a slight, less sharp increase after the flare on 10-Dec-2012 5:48. The A class flares either happened before slight decreases, where the flux increase stopped or

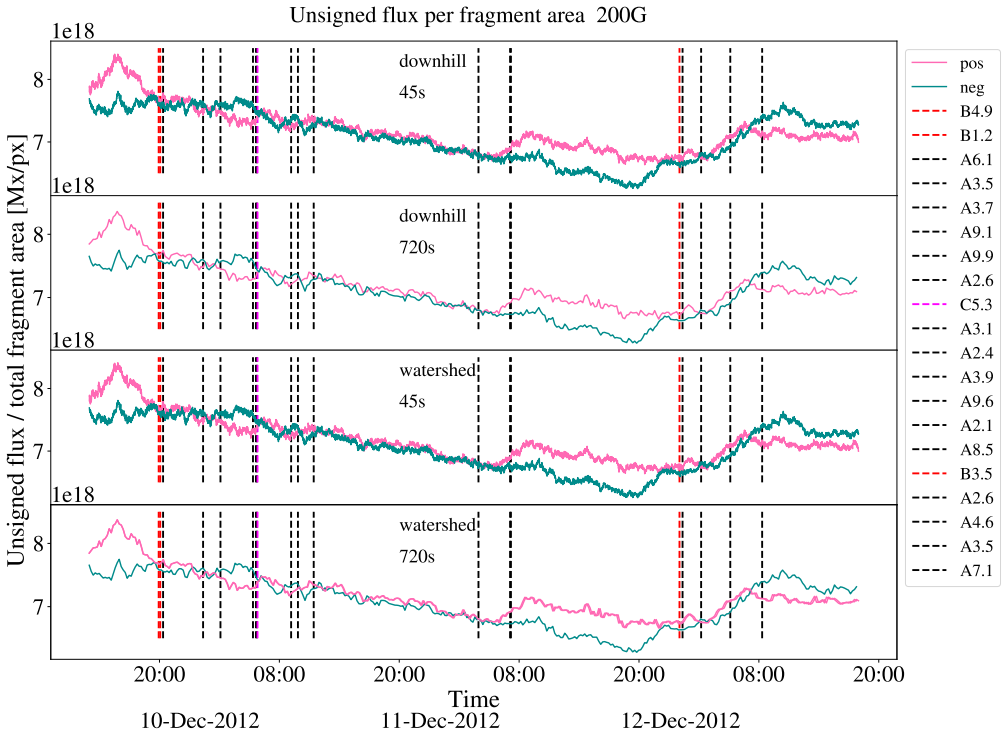

Figure 6.4: Average flux per fragment area for region AR 11630, using downhill fragmentation (top two panels) and watershed fragmentation method (bottom two panels), whit magnetic field threshold of 200G. Green line is for negative fragments and pink for positives. The vertical dashed lines indicate the start time of the RHESSI flares(black: A, red: B, purple: C-class).

plateaued. For the negative fragments, A flares were followed by either a slight decrease in flux or no changes happened about their occurrence time. This result for the negative fragments and the fact that the changes occurred before the flaring times agrees with Watson (2012), where changes of the field were recorded to be happening before the X-class flares.

In conclusion, increases in flux led to B and C class flares while A class flares were halting the increasing flux for the positive field. For the negative field there were a lot of instances where a decrease in the field was followed by A class flares.

Perhaps more important is Figure 6.4 which gives the result of the average unsigned flux per unit area. If there is emergence, this fraction should either stay constant or increase. If we have the same flux but the fragment area increases because the region is closer to disk centre or because it spreads out, this fraction

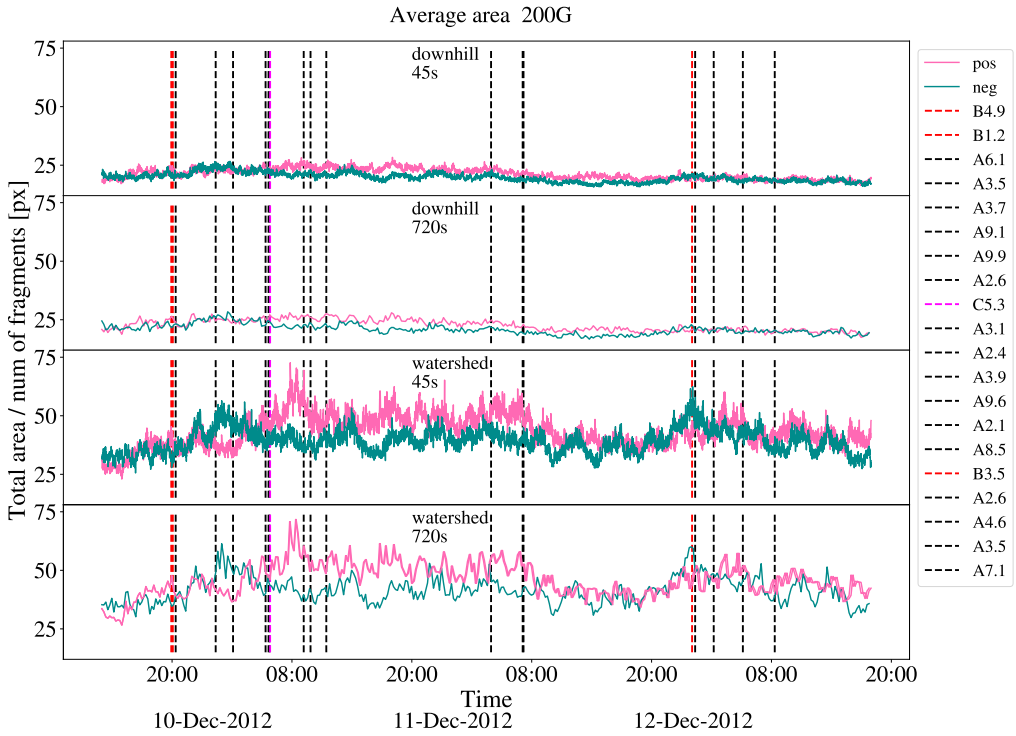

Figure 6.5: Average area per fragment for region AR 11630, using downhill fragmentation (top two panels) and watershed fragmentation method (bottom two panels),with magnetic field threshold of $200G$. Green line is for negative fragments and pink for positives. The vertical dashed lines indicate the start time of the RHESSI flares(black: A, red: B, purple: C-class).

will decrease. For the negative fragments, there is emergence before the first 12 flares, which continues for a total of 10 hours, followed by a decrease after 10-Dec-2012 06:00 UT. The field then spreads and possibly the resulting shear leads to the A class flares (10-Dec-2012 09:10 UT). Emergence can be detected for the negative fragments before a bundle of a B and 2 A-class flares take place on 12-Dec-2012 00:03 and the emergence continues for all remaining 5 flares. For the positive fragments, no specific pattern can be detected. The first 2 B class flares took place without positive emergence, there was emergence before the C class flare and there were A class flares in all cases where the average flux per area increases, decreases or plateaus. This plot suggests that emergence starts before microflares and continues during the flaring times for negative fragments and no pattern arising for the positive.

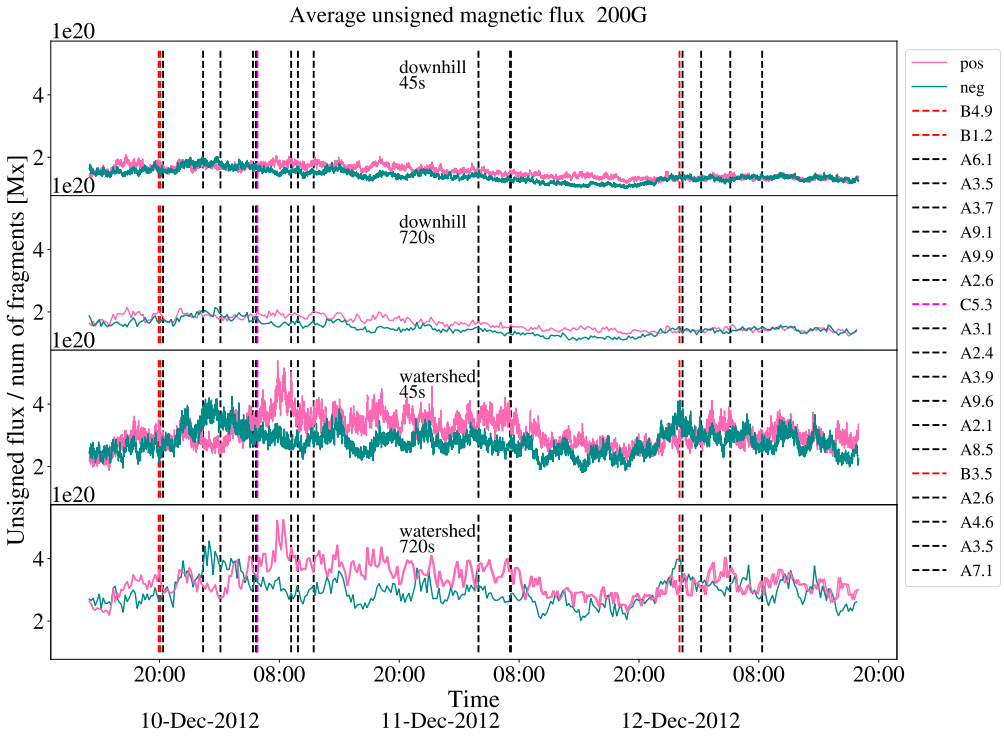

Figure 6.6: Average unsigned flux per fragment for region AR 11630, using downhill fragmentation (top two panels) and watershed fragmentation method (bottom two panels), with magnetic field threshold of $200G$. Green line is for negative fragments and pink for positives. The vertical dashed lines indicate the start time of the RHESSI flares(black: A, red: B, purple: C-class).

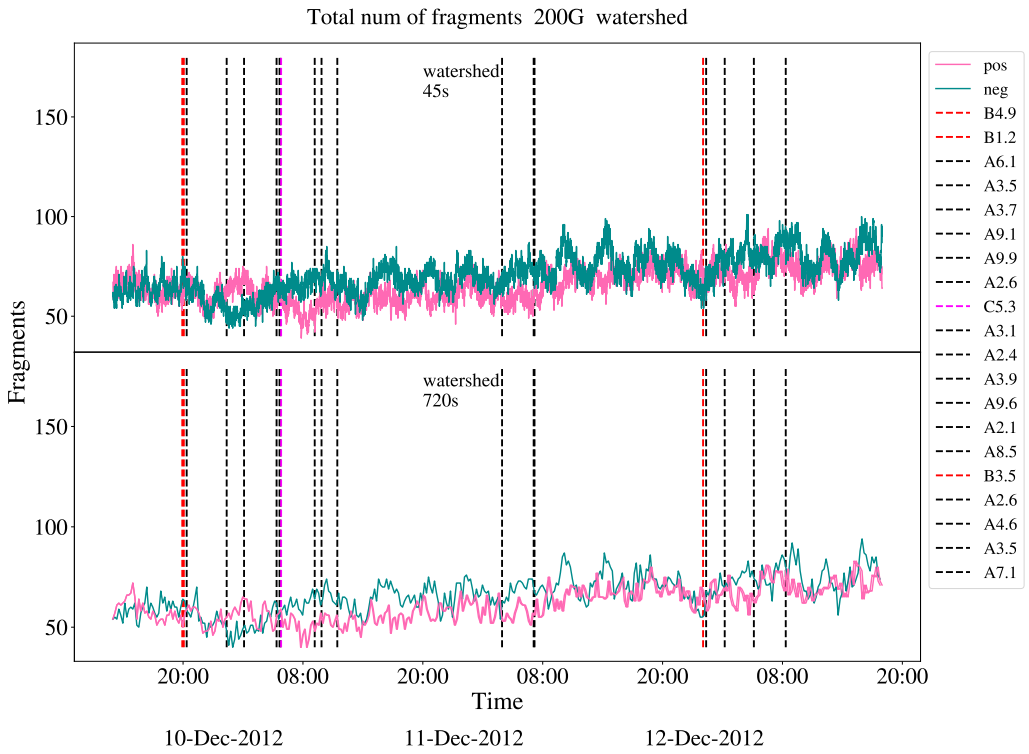

Figure 6.7: Total number of fragments for region AR11630, using watershed fragmentation and magnetic field threshold $\geq |200G|$. Green line is for negative fragments and pink for positives. The vertical dashed lines indicate the start time of the RHESSI flares(black: A, red: B, purple: C-class).

In Figures 6.5 and 6.6 we show the average fragment area and average unsigned flux per fragment. These will be different between the two methods as the downhill method segments images into smaller fragments, while watershed separates them into fewer larger fragments. The time evolution between downhill and watershed may seem different, but this is due to the fact that the y-axis has been normalised between the two fragmentation methods. Comparing the results between the 45s and 720s datasets, they do not give back exactly the same time evolution. This is both because 45s will be more noisy but also because 720s is too large a cadence to see field changes. The average area and flux will increase either when there is emergence, merging or the LoS component gets stronger. With these bulk properties there appears to be no specific pattern of increase or decrease before or after a flare, either for the positive or negative fragments.

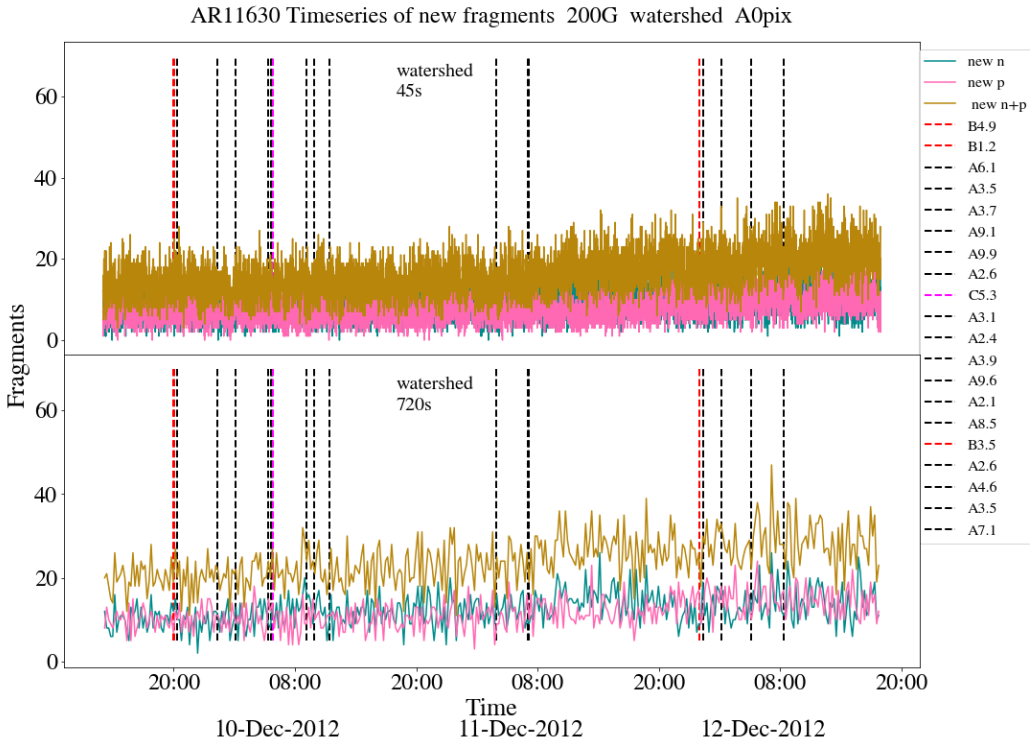

Figure 6.8: Number of new fragments appearing for region AR11630. With cyan the number of new negatives fragments, with pink the number of new positive fragments and with golden the number of all new fragments. The vertical dashed lines indicate the start time of the RHESSI flares(black: A, red: B, purple: C-class).

Finally, Figures 6.7-6.8 give the total number of fragments and number of new fragments. A fragment will be given a new label if it emerges, if it is result of splitting or if it moved further than the angular distance limit we chose. If two fragments merge, the larger fragment propagated to the new frame will not change labels. There is a general trend of more fragments as time progresses and the region evolves and this is also reflected in the plot of more new fragments. There does not seem to be an obvious change in the number fragments about the time of the flares.

6.2.1.2 Spatial evolution of fragments

We now look at the movement of the fragments for region AR 11630. Figure 6.9 presents the displacement of the centroid of each fragment per frame, with reference point the fragment location at first detection. For every frame, the fragment centroid pixel location at the initial frame $[x_0, y_0]$ was subtracted by the current pixel location of the centroid $[x_i, y_i]$. The plots were created for the 45s data with maximum angular distance limit of 0.05 deg for tracking the fragments from frame to frame. The size of the scatter plot symbol indicates the area of the fragment per frame in pixels and its colour is coded with time. The colourbar covers the entirety of the observation time - the initial time is dark blue and moves through to pink at the final time.

We opted for plotting the movement of the five longest-lived fragments (Figure 6.9 top row) and then repeat the process for 200 longest-lived fragments (Figure 6.9 bottom row) as a way to illustrate any apparent preferential movement of the fragments of the region. The average lifetime for the negative and positive fragments plotted on the top row was 15 hours. In the bottom row the lifetime of the fragments ranges from 1.7 to 23 hours. We keep in mind that Watson (2012), using downhill fragmentation, found no preferential drift for fragments tracked for less than a day. We compare their results with the watershed method.

These plots are in the pixel units of the submaps. The submaps themselves were differentially rotated before the fragmentation took place and the fragments properties calculated. As a result, a change in the centroid position should be a genuine movement of the fragment.

Figure 6.9 shows that in all cases the fragments generally spread out from their

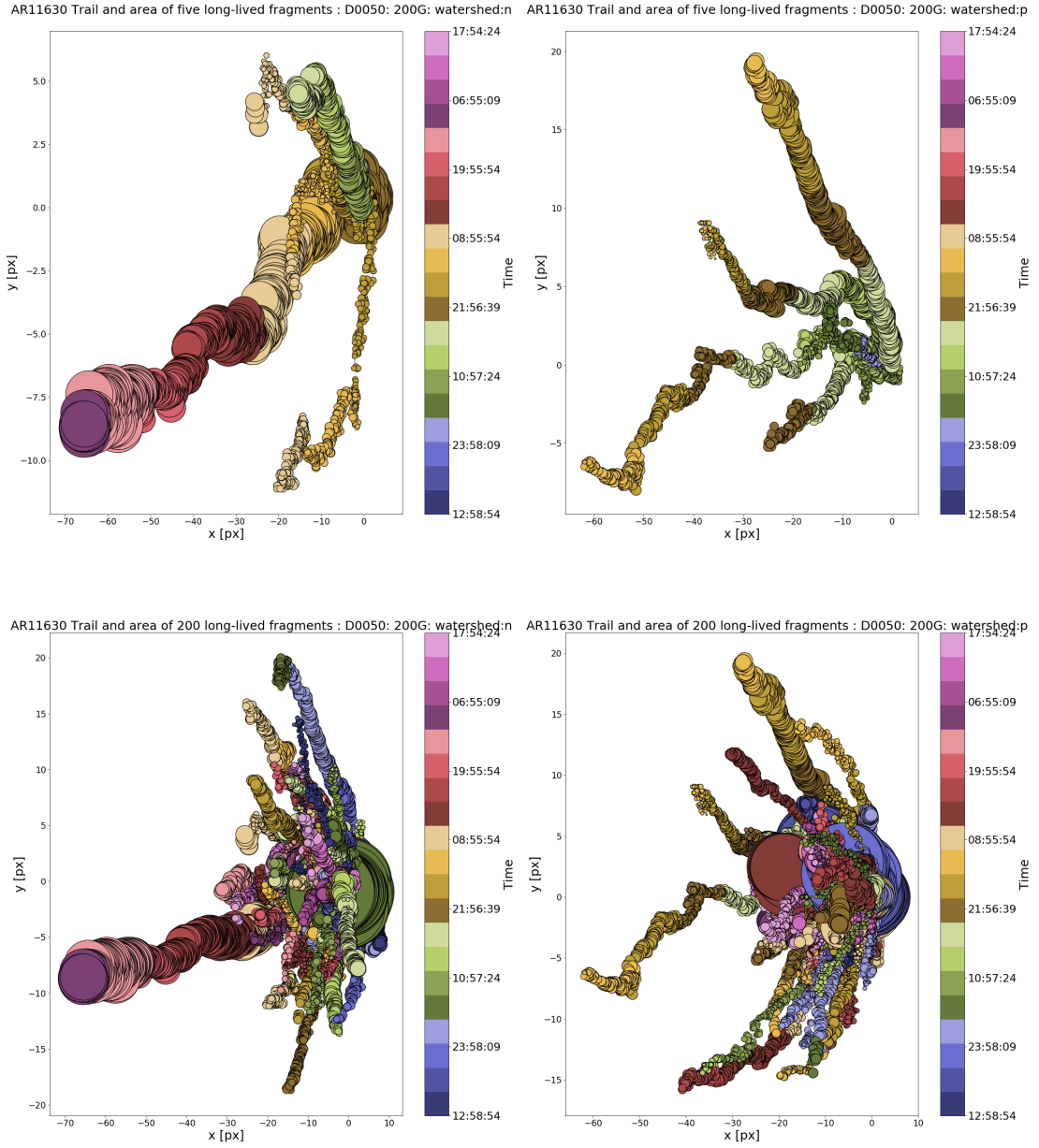

Figure 6.9: Timeseries of the x and y position (in pixels) of the geometric centroid of the 5 (top row) and 200 (bottom row) fragments that were tracked for the longest time during the observation. The position given is relative to the position the fragment was first detected. A magnetic field threshold of |200|G has been applied. The colour of the bullets changes with time from blue to red and their size indicates the surface area of the fragment, in pixels. Shown are the result for the watershed method for the negative (left column) and positive fragments (right column).

Table 6.4: RHESSI flares for region AR 11819.

GOES class	Start time	Peak time	End time
B1.7	14/08/2013 03:15	14/08/2013 03:22	14/08/2013 03:35
A5.0	14/08/2013 03:35	14/08/2013 03:37	14/08/2013 03:43
A2.0	14/08/2013 03:50	14/08/2013 03:52	14/08/2013 03:57
A8.9	14/08/2013 04:02	14/08/2013 04:07	14/08/2013 04:07
B1.4	14/08/2013 08:25	14/08/2013 08:34	14/08/2013 08:36
A2.6	14/08/2013 08:48	14/08/2013 08:52	14/08/2013 08:54

position of first detection, and for both polarities they are moving in the same leftwards (eastern) direction. The long lasting positive fragments seem to be more concentrated during the earlier times (green in left panel of Figure 6.9) before later spreading out further (yellow symbols). They also spread out further than the negative fragments, with the longest lasting negative fragments appearing later in the time range.

6.2.2 AR 11819

AR 11819 emerged while still on the back side of the Sun. The region formed fully only when rotated around to Earth view, satisfying our selection criteria. It appeared on the South Eastern part of the Sun about 10 August 2013 07:30 UTC and formed as region on 11 August 2013 08:30 UTC. Our analysis lasted over a the time period from 13 August 2013 20:58:23 until 14 August 2013 15:59:08 UTC. The region at the beginning of the analysis is fairly central at longitude about -180 arcsecs. This is a small region, situated between two larger ones and by the end of the analysis its positive field starts merging with the neighbouring region. The submaps were carefully selected in a way to omit any field belonging to other regions. After inspecting individually the location of the last four from the ten microflares initially reported by RHESSI in AIA maps, we determined they did not originated from AR 11819. Table 6.4 shows a list of the 6 RHESSI flares that were determined to take place in the region.

Figure 6.10 presents the HMI maps on 720s data with the contours of RHESSI image overplotted (pink), cyan for negative and yellow for positive polarities the

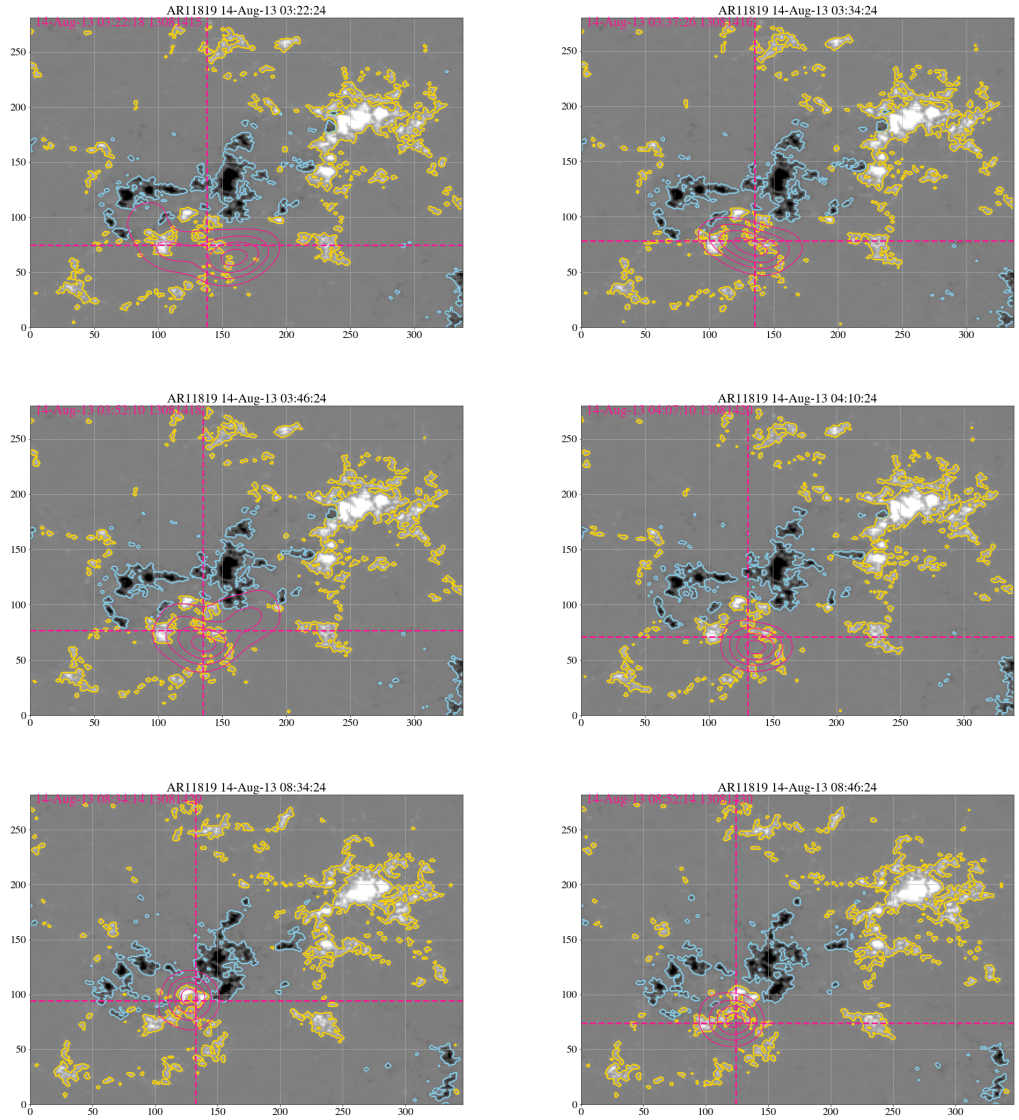

Figure 6.10: HMI submaps of region AR 11819, with pink contours overplotted indicating the RHESSI flare loops. With coloured text the peak time of the flare. The contours indicate the fragments identified by the Watershed fragmentation (positive: yellow, negative: cyan).

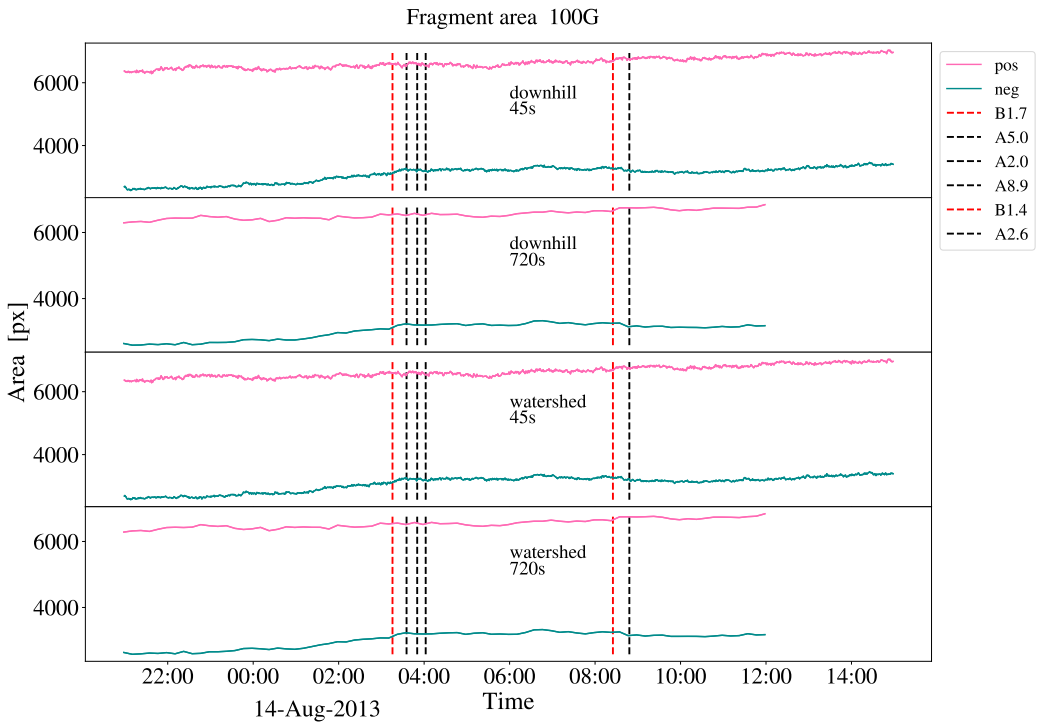

Figure 6.11: Total area from all fragments for region AR11819, using downhill fragmentation (top two panels) and watershed fragmentation method (bottom two panels), with magnetic field threshold of $100G$. The green plot is for the negative fragments and the pink for the positives. The vertical dashed lines indicate the start time of the RHESSI flares (black: A, red: B, purple: C-class).

contours of the fragments returned by the watershed algorithm. Some of the flares mainly happened around the Polarity Inversion Line, as expected but some seem deeply rooted at the positive fragments. This is due to the fact that the positive field reconnected with field from other regions. The flares happened primarily around small concentrations of flux, with the exception of the last two which are centred around large positive fragments. As a result, it is logical to expect more intense changes in the positive field than in the negative.

6.2.2.1 Time profiles of field changes

For this active region we focus more on the 45s time profiles, but also include the 720s for the sake of comparison in the initial figures. Although note that the 720s data covers a shorter time range than the fuller 45s analysis.

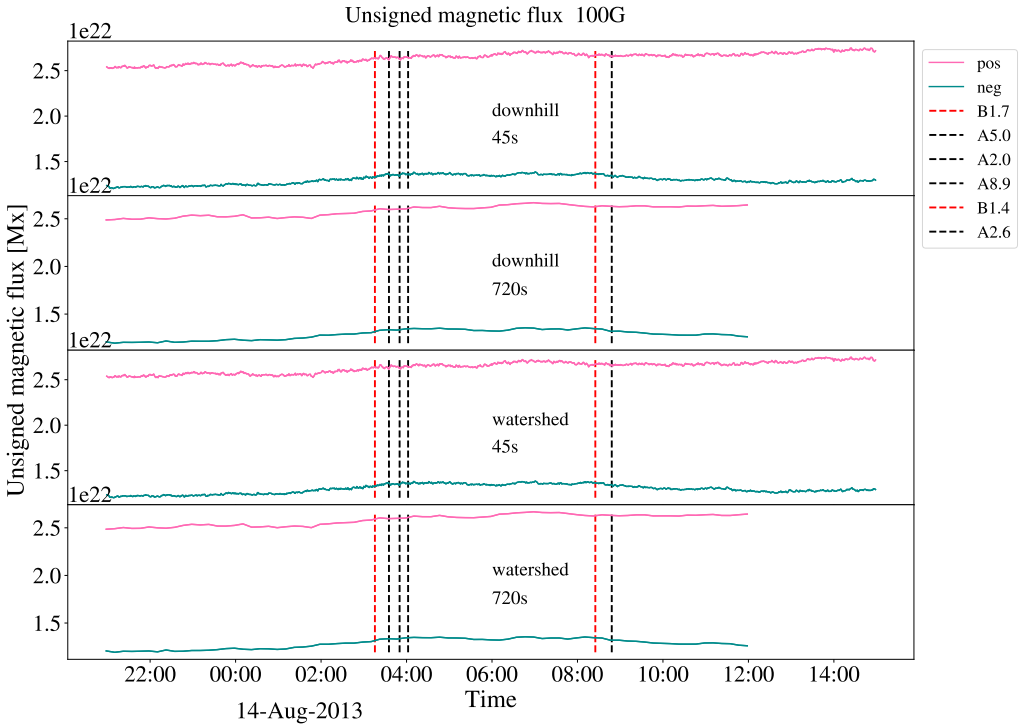

Figure 6.12: Total unsigned flux from all fragments for region AR11819, using downhill fragmentation (top two panels) and watershed fragmentation method (bottom two panels), with magnetic field threshold of $100G$. Green line is for negative fragments and pink for positives. The vertical dashed lines indicate the start time of the RHESSI flares (black: A, red: B, purple: C-class).

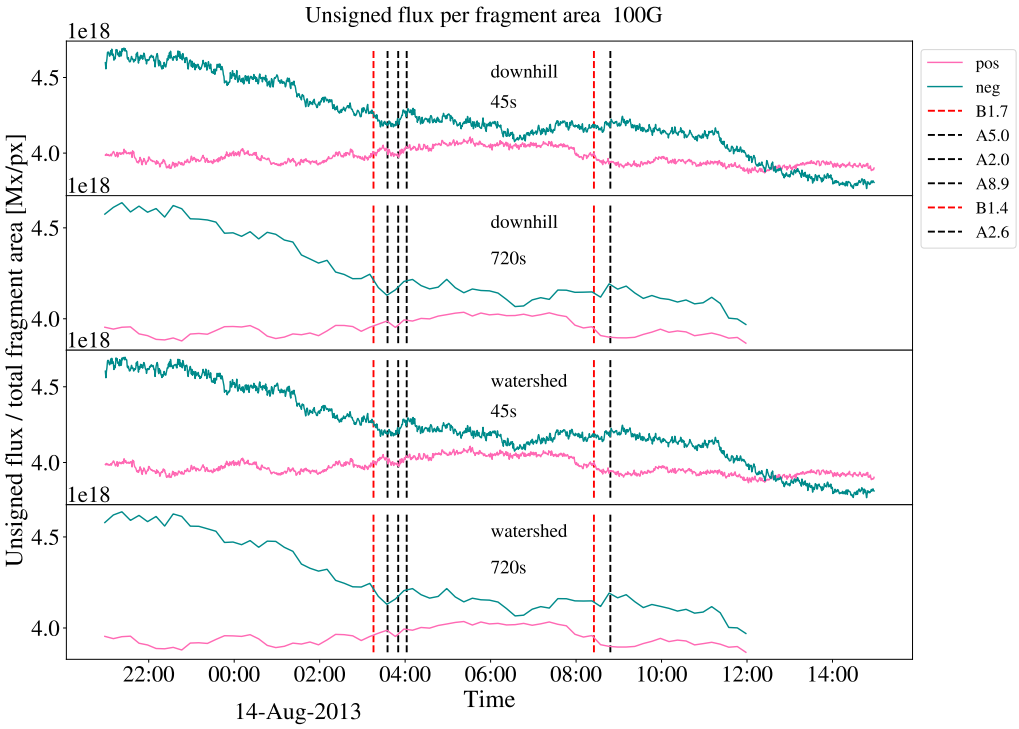

Figure 6.13: Average flux per fragment area for region AR11819, using downhill fragmentation (top two panels) and watershed fragmentation method (bottom two panels). A magnetic field threshold of $100G$ was applied. Green line is for negative fragments and pink for positives. The vertical dashed lines indicate the start time of the RHESSI flares (black: A, red: B, purple: C-class).

In Figures 6.11-6.12 the profile of total fragment area and flux appear to be generally flat and unaffected by the flares, even though there were two B-class flares originating from this region. An exception to the flat profile can be seen as a small decrease in the total area and a small increase in the total flux of positive fragments before the start time of the second flare on 03:35UT. There is no consistent behaviour in the change of those properties associated with any class of microflares.

In Figure 6.13 the profile of the average unsigned flux per unit area shows more interesting behaviour. At the beginning of the observation it is decreasing for negative but slightly increasing for positive. B1.7 microflare occurs at 03:15UT followed by a slightly positive gradient on the average flux profile about that time, Around the time of the second flare (A5.0 03:55) the profile is flat and unchanged.

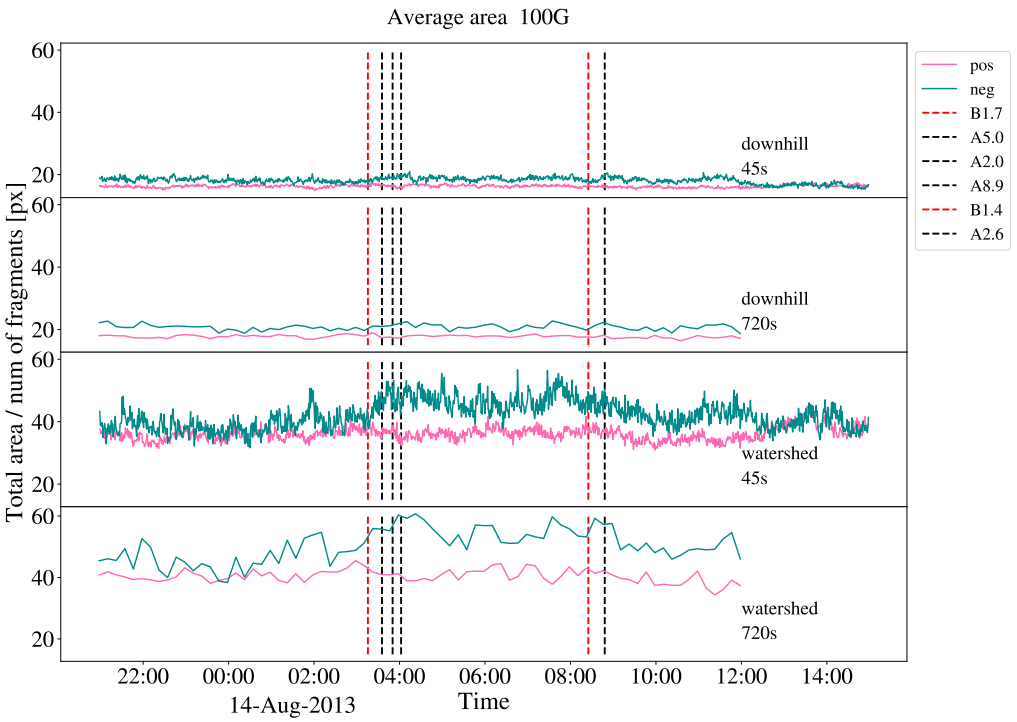

Figure 6.14: Average area per fragment for region AR11819, using downhill fragmentation (top two panels) and watershed fragmentation method (bottom two panels), with magnetic field threshold of 100G. Green line is for negative fragments and pink for positives. The vertical dashed lines indicate the start time of the RHESSI flares (black: A, red: B, purple: C-class).

The third flare (A2.0 03:50UT) starts with slightly positive gradient both for the negative and positive flux. Again, these changes are very small and we cannot omit the possibility that they are coincidences. At the same time, viewing movies of the region, there was no significant merging or splitting for that time but there is reconnection with nearby regions. Therefore, we could be seeing the effect of cancellation from those interactions. The last two flares (B1.4 08:34 and A2.6 08:52) are not accompanied by any change in the time profile in Figure 6.13. The plot of average flux per area shows that emergence occurred after the flares started taking place, probably as a result of increased shearing due to the dynamic nature of the region.

Figures 6.14 and 6.15 show the profiles of area per number of fragments and flux per number of fragments. For the positive fragments there is a flat profile.

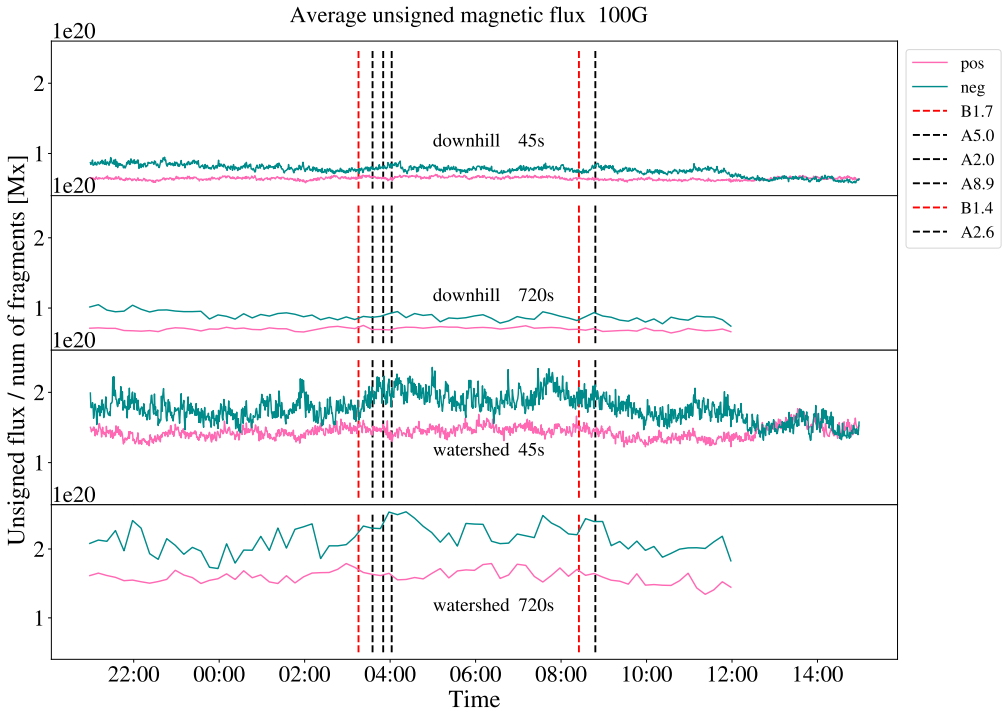

Figure 6.15: Average unsigned flux per fragment for region AR11819, using downhill fragmentation (top two panels) and watershed fragmentation method (bottom two panels), with magnetic field threshold of $100G$. The green plot is for the negative fragments and the pink for the positives. The vertical dashed lines indicate the start time of the RHESSI flares (black: A, red: B, purple: C-class).

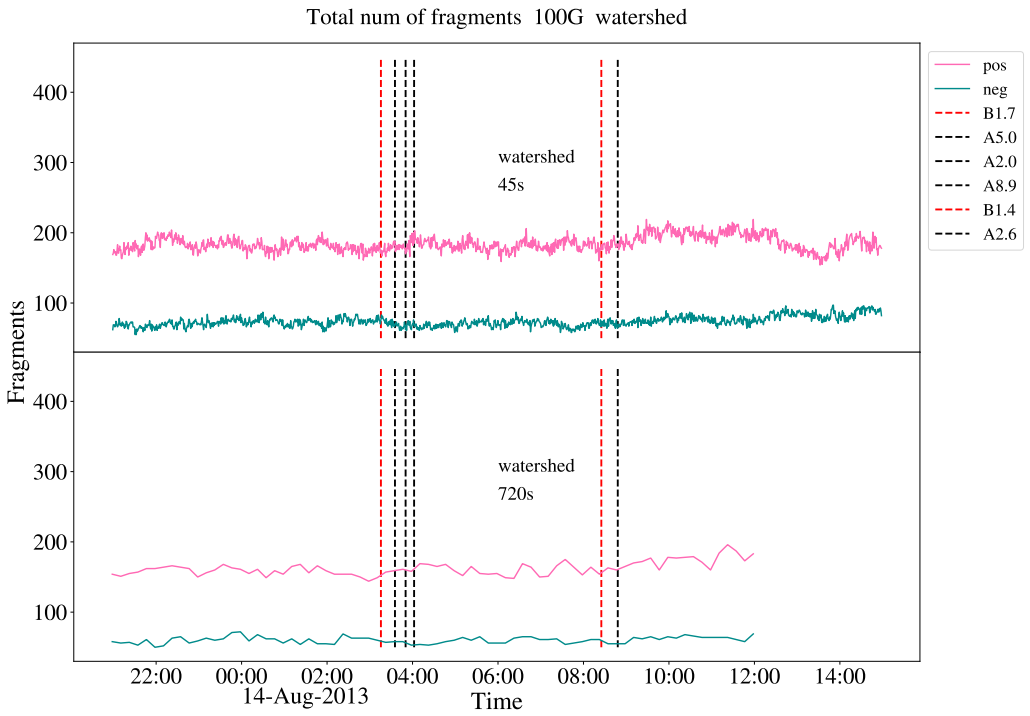

Figure 6.16: Timeseries of the total number of fragments for region AR11819, using watershed fragmentation and magnetic field threshold $\geq |100G|$. The green plot is for the negative fragments and the pink for the positives. The vertical dashed lines indicate the start time of the RHESSI flares (black: A, red: B, purple: C-class).

For the negative, there is a peak at 02:00UT. That was caused by merging of two large fragments. The general profile of the average area and flux for the negative fragments is increasing. Looking at the position of the flare loops in Figure 6.10, they where mainly rooted on the positive fragments. As explained at the beginning of Section 6.2.2, the positive field re-connected with negative field from a nearby region. This implies that the merging of negative fragments from AR 11819 continued uninterrupted while the positive fragments cancelled out with negative field of the other regions. It also means it is unclear whether the properties of negative fragments were associated with the flares at all. The flares did cause a dip in the average area and flux of the positive fragments at 04:00UT, consistent with cancellation. The last two flares had no impact in either polarities.

Figures 6.16-6.17 show the total number of fragments and number of new

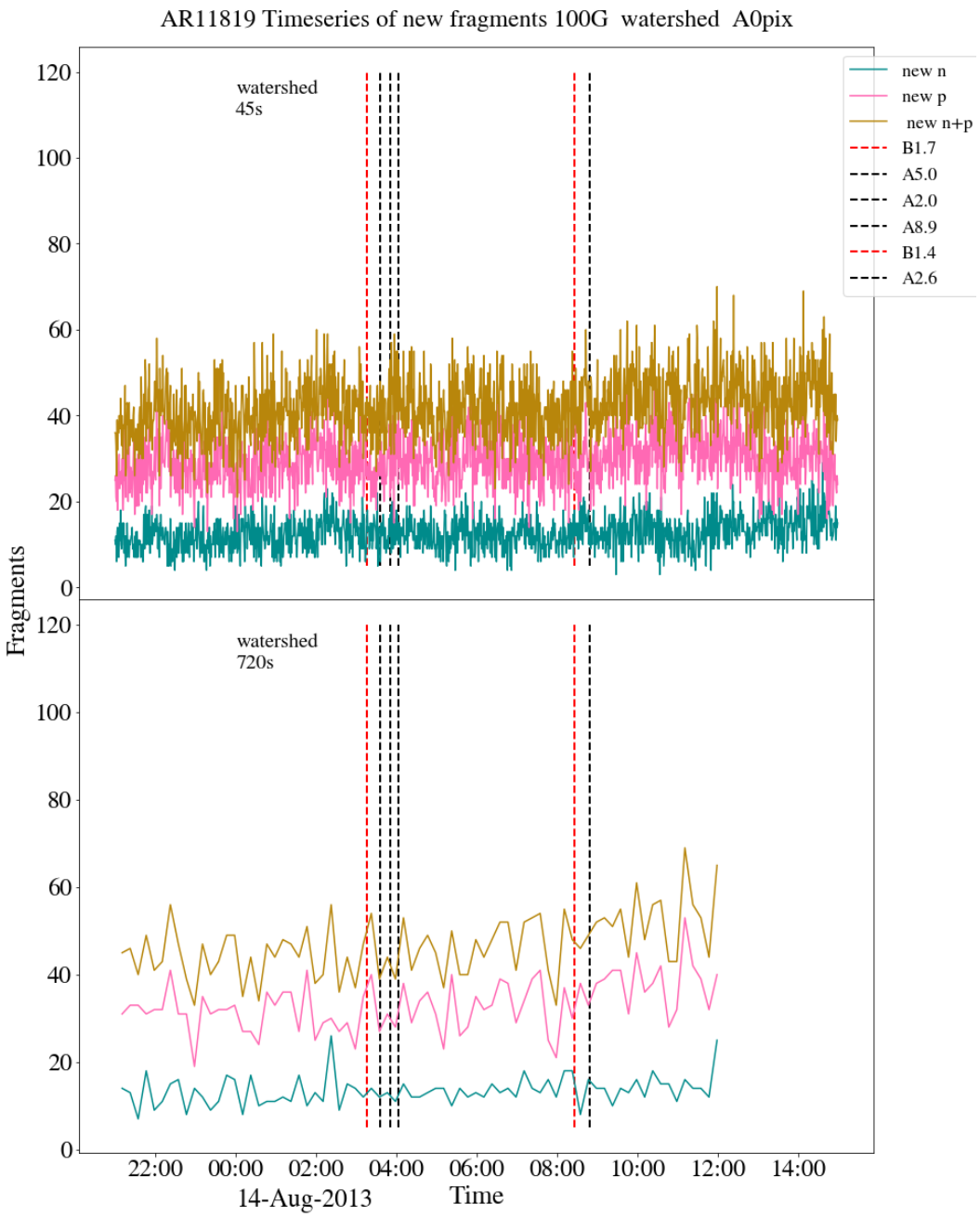

Figure 6.17: Number of new fragments appearing for region AR11819. With cyan are shown the number of new negatives fragments. With pink are shown the number of new positive fragments. With golden are shown the number of all new fragments. The vertical dashed lines indicate the start time of the RHESSI flares (black: A, red: B, purple: C-class).

fragments. The number of fragments shows that the rate of fragmentation was steady, with a slight increase for positives after the continuous burst of the first four flares. It is likely that this was indeed connected with the flaring process, as the release of energy re-organises the field. The number of new fragments in Figure 6.17 shows no clear relation between the bulk properties and the microflares.

This region does not give a specific trend between the properties and the flaring times, but indicates emergence before flares occurred.

6.2.2.2 Spatial evolution of fragments

The movement of the 5 and 200 longest lived fragments for this region, can be seen in Figure 6.18, where it shows a clear difference to those of region AR 11630. For the five longest-lived fragments (Figure 6.18, top row), for the negative fragments, there are trails moving both towards East and West. Instead, the positive fragments seem more organised, with four out of five fragments moving uniformly towards Sun West while one staying at the same longitudes. However, the plot of 200 fragments (Figure 6.18, bottom row) shows a slight preference of the negative towards Sun East, although not thoroughly organised. The positive fragments seem to mainly stay on location of first detection and secondarily have no preferential direction. The average lifetime of the fragments timetracked in top row is 8.3 hours. In bottom, the fragments existed from 1.7 to 8.9 hours.

6.2.3 AR 12234

AR 12334 emerged on 10-December-2014 16:00:00 UTC at about -360 arcsecs. Our analysis covers the time period from 10-Dec-2014 16:28:54 to 12-Dec-2014 16:28:09. During this time, the region moves from the Eastern part (10-Dec), to Sun centre (11-Dec), to Western (12-Dec), so a change in the LoS component should be taken into account. It was a smaller region compared to the other two selected, with a larger region close by. Its positive field becomes spread out as it evolves with time while the negative remains concentrated. It exhibited a series of continuous microflares, detailed in Table 6.5.

Figure 6.19 presents the HMI map on 720s data with the contours of the RHESSI images overplotted (in pink). With cyan for negative and yellow for

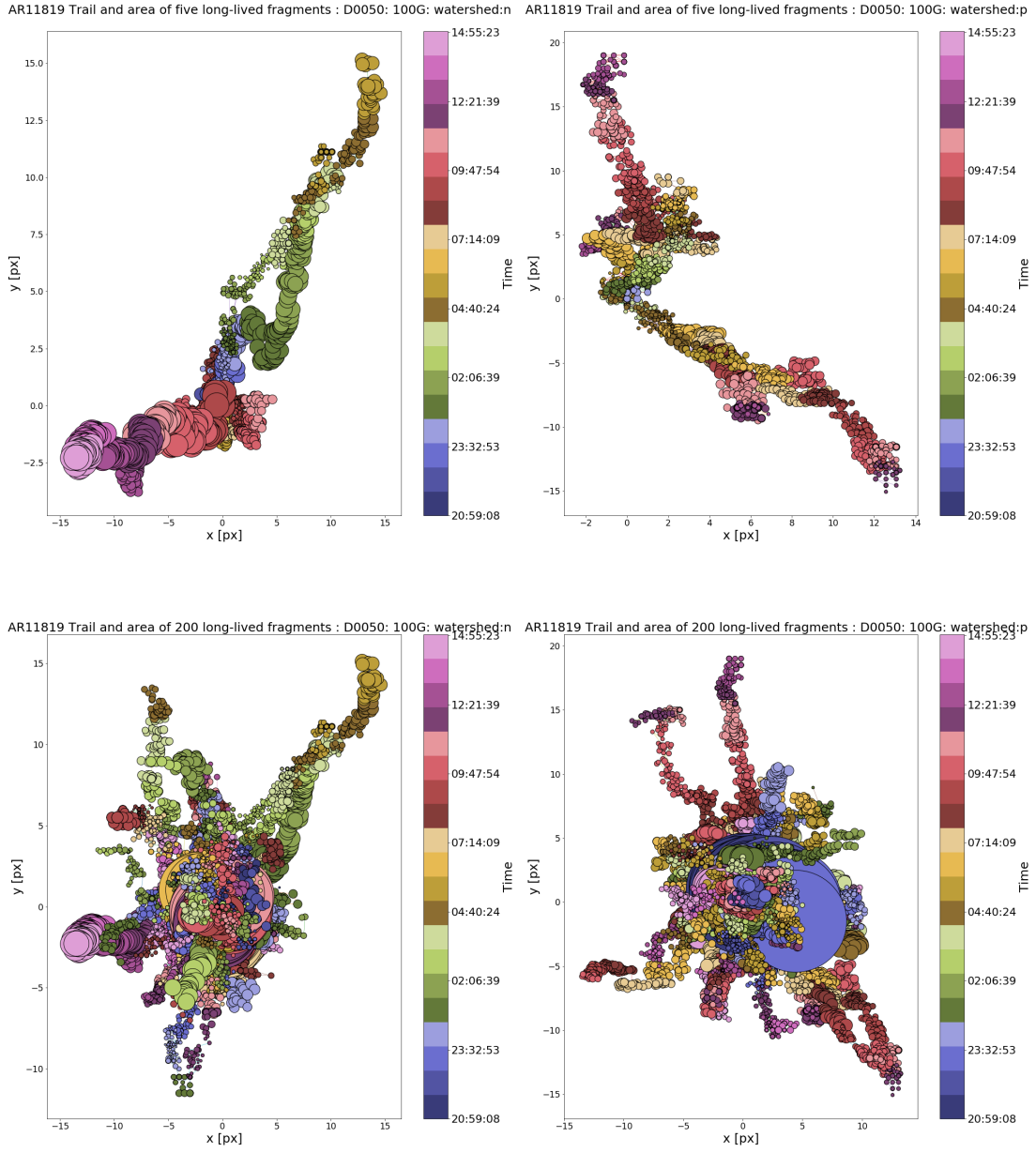

Figure 6.18: Timeseries of the x and y position (in pixels) of the geometric centroid of the 5 (top row) and 200 (bottom row) fragments that were tracked for the longest time during the observation. The position given is relative to the position the fragment was first detected. A magnetic field threshold of |100|G has been applied. The colour of the bullets changes with time from blue to red and their size indicates the surface area of the fragment, in pixels. Shown are the result for the watershed method for the negative (left column) and positive fragments (right column).

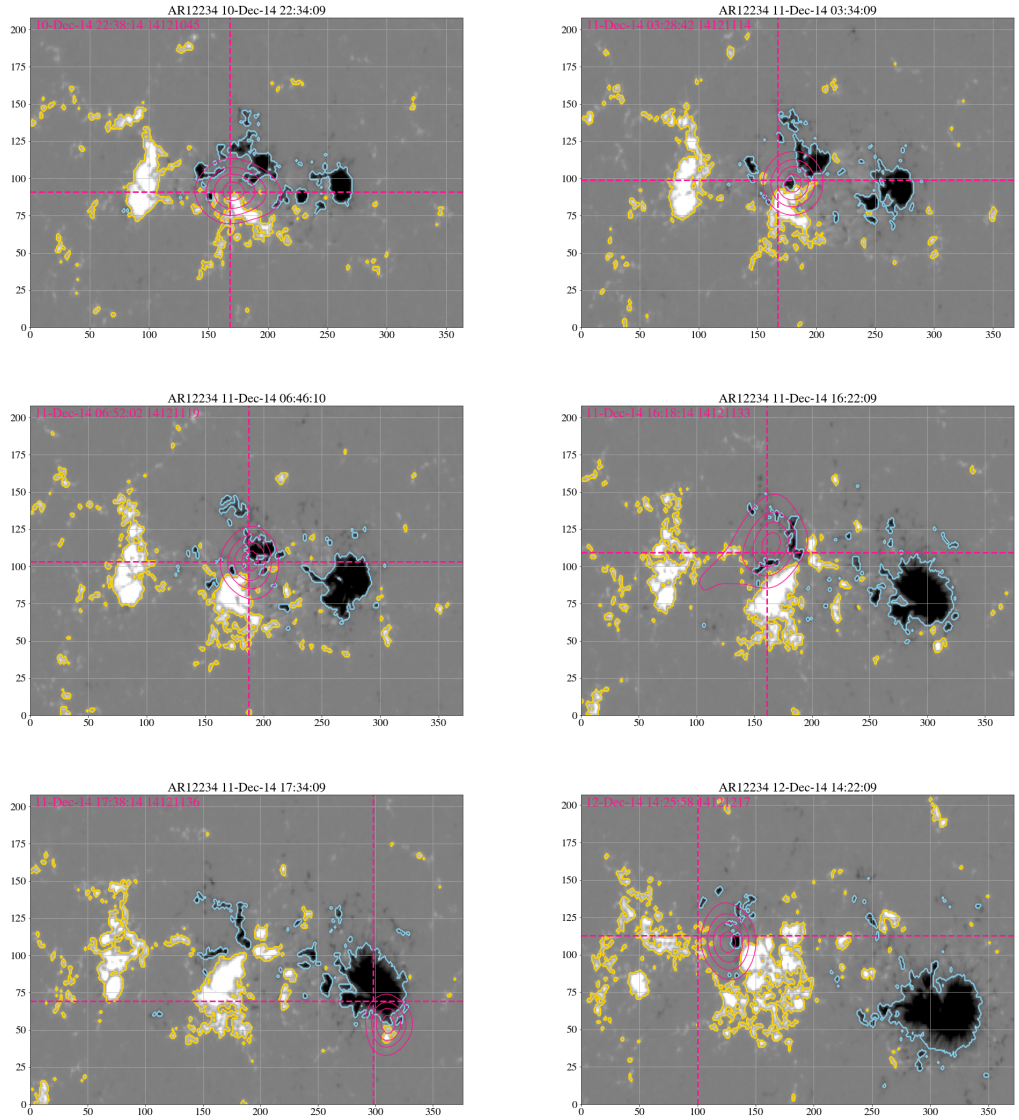

Figure 6.19: HMI submaps of region AR 12234, with pink contours overplotted indicating the RHESSI flare loops. The contours indicate the fragments identified by the Watershed fragmentation (positive: yellow, negative: cyan). With coloured text the peak time of the flare.

Table 6.5: RHESSI flares for region AR 12234.

GOES class	Start time	Peak time	End time
B3.2	10/12/2014 22:27	10/12/2014 22:38	10/12/2014 22:53
B5.8	11/12/2014 03:25	11/12/2014 03:28	11/12/2014 03:33
A1.8	11/12/2014 06:51	11/12/2014 06:52	11/12/2014 06:53
A3.9	11/12/2014 07:01	11/12/2014 07:04	11/12/2014 07:12
C1.1	11/12/2014 08:48	11/12/2014 08:52	11/12/2014 08:53
A4.9	11/12/2014 16:16	11/12/2014 16:18	11/12/2014 16:19
A1.5	11/12/2014 17:37	11/12/2014 17:38	11/12/2014 17:38
A4.6	12/12/2014 14:23	12/12/2014 14:25	12/12/2014 14:28
A3.4	12/12/2014 14:28	12/12/2014 14:33	12/12/2014 14:35
C3.4	12/12/2014 14:35	12/12/2014 14:40	12/12/2014 14:48

positive the contours of the fragments returned by the watershed algorithm are given. As with the previous regions, the flares mainly happened around the Polarity Inversion Line and are primarily associated with small and secondarily with larger concentrations of flux. There are fragments of both polarities around the RHESSI microflare contours, with possibly slightly more negative fragments. We would expect field changes in both polarities.

6.2.3.1 Time profiles of field changes

As can be seen in Figure 6.20 the fragment area has a general steady increase with time for both polarities, which at least partly can be attributed to the increase of the LoS component. It has not been affected by the occurrence of flares as there are no clear changes about the times of the microflares. There is a small dip in the area profile for positive fragments after the two A-class flares on 11-Dec-2014 07:01, since it is the only change happening in close proximity to a flare start time. However, that behaviour is very similar to the general behaviour of the plot and could be just noise.

In Figure 6.21 the time profile of the total unsigned flux shows the negative flux gradually increasing for the whole time considered but the positive only increases until about 12-Dec-2014 03:00UT. This was not a geometrical effect as the region

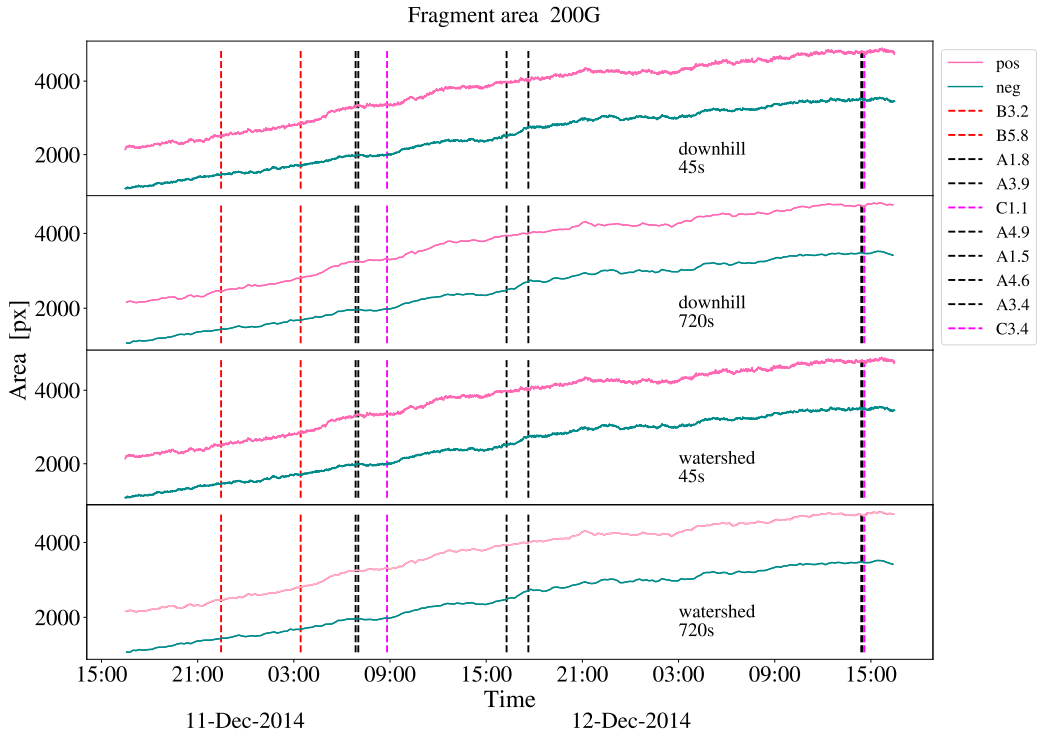

Figure 6.20: Total area from all fragments for region AR12234, using downhill fragmentation (top two panels) and watershed fragmentation method (bottom two panels),with magnetic field threshold of 200G. Green line is for negative fragments pink for positives. The vertical dashed lines indicate the start time of the RHESSI flares, where black refers to A-class , red to B-class and purple to C-class flares.

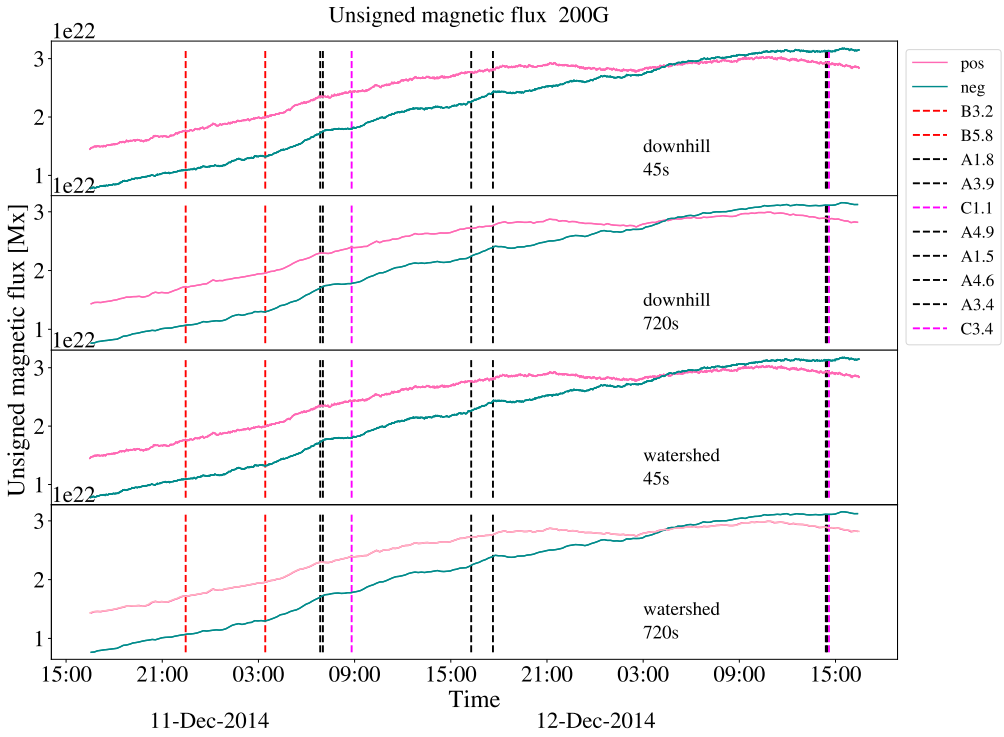

Figure 6.21: Total unsigned flux from all fragments for region AR12234, using downhill fragmentation (top two panels) and watershed fragmentation method (bottom two panels), with magnetic field threshold of 200G. Green line is for negative fragments and pink for positives. The vertical dashed lines indicate the start time of the RHESSI flares (black: A, red: B, purple: C-class).

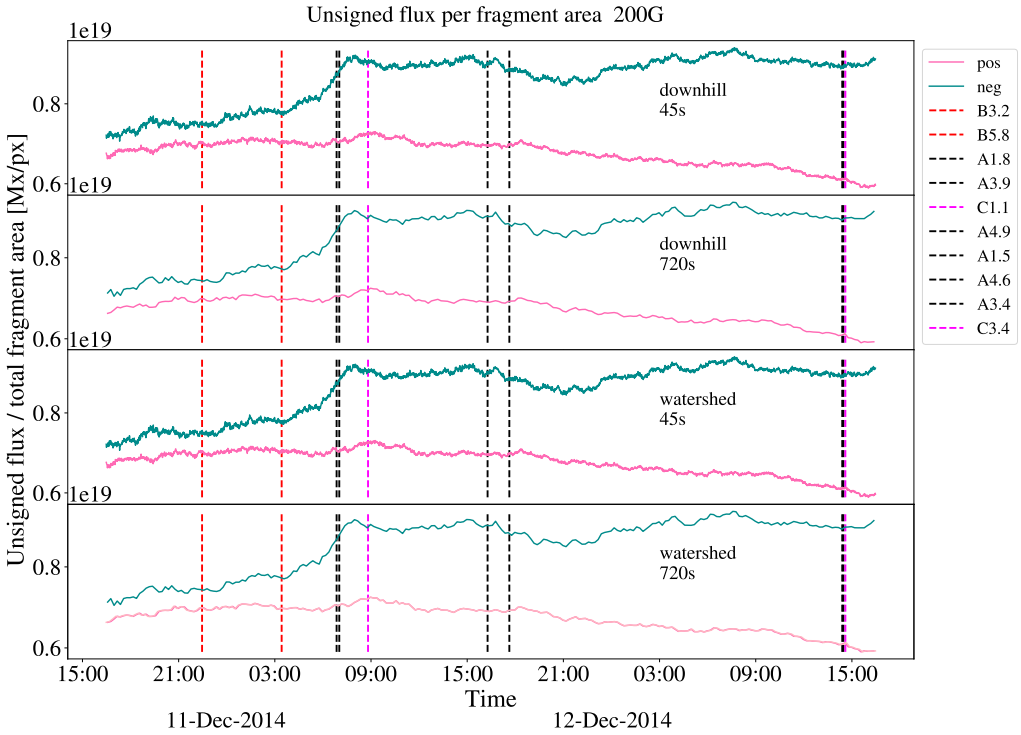

Figure 6.22: Average flux per fragment area for region AR12234, using downhill fragmentation (top two panels) and watershed fragmentation method (bottom two panels), with magnetic field threshold of 200G. Green line is for negative fragments and pink for positives. The vertical dashed lines indicate the start time of the RHESSI flares (black: A, red: B, purple: C-class).

was still at a central location. It might be implying that the positive field spread out so much that, overall, it dropped below the B_{LOS} threshold. Also for the total fragment flux, no particular change can be seen before or after the flares.

Moving on to the average flux per area, Figure 6.22, the negative fragments show a steady increase throughout the time range, indicating emergence. The large increase on 11-Dec-2014 05:00UT is caused by the merging of two big fragments. The negative fragments have substantially more flux per area compared to the positive, a behaviour to be expected when seeing how concentrated the negative flux has been compared to the positive in the maps of Figure 6.19 . Another factor leading to this discrepancy is that there were a lot of small positive

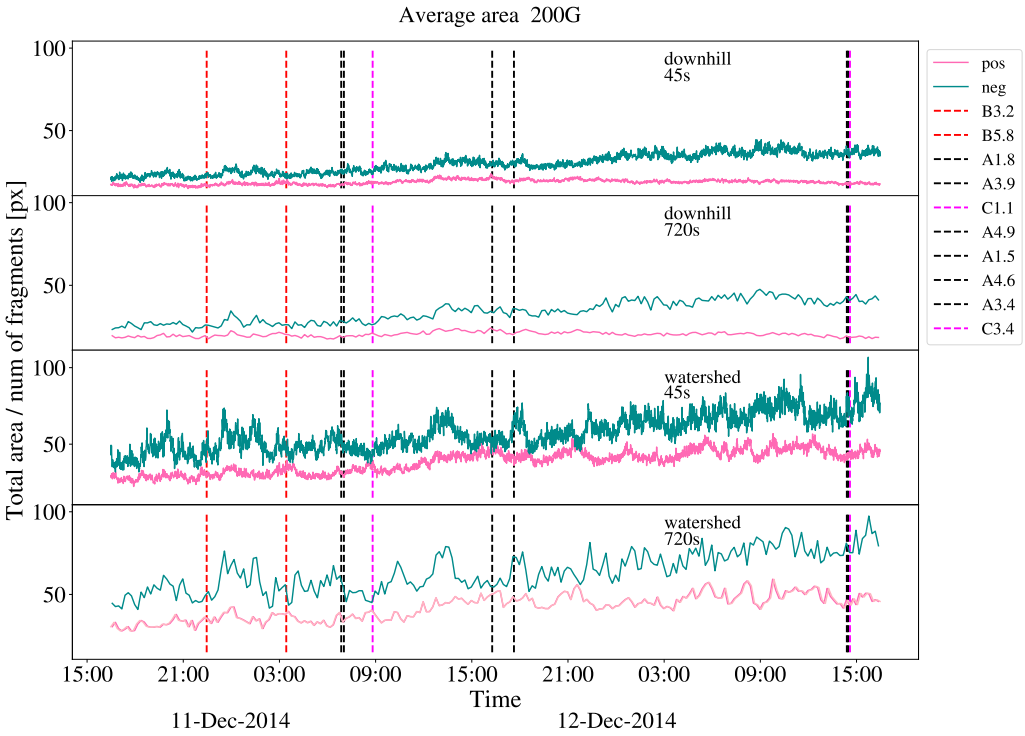

Figure 6.23: Average area per fragment for region AR12234, using downhill fragmentation (top two panels) and watershed fragmentation method (bottom two panels), with magnetic field threshold of $200G$. Green line is for negative fragments and pink for positives. The vertical dashed lines indicate the start time of the RHESSI flares (black: A, red: B, purple: C-class).

fragments that satisfied the B_{LOS} threshold, while the small negative fragments were weaker and so not tracked (that does not contradict Figure 6.21 suggests that positive fragments overall -and not individually- had lower flux than negative). For the negative, no consistent changes are detected before any class of flares. For the positive fragments there is a pattern of increase-A flares, decrease-A flare-increase on 03:50UT in the flux per area, but this is not repeated for the subsequent A class flares.

Figures 6.23-6.24 show the average fragment area and average unsigned flux per fragment. These show a generally steady value for the positive fragments but slightly more increasing for negative.

Region AR 12234 has not shown any trends of interest for the bulk properties.

Figures 6.25-6.26 shows the total number of fragments and new fragments.

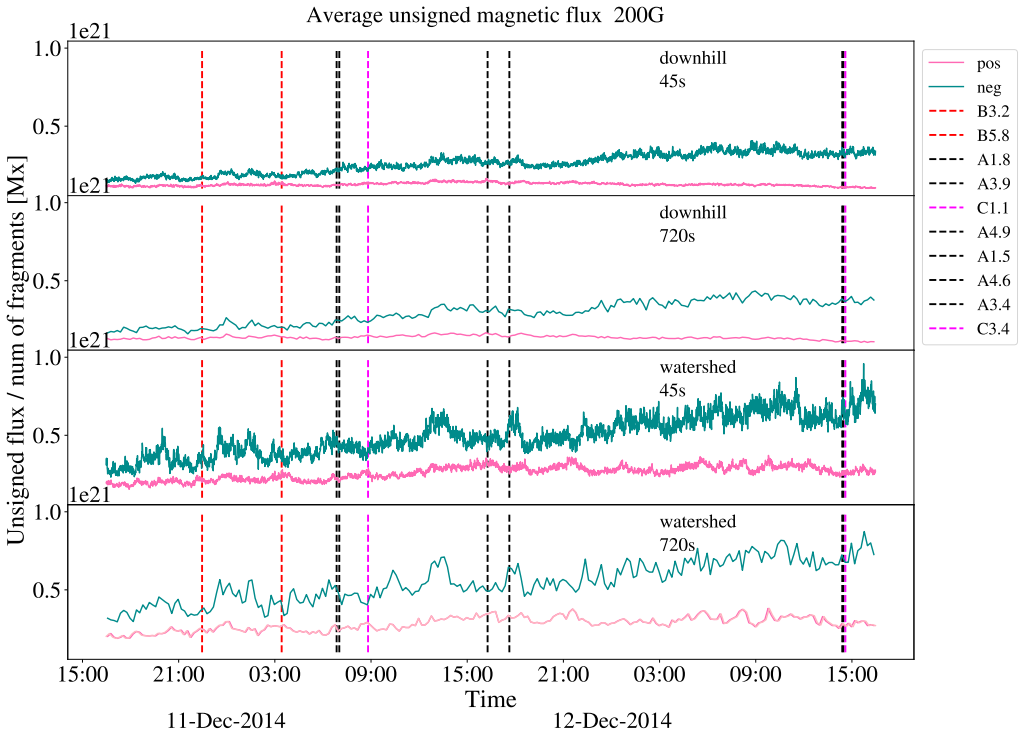

Figure 6.24: Average unsigned flux per fragment for region AR12234, using downhill fragmentation (top two panels) and watershed fragmentation method (bottom two panels), with magnetic field threshold of $200G$. Green line is for negative fragments and pink for positives. The vertical dashed lines indicate the start time of the RHESSI flares (black: A, red: B, purple: C-class).

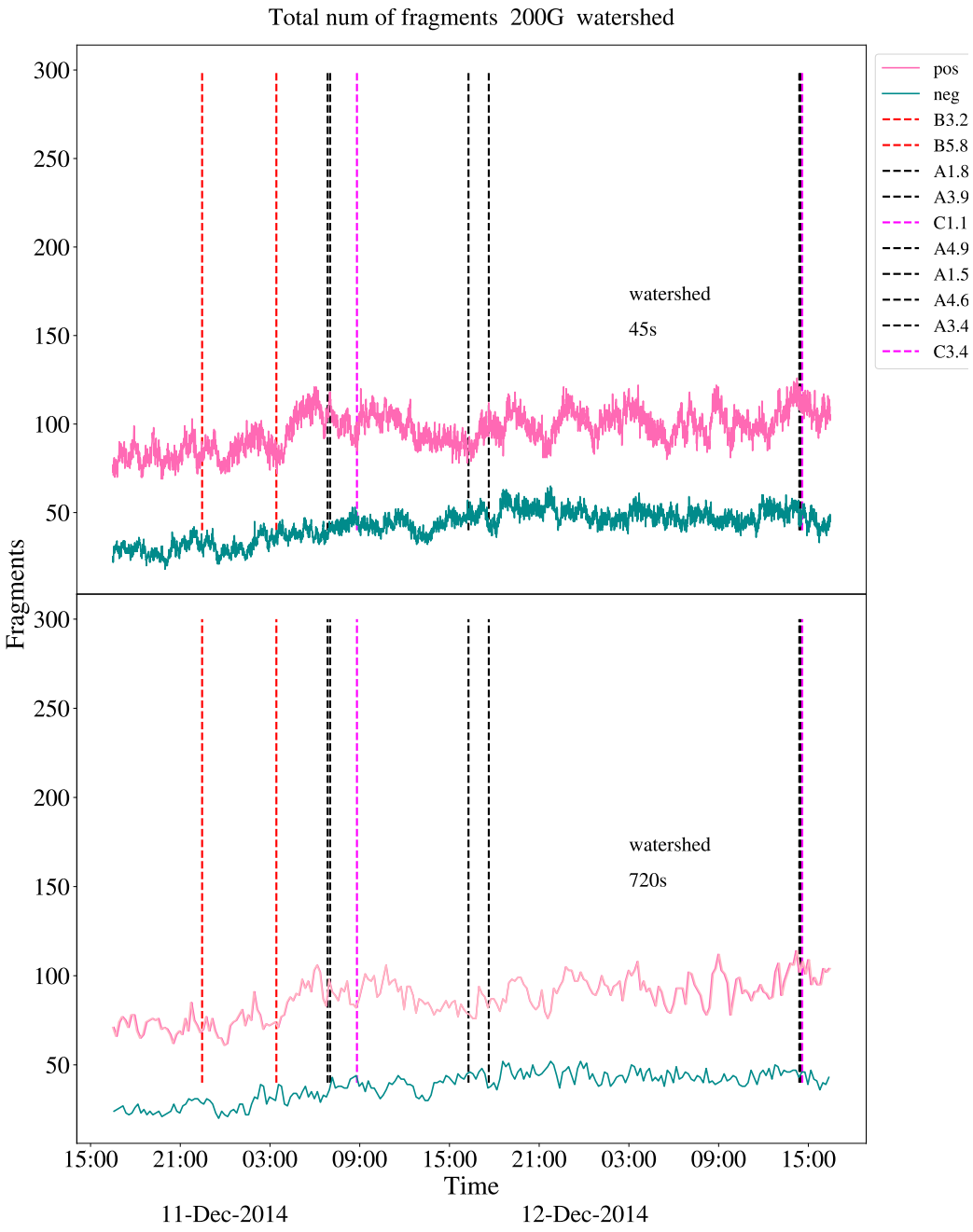

Figure 6.25: Total number of fragments for region AR12234, using watershed fragmentation and magnetic field threshold $\geq |200G|$. The green plot is for the negative fragments and the pink for the positives. The vertical dashed lines indicate the start time of the RHESSI flares (black: A, red: B, purple: C-class).

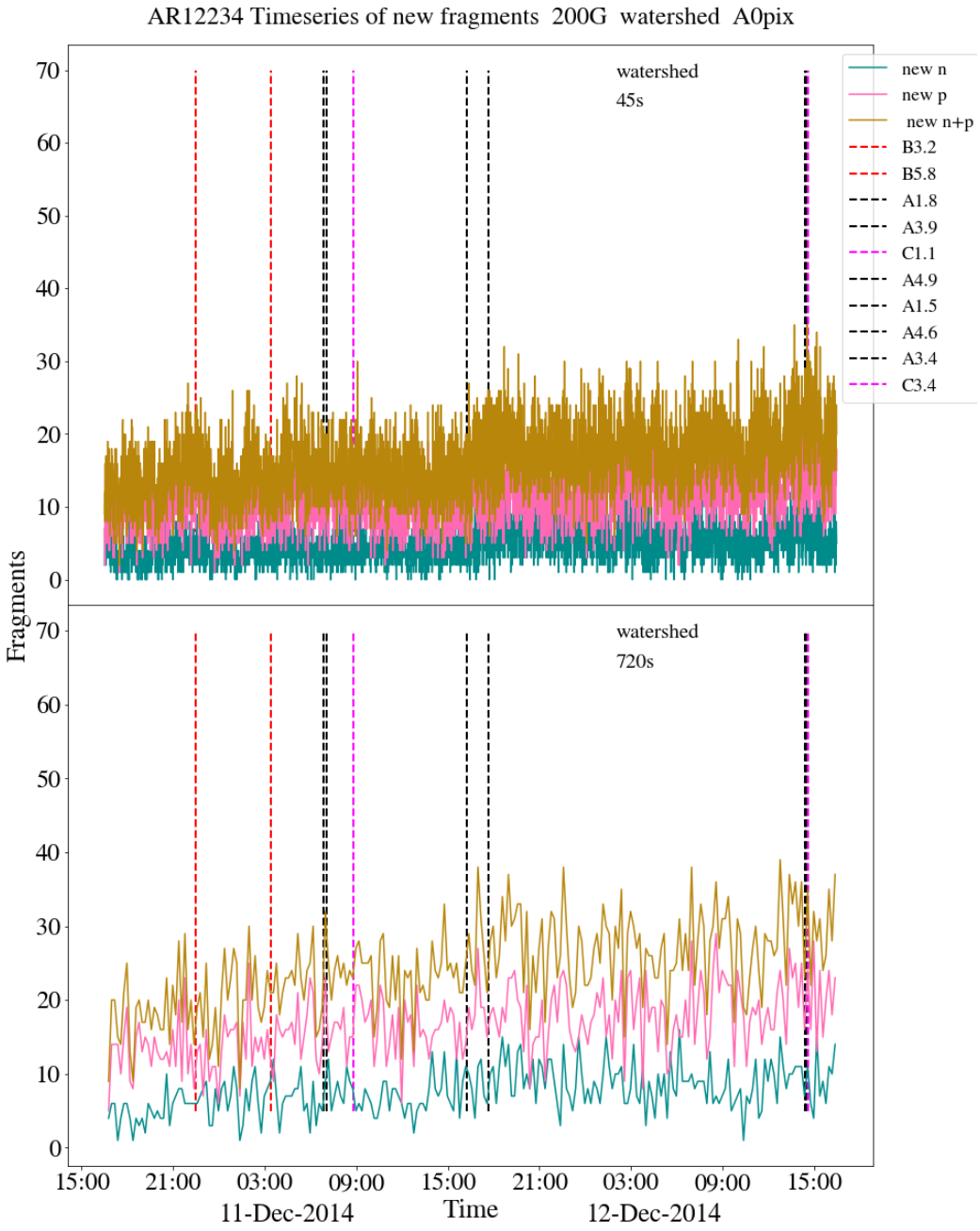

Figure 6.26: Number of new fragments appearing for region AR12234. With cyan are shown the number of new negatives fragments. With pink are shown the number of new positive fragments. With golden are shown the number of all new fragments. A magnetic field threshold of 200G was applied. The vertical dashed lines indicate the start time of the RHESSI flares (black: A, red: B, purple: C-class).

Although a variety of features occur in these time profiles there does not seem to be a consistent behaviour about the time of the microflare.

6.2.3.2 Spatial evolution of fragments

Figure 6.27 shows the movement of AR 12234 five longest-lived fragments (top row) and 200 longest-lived fragments (bottom row).The average lifetime of fragments in the top row was 13.5 hours, while for the 200 fragments it ranges from 2.5 to 13.8 hours. At the beginning of the observation, fragments of both polarities wobble around the position of first detection. For the five-longest lived fragments, as the time progresses the negative and positive fragments tend to go in opposite x directions, as they did at the beginning of observation for AR 11819 (Figure 6.18). The negative field in AR 12234 is highly concentrated while the positive spreads out. This is conformed also when looking at the plots for the 200 fragments, where the trail of the positive fragments is clearly spread out.

6.3 Summary and Conclusions

In this Chapter we have applied our Python code to characterise and track fragments in the HMI magnetograms of 3 microflaring active regions. We have presented the bulk properties of the fragments as time profiles as well as spatial movement of some of the longest tracked fragments.

For the total fragment area, we found that with AR 11630, the area of positive fragments was increasing both before and after the start time of flares, while for the negative fragments the area showed more steady behaviour. Similarly for AR 11819, the area for positive fragments had small increases and decreases before the B-class flares and no change for the negative, even during the times of the larger microflares. For AR 12234 the total area of the positive fragments decreased about the time of 2 A-class flares and the negative showed no change.

For the total unsigned flux, AR 11630 showed an increase in the positive flux before some B and C-class flares. A-class flares were associated with the flux stopping to increase. With the negative flux there would be a decrease which was then followed by A-class flares. For AR 11819, for the positive field there was a B-class flare followed by flux increase. The negative field showed an increase

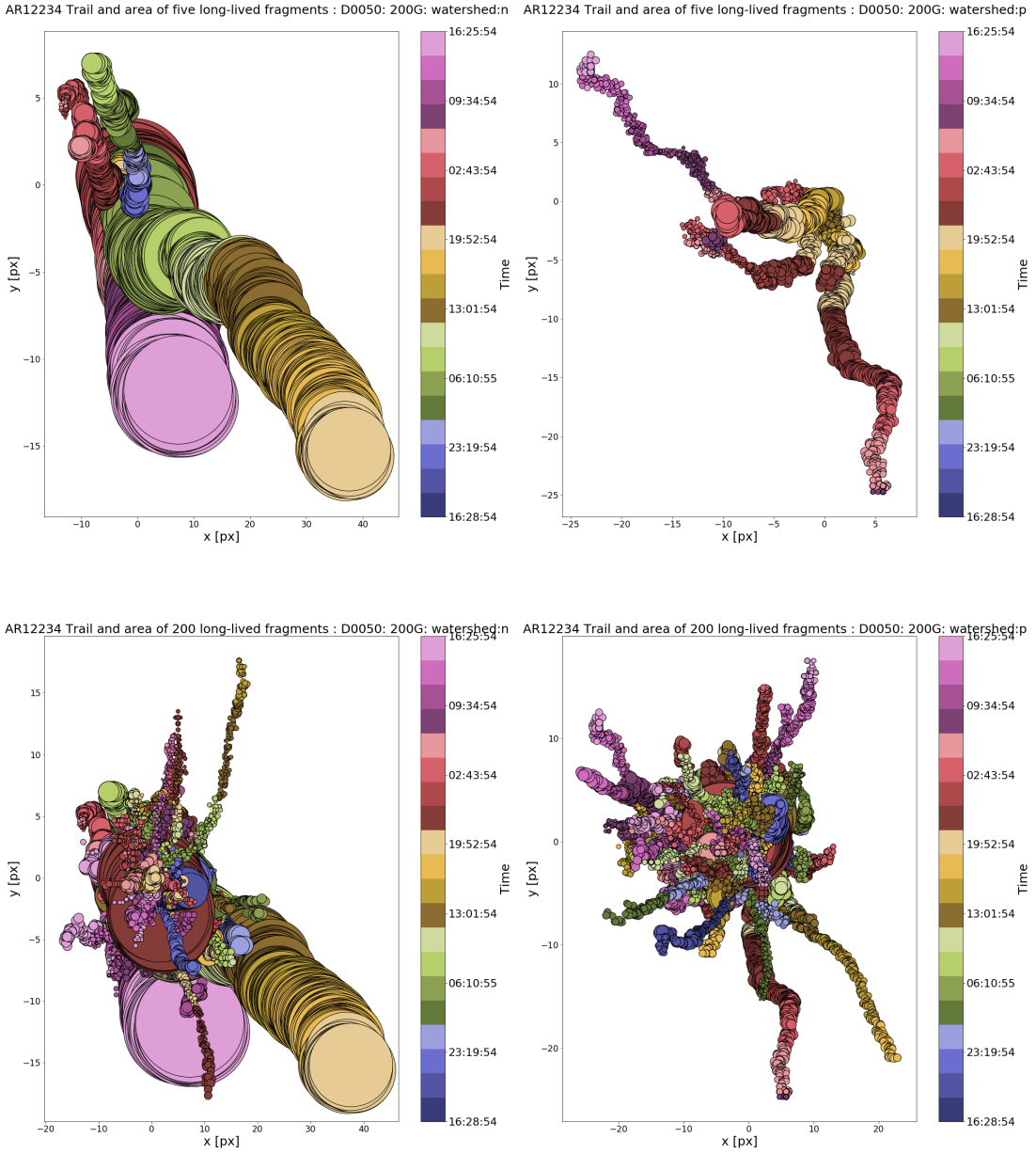

Figure 6.27: Timeseries of the x and y position (in pixels) of the geometric centroid of the 5 (top row) and 200 (bottom row) fragments that were tracked for the longest time during the observation. The position given is relative to the position the fragment was first detected. A magnetic field threshold of |200|G has been applied. The colour of the bullets changes with time from blue to red and their size indicates the surface area of the fragment, in pixels. Shown are the result for the watershed method for the negative (left column) and positive fragments (right column).

in flux and then there was an A-class flare. Finally, for AR 12234 there were no obvious changes in the time profile about the times of the microflares in both polarities.

As far as the average flux of fragments is concerned, AR 11630 showed that emergence starts before microflares and continues during the flaring times for the negative fragments, while there is no pattern arising for the positive fragments. Results from AR 11819 suggest that emergence occurred after the flares started taking place. For AR 12234, there were no consistent changes happening before any class of flares in the negative fragments. For the positives, there is an example of all combinations: increase, decrease and no change before A-class flares.

The average area and flux either were no impacted by flares, or seemed to cause flares or they simply showed the effects of merging, splitting and cancellation.

The plots of number of fragments and number of new fragments showed that fragments tend to split after flares, which is consistent with release of energy.

As a conclusion, more changes seemed to happen before flares than after their start time. For the positive fragments, we see an increase of total fragments area and flux before B and C-class flares while we observe a decrease before A-class flares. The negative fragments in most cases showed no changes at all. This could be due to the fact that in two of the regions the positive field reconnected with nearby regions as well.

Petrie & Sudol (2010) in a study of stepwise changes for mainly X class flares found that the changes of the positive field were twice as much as the changes in the negative. They also reported that the flux tends to decrease after flares. That was confirmed by Burtseva & Petrie (2013, study for M and X class flares) and satisfied the implosion scenario by Hudson et al. (2008). However, it was disputed by Castellanos Durán et al. (2018, study for C, M and X class flares) and it was contrary to the results from Watson (2012, study for X class flares). Another difference between Castellanos Durán et al. (2018) and Petrie & Sudol (2010) is that they do not find any dependance of the ΔB_{LOS} changes with the location of the flare on disk. Both of those studies find that small ΔB_{LOS} are more frequent than big changes, with Castellanos Durán et al. (2018) reporting that the frequency of a ΔB_{LOS} occurring falls exponentially with its strength.

In this study, none of the properties showed a consistent pattern in change

before or after flares, which was the science question we were focussing on.

Finally, the plots of spatial movement gave an indication of the general direction of the fragments per polarity. Interestingly for AR 11630 both polarities have a preferential direction towards Sun East. For AR 11819 and AR 12234, the negative field moves in all directions or towards Sun West, while the positive had no preferential direction. In the last two regions we saw the least number of changes in their field properties, but it is not clear if those two facts are connected.

The products of the pipeline presented in this thesis offer the possibility of additional future analysis. One of the properties we have calculated is the orientation angle of an ellipse that is being fitted to the fragment. A plot of this property would give an idea of the orientation of the field as time progresses and consequently of the structure of the magnetic loops forming the active region. We would expect a more complicated field to lead to more microflares, as there are increased changes of stressed field of opposite polarities, as well as it adds up to the helicity of the region.

The pipeline itself can be developed even further. If the feature of the YAFTA algorithm, where the intersection of fragments from one frame with another is recognised was added, then we could classify events as merging, splitting or emergence. In that case, we would be able to identify which of the changes in the bulk properties correspond to flux emergence.

A lifetime criterion, even a moderate one of eg. a fragment existing for at least two frames, could also be implemented. No findings in this research suggested against it and its inclusion would limit the background noise both in the temporal and spatial plots. On the contrary, a spatial criterion should not be part of the pipeline, unless the least B_{LOS} threshold are reduced and more field is allowed to be identified by our code. This is because the flares studied tended to happen around small fragments.

A next step to take in this research, would be to identify what is meant by a change in the properties. A good place to start is to continue the work by Sudol & Harvey (2005); Petrie & Sudol (2010); Burtseva & Petrie (2013); Burtseva et al. (2015); Castellanos Durán et al. (2018); Petrie (2019), to identify when a ΔB_{LOS} takes place and to what extend and then, for those times, see if there are any changes in the other properties we have calculated. We could also make further

use of the RHESSI database to compare the flare and fragment centroid location. Burtseva et al. (2015) found that fragments align strongly with early emission detected by RHESSI but weak changes were not as well associated. It would be exciting to see the results that would come up for microflares.

Chapter 7

Conclusions and future work

The motivation of this thesis was to identify characteristic properties of the solar magnetic field that are associated with flares. We made use of observational data and created methods to allow for their statistical analysis in order to identify any possible patterns of behaviour. This work has been separated into two different sections; Chapter 3 focussed on the association of one pattern of the large-scale magnetic field with flares, while Chapter 4 goes in the opposite direction, looking at field changes on much smaller scales.

In Chapter 3 we used two independent methods, one utilising ground based data and one using magnetic field extrapolations, to identify and track parts of the boundaries between sectors of opposite polarities of the Interplanetary Magnetic Field, the Hale Sector Boundaries (HSBs). At the same time, the flare catalogue of the RHESSI instrument provided an opportunity to perform a much larger statistical study than those already in the literature, searching for a connection between HSBs and flares. We showed that 41% of RHESSI flares in Cycle 23 and 47% for Cycle 24 happened no further than 30^o from HSB. The HSBs exhibited the expected behaviour when detected by either method, following the Solar Cycle as dictated by Hale's law. Their flare association ranged from fairly sharp, as was for Cycle 23, to more ambiguous for Cycle 24.

This suggests a connection between flux emergence and release of free magnetic energy with the deep interior. Sunspots also follow the Hale boundary (Svalgaard & Wilcox 1976) but flares sharpen this relationship. The behaviour of flare occurrence was also previously presented for Cycle 23 (Svalgaard et al. 2011), which

we confirmed comprehensively. It is unclear whether using another magnetic field extrapolation would have sharpened our results. Even at distances of $2R_{\odot}$, we are looking at places where the magnetic field dominates, but it cannot be excluded that a twist of the field might be having an impact in the organisation of the HSBs. In any case, it would be interesting as future work to see a reproduction of this methodology with different field extrapolations and compare the resulting statistics. Another question to answer is what is the link between the solar dynamo and HSBs. The large-scale structures have been difficult to study because of the long timescales they cover, and therefore this question remains to-date.

In Chapter 4 we examined the migration paths both of HSBs and of regions of the Sun with persistent and periodic appearance of sunspots, Active Longitudes. We found HSBs to be fairly well organised and assuming a two-sector pattern during the declining phase of solar cycle 23, while they had a more chaotic profile, with a four sector structure during the rising phases of cycle 23 and 24. Active Longitudes had a similar behaviour as HSBs, with their movement being faster and then slower than the Carrington rate at the start and at the end phase of the cycles. However, their migration paths did not always match those of the HSBs while at other times they seemed very similar. The fact that they are both associated in some level with flares (Svalgaard et al. 2011; Loumou, K. et al. 2018; Gyenge et al. 2016) implied that there should be an agreement between them. It does not imply however that they are necessarily the same phenomenon. In fact Usoskin et al. (2005); Gyenge et al. (2016) showed that Active Longitudes have a distinct parabolic path for much longer timescales than we could see with HSBs. An extension of this work, would be to take advantage of the HSB-PFSS approach for all magnetograms suitable and repeat this work on larger timescales.

In Chapter 5 we presented the Python pipeline we created, starting from the in-house algorithm of Watson (2012) and extending it to perform fragmentation and feature tracking with time. In order to do so, we used a downhill and watershed approach, which we explained in detail. We applied our pipeline on three microflaring regions in Chapter 6. We looked at the bulk properties of the regions in time and searched for preferred directions of drift of the fragments. The results were not conclusive in this case, with both increases and decreases in the area and flux of the fragments both before and after flares. More consistency seemed to be

present in the fact that the positive field exhibited more changes than the negative field for all three regions and that A-class flares were more often associated with a decrease in flux than an increase. It is not clear whether this is due to a physical reason as in two out of three cases the positive field interacted with the negative field. The implosion scenario of Hudson et al. (2008), confirmed by Burtseva & Petrie (2013) for large flares, states that the LoS flux post-flare will decrease as the field shears further and turns mainly horizontal.

There are a number of limitations that should be considered when conducting research of this kind. The scope for improvement in our pipeline is one of them. The main property missing from our code is the ability to detect merging and splitting of fragments. It would be advantageous to follow the procedure of YAFTA and query the intersection of the surfaces of fragments from one frame to the next to identify which fragments split, which merged and which emerged or cancelled out. This would give us the opportunity to sort out any changes happening in the fragments accordingly. In this way, we would be able to tell if a change in the field properties happened because fragments appeared or merged etc.

Lamb et al. (2013) flag that feature lifetimes do not necessarily correspond to emergence or cancellation. Finding an increase of a region property via its timeseries could be just the result of the field being re-arranged or of previously unresolved flux becoming detectable by the instrument. Equally, a decrease in properties or in number of features could simply be due to dispersion. Another way to test this is to study the drift of fragments seeming to disperse or cancel out, to see if the migration path reappears in later stages. That would be an indication that the fragments just dispersed and did not cancel out.

Another issue is the data we used. We were restricted to LoS as we were interested in using the downhill approach. However, Leka & Barnes (2003) note the need to use both LoS and vector magnetograms as they argue that the phenomena taking place in the photosphere could be not well connected with the conditions in the chromosphere.

Is the location of the flares important? Burtseva & Petrie (2013) studied the total change in flux per fragment, moving from Sun-centre to Sun-limb. They found no correlation between those two parameters. This is something that we

could incorporate in order to test for microflares. In a similar aspect, another step in our research could be to plot the latitudinal and longitudinal speed of the longest lived fragments with time, trying to identify a preferred drift in a more quantified manner than the spatial profiles of Chapter 6.

Another issue was that due to the number of flares, we only looked at their start times. Sudol & Harvey (2005) found no changes before a flare, but detected stepwise changes of large flares before the flares ended. It would be interesting to add the peak and end times of our flarelist and see where the changes we show occur in the property timelines.

Finally a case could be that there is nothing to be found. Leka & Barnes (2003) they found no consistent signature before flares, something that changed with the findings of Schrijver (2007) and the association between the unsigned flux close to the Polarity Inversion Line and strong flares. In Leka & Barnes (2007) it is shown that the total excess energy of the photospheric magnetic field is the most important parameter from the ones frequently used in Solar Flare forecasting. Castellanos Durán et al. (2018) find that the smallest flares exhibiting a stepwise change is a C3.0 GOES class flare but lacking large enough numbers of microflares in their sample.

The statistical research of small flares is still an open field, with the latest article to-date on the topic being Petrie (2019), where they start from a C9.0-class flare upwards.

Bibliography

Altschuler, M. D. & Newkirk, G. 1969, Sol. Phys., 9, 131

Anusha, L. S., Solanki, S. K., Hirzberger, J., & Feller, A. 2017, A&A, 598, A47

Aschwanden, M. J. 2010, Sol. Phys., 262, 235

Attie, R. & Innes, D. E. 2015, A&A, 574, A106

Bai, T. 2003, ApJ, 585, 1114

Baranyi, T., Győri, L., & Ludmány, A. 2016, Sol. Phys., 291, 3081

Berdyugina, S. V., Moss, D., Sokoloff, D., & Usoskin, I. G. 2006, A&A, 445, 703

Berdyugina, S. V. & Usoskin, I. G. 2003, A&A, 405, 1121

Beucher, S. & Lantuéjoul, C. 1979, Use of Watersheds in Contour Detection, workshop published

Bigazzi, A. & Ruzmaikin, A. 2004, ApJ, 604, 944

Bumba, V. & Obridko, V. N. 1969, Sol. Phys., 6, 104

Burtseva, O., Martínez-Oliveros, J. C., Petrie, G. J. D., & Pevtsov, A. A. 2015, ApJ, 806, 173

Burtseva, O. & Petrie, G. 2013, Sol. Phys., 283, 429

Canfield, R. C. & Russell, A. J. B. 2007, The Astrophysical Journal, 662, L39

Carmichael, H. 1964, NASA Special Publication, 50, 451

Carrington, R. C. 1863, Observations of the Spots on the Sun from November 9, 1853 to March 24, 1861, Made at Redhill (Williams and Norgate)

Carroll, B. W. & Ostlie, D. A. 2006, An introduction to modern astrophysics and cosmology

Castellanos Durán, J. S., Kleint, L., & Calvo-Mozo, B. 2018, ApJ, 852, 25

Christe, S., Hannah, I. G., Krucker, S., McTiernan, J., & Lin, R. P. 2008, ApJ, 677, 1385

Community, T. S., Mumford, S. J., Christe, S., et al. 2015, Computational Science & Discovery, 8, 014009

Couvidat, S., Schou, J., Hoeksema, J. T., et al. 2016, Solar Physics, 291, 1887

Crawford, D. F., Jauncey, D. L., & Murdoch, H. S. 1970, ApJ, 162, 405

DeForest, C. E., Hagenaar, H. J., Lamb, D. A., Parnell, C. E., & Welsch, B. T. 2007, The Astrophysical Journal, 666, 576

Dittmer, P. H. 1975, Sol. Phys., 41, 227

Echer, E. & Svalgaard, L. 2004, Geophys. Res. Lett., 31, L12808

Falconer, D. A., Moore, R. L., Barghouty, A. F., & Khazanov, I. 2012, The Astrophysical Journal, 757, 32

Fletcher, L., Dennis, B. R., Hudson, H. S., et al. 2011, Space Sci. Rev., 159, 19

Gaizauskas, V., Harvey, K. L., Harvey, J. W., & Zwaan, C. 1983, ApJ, 265, 1056

Getachew, T., Virtanen, I., & Mursula, K. 2017, Sol. Phys., 292, 174

Gyenge, N., Baranyi, T., & Ludmány, A. 2012, Central European Astrophysical Bulletin, 36, 9

Gyenge, N., Baranyi, T., & Ludmány, A. 2014, Sol. Phys., 289, 579

Gyenge, N., Ludmány, A., & Baranyi, T. 2016, ApJ, 818, 127

Gyenge, N., Singh, T., Kiss, T. S., Srivastava, A. K., & Erdélyi, R. 2017, ApJ, 838, 18

Győri, L., Ludmány, A., & Baranyi, T. 2017, MNRAS, 465, 1259

Hagenaar, H. J., Schrijver, C. J., Title, A. M., & Shine, R. A. 1999, The Astrophysical Journal, 511, 932

Hale, G. E., Ellerman, F., Nicholson, S. B., & Joy, A. H. 1919, Astrophys. J., 49, 153

Hale, G. E., Ellerman, F., Nicholson, S. B., & Joy, A. H. 1919, ApJ, 49, 153

Hannah, I. G., Hudson, H. S., Battaglia, M., et al. 2011, Space Sci. Rev., 159, 263

Higgins, P., Gallagher, P., McAteer, R., & Bloomfield, D. 2011, Advances in Space Research, 47, 2105 , recent Advances in Space Weather Monitoring, Modelling, and Forecasting - 2

Hirayama, T. 1974, Sol. Phys., 34, 323

Howard, R. F., Harvey, J. W., & Forgach, S. 1990, Sol. Phys., 130, 295

Hudson, H. S. 1991, Sol. Phys., 133, 357

Hudson, H. S., Fisher, G. H., & Welsch, B. T. 2008, in Astronomical Society of the Pacific Conference Series, Vol. 383, Subsurface and Atmospheric Influences on Solar Activity, ed. R. Howe, R. W. Komm, K. S. Balasubramaniam, & G. J. D. Petrie, 221

Hudson, H. S., Svalgaard, L., & Hannah, I. G. 2014, Space Sci. Rev., 186, 17

Hurford, G. J. 2010, ISSI Scientific Reports Series, 9, 223

Hurford, G. J., Schmahl, E. J., Schwartz, R. A., et al. 2002, Sol. Phys., 210, 61

Ivanov, K. G. 2010, Geomagnetism and Aeronomy, 50, 285

Ivanov, K. G. & Kharshiladze, A. F. 2013, Geomagnetism and Aeronomy, 53, 677

Khan, A. M. & Ravi, S. 2013, International Journal of Soft Computing and Engineering (IJSCE), 3, 84

Kopp, R. A. & Pneuman, G. W. 1976, Sol. Phys., 50, 85

Lamb, D. & Deforest, C. E. 2003, in AGU Fall Meeting Abstracts, Vol. 2003, SH42B–0530

Lamb, D. A., DeForest, C. E., Hagenaar, H. J., Parnell, C. E., & Welsch, B. T. 2008, ApJ, 674, 520

Lamb, D. A., Howard, T. A., DeForest, C. E., Parnell, C. E., & Welsch, B. T. 2013, ApJ, 774, 127

Leka, K. D. & Barnes, G. 2003, ApJ, 595, 1277

Leka, K. D. & Barnes, G. 2007, ApJ, 656, 1173

Li, J. 2011, ApJ, 735, 130

Lin, R. P., Dennis, B. R., Hurford, G. J., et al. 2002, Sol. Phys., 210, 3

Lockwood, M. 2013, Living Reviews in Solar Physics, 10

Losh, H. M. 1939, Publications of Michigan Observatory, 7, 127

Loumou, K., Hannah, I. G., & Hudson, H. S. 2018, A&A, 618, A9

Mann, G., Warmuth, A., & Aurass, H. 2009, A&A, 494, 669

Mansurov, S. M. 1969, Geomagnetism and Aeronomy, 9, 622

Mavromichalaki, H., Plainaki, C., Zouganelis, I., & Petropoulos, B. 2003, Sol. Phys., 218, 63

McIntosh, P. S. 1990, Sol. Phys., 125, 251

Ness, N. F., Scearce, C. S., & Seek, J. B. 1964, J. Geophys. Res., 69, 3531

Parker, E. N. 1958, ApJ, 128, 664

Parnell, C. E. 2002, MNRAS, 335, 389

Parnell, C. E., DeForest, C. E., Hagenaar, H. J., et al. 2009, ApJ, 698, 75

Pelt, J., Korpi, M. J., & Tuominen, I. 2010, A&A, 513, A48

Petrie, G. J. D. 2019, The Astrophysical Journal Supplement Series, 240, 11

Petrie, G. J. D. & Sudol, J. J. 2010, The Astrophysical Journal, 724, 1218

Potts, H. E. & Diver, D. A. 2008, Sol. Phys., 248, 263

Rosenberg, R. L. & Coleman, Jr., P. J. 1969, J. Geophys. Res., 74, 5611

Schatten, K. H., Wilcox, J. M., & Ness, N. F. 1969, Sol. Phys., 6, 442

Schrijver, C. J. 2007, ApJ, 655, L117

Schwartz, R. A., Csillaghy, A., Tolbert, A. K., et al. 2002, Sol. Phys., 210, 165

Shibata, K. & Magara, T. 2011, Living Reviews in Solar Physics, 8

Soille, P. J. & Ansoult, M. M. 1990, Signal Processing, 20, 171

Spirock, T. J., Yurchyshyn, V. B., & Wang, H. 2002, The Astrophysical Journal, 572, 1072

Strous, L. H., Scharmer, G., Tarbell, T. D., Title, A. M., & Zwaan, C. 1996, A&A, 306, 947

Sturrock, P. A. 1966, Nature, 211, 695

Sudol, J. J. & Harvey, J. W. 2005, ApJ, 635, 647

Sun, X., Hoeksema, J. T., Liu, Y., Kazachenko, M., & Chen, R. 2017, ApJ, 839, 67

Svalgaard, L. 1968, Geofysiske Meddelelser, R-6

Svalgaard, L. 1972, J. Geophys. Res., 77, 4027

Svalgaard, L., Hannah, I. G., & Hudson, H. S. 2011, ApJ, 733, 49

Svalgaard, L. & Wilcox, J. M. 1976, Sol. Phys., 49, 177

Svalgaard, L., Wilcox, J. M., Scherrer, P. H., & Howard, R. 1975, Sol. Phys., 45, 83

Toriumi, S. & Wang, H. 2019, Living Reviews in Solar Physics, 16, 3

Usoskin, I. G., Berdyugina, S. V., Moss, D., & Sokoloff, D. D. 2007, Advances in Space Research, 40, 951

Usoskin, I. G., Berdyugina, S. V., & Poutanen, J. 2005, A&A, 441, 347

van der Walt, S., Schönberger, J. L., Nunez-Iglesias, J., et al. 2014, PeerJ, 2, e453

Verbeeck, C., Delouille, V., Mampaey, B., & De Visscher, R. 2014, A&A, 561, A29

Wang, H. 1992, Solar Physics, 140, 85

Wang, H., Ewell, Jr., M. W., Zirin, H., & Ai, G. 1994, ApJ, 424, 436

Wang, H. & Liu, C. 2015, Research in Astronomy and Astrophysics, 15, 145

Wang, H., Spirock, T. J., Qiu, J., et al. 2002, The Astrophysical Journal, 576, 497

Watson, F., Fletcher, L., Dalla, S., & Marshall, S. 2009, Solar Physics, 260, 5

Watson, F. T. 2012, PhD thesis, University of Glasgow

Welsch, B. T., Christe, S., & McTiernan, J. M. 2011, Sol. Phys., 274, 131

Welsch, B. T. & Longcope, D. W. 2003, The Astrophysical Journal, 588, 620

Wheatland, M. S. 2004, ApJ, 609, 1134

Wilcox, J. M. & Ness, N. F. 1965, J. Geophys. Res., 70, 5793

Zhang, L., Mursula, K., Usoskin, I., & Wang, H. 2011, Journal of Atmospheric and Solar-Terrestrial Physics, 73, 258

Zwaan, C. 1987, ARA&A, 25, 83